A New Lagrangian Perspective on Atmospheric Heat Extremes

Dissertation

zur Erlangung des Grades

„Doktor der Naturwissenschaften“

am Fachbereich Physik, Mathematik und Informatik

der

Johannes Gutenberg-Universität

in Mainz

Amelie Maria Mayer

Date of oral examination: 4 December 2025
Supervisor: Prof. Dr. Volkmar Wirth

Abstract

Heat extremes are among the most dangerous weather-related hazards. However, a full understanding of how heat extremes form in the Earth's atmosphere is still lacking. In particular, the relative importance of the three key processes—horizontal advection, subsidence, and diabatic heating—is a subject of ongoing debate. This thesis provides a new quantitative assessment on the relative importance of these processes employing the Lagrangian framework. A key aspect of this new assessment is the consideration of a Lagrangian climatology of the processes. The assessment reveals that horizontal advection can be seen as the main contributor to heat extremes across most of the globe.

In the first part of the thesis, a new method for extracting Lagrangian information about the atmospheric flow is developed, which is later used to quantify the key processes of heat extreme formation. The method is based on the advection of passive tracer fields in combination with a relaxation term. As a result, the method provides accumulated Lagrangian information, such as the recent diabatic heating experienced by air parcels along their pathways, at each point on an Eulerian grid at any time step. The method can be regarded as an alternative tool to calculating trajectories, tailored to gaining accumulated Lagrangian information efficiently.

In the second part of the thesis, the tracer method is then used to quantitatively assess the roles of the processes involved in heat extreme formation from a Lagrangian perspective. At each grid point and time step, the method provides a decomposition of temperature anomalies into the aforementioned processes. Two different decomposition approaches are contrasted: one that has been established in previous studies and which is based on the absolute contributions of the respective terms; and one that is introduced in this thesis and that considers the contributions in terms of anomalies, defined as deviations from their corresponding climatological means. The new decomposition is based on the understanding that a particularly large contribution from a given term may be irrelevant if it typically occurs as part of the climatology. By removing the atmosphere's climatological behaviour—which is of limited use in explaining anomalies—the new approach arguably provides a more meaningful framework for understanding anomalous temperatures. The analysis of two recent heatwaves in the extratropics reveals that the new decomposition offers a markedly different perspective on the relative importance of the processes compared to previous assessments of these cases. In particular, anomalous horizontal advection—specifically the absence of cold-air advection—rather than anomalous subsidence or diabatic heating, is found to be the key contributor to heat extremes in the studied regions.

In the final part of the thesis, the region-specific findings are extended to encompass the entire global domain. Most importantly, the analysis reveals that the contribution from

anomalous horizontal advection dominates the formation of near-surface heat extremes across the entire midlatitude region.

The presented Lagrangian diagnostic, together with the newly developed tracer method, could be readily applied to climate model simulations, providing a powerful tool to deepen our understanding of the processes driving heat extremes in a future climate, where they are likely to pose an even greater threat to society than today.

Contents

Chapter 1
1 Introduction

Mainz, a summer day in the near future: The asphalt sizzles, nature struggles, and people wipe the sweat from their foreheads. Hospitals are at capacity, water resources are scarce, and air conditioners run at full blast. Most people seem paralysed by the heat. And some may be wondering: Why is it so unbearably hot again?

Such a scenario might happen the next time Europe is hit by a heatwave. And it is likely that Europe will experience another heatwave sooner or later, as climate change is projected to increase the frequency and intensity of heat extremes worldwide (e.g. IPCC, 2021). But how do heat events form or to what extent do different processes contribute? This thesis aims to give more insights into this question.

Heat extremes across the globe share a common feature: a large-scale upper-level anticyclonic flow anomaly (e.g. Stefanon et al., 2012; Zschenderlein et al., 2019) that typically extends down to the surface. In the extratropics, these anomalies are generally linked to large-amplitude undulations of the jet stream in the form of extended ridges (e.g. Sousa et al., 2018) or atmospheric blocking (e.g. Pfahl and Wernli, 2012). Two typical examples of the mid-level flow conditions during severe heat extremes in the mid-latitudes are depicted in Figure 1.1. It includes the record-breaking heatwaves of 2021 in the Pacific Northwest and 2022 in Western Europe, during which a pronounced anticyclonic flow was evident above the high-temperature regions. Both heatwaves will be discussed later on in this thesis.

The anticyclonic flow anomaly is a crucial synoptic factor in the formation of heat extremes, but regional factors can also impact their severity and evolution. In this context, the interaction between the land and the atmosphere has often been considered important in amplifying heat extremes (e.g. Miralles et al., 2019, and references therein). In particular, soil moisture feedbacks that influence how the surface energy is divided into sensible and latent heat fluxes seem to play a role. That is, as soils dry out, less energy is used for evaporation and more is transferred through sensible heating, creating a positive feedback loop between atmospheric heating and drying. The local coupling between dry soils and the atmosphere has been recognised as crucial, for instance, in the European heatwave of 2003 (e.g. Fischer et al., 2007) and the Russian heatwave of 2010 (e.g. Miralles et al., 2014). Beyond local coupling, remote coupling through drought conditions upwind of the

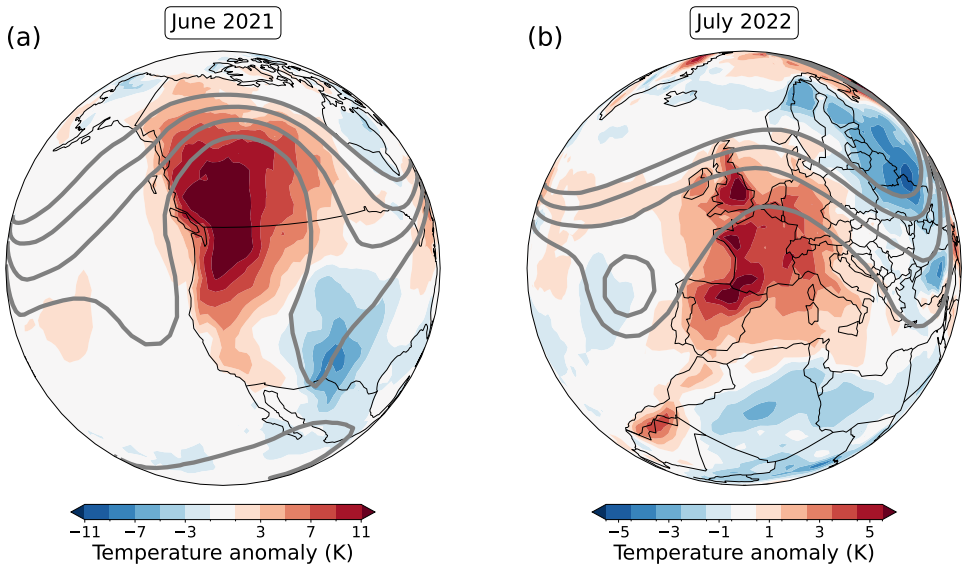

Figure 1.1 – 500 hPa geopotential height (grey contours; contour lines depict 56000 m, 56500 m, 57000 m, and 57500 m) and surface temperature anomaly (colour shading) during two heat extremes. (a) Temporal average between 27 June to 1 July 2021. (b) Temporal average between 16 to 20 June 2022. Data basis: ERA5 (Hersbach et al., 2023a; Hersbach et al., 2023b).

heatwave regions has also been considered important for these heat extremes (Schumacher et al., 2019).

Despite the profound knowledge of the large-scale atmospheric circulation and the documented soil-moisture feedbacks associated with heat extremes, a clear understanding of how air masses with anomalously high temperatures primarily form during heat extremes is, however, still lacking. Three processes are believed to play a central role in this context—horizontal warm air advection, subsidence accompanied by adiabatic warming, and diabatic heating—and the large-scale circulation appears to support all of them. The circulation facilitates the poleward *advection of warm air* along the western flank of the anticyclonic anomaly, while it also features widespread *subsidence*. This subsidence, on the one hand, is associated with compression and, thus, adiabatic warming of air masses and, on the other hand, suppresses cloud formation, resulting in mostly clear skies and increased shortwave radiation, which may, in turn, enable strong *diabatic heating* of air masses through surface sensible heat fluxes.

Importantly, though, the relative importance of each of the three processes in the formation of heat extremes is still subject to debate. Many studies have focused either on a single process (e.g. Fischer et al., 2007; Garfinkel and Harnik, 2017), specific cases (e.g. Black et al., 2004; Miralles et al., 2014; Zschenderlein et al., 2018), or selected regions (e.g. Quinting and Reeder, 2017; Sousa et al., 2019; Hochman et al., 2021), resulting in different conclusions about the relative importance of the three processes. These differences may

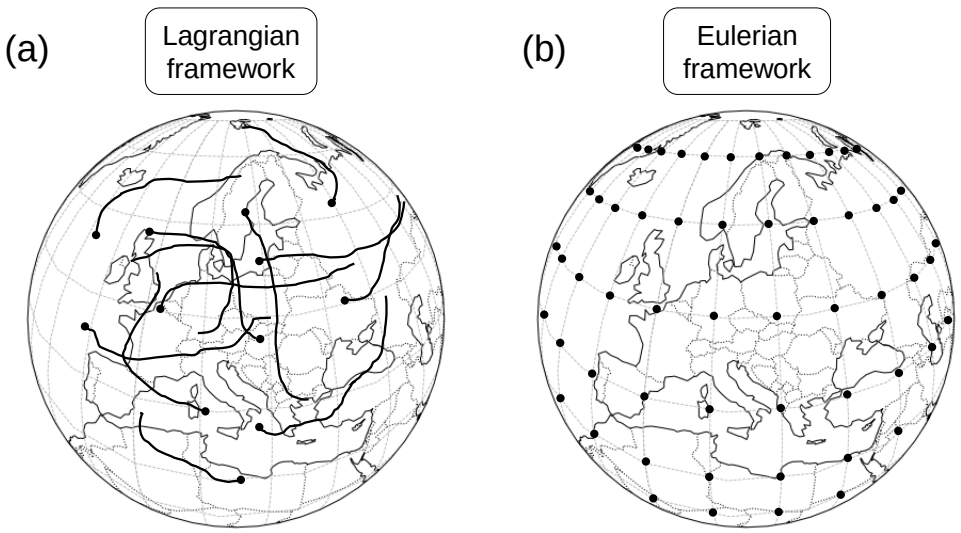

Figure 1.2 – Schematic illustrating the Lagrangian and the Eulerian frameworks. In the Lagrangian framework (panel a), the control volumes move with the flow. Trajectories (indicated by the black lines) describe their pathways. In contrast, in the Eulerian framework (panel b) the control volumes remain fixed in space. The evolution of the flow is described by temporal changes of the physical quantities at these fixed locations.

partly arise from the fact that the relative importance of the processes may vary from case to case and across different phases of the heat extreme development. However, they may also stem from the use of different—and at times inconsistent—formulations of the individual processes, complicating the comparison of results across studies and hindering the development of a coherent understanding of the processes' roles in the formation of heat extremes. Taken together, further research is required to clarify the question of which specific role the individual processes play in heat extreme formation, particularly on a global scale. The present thesis seeks to address this research gap.

In the thesis, the Lagrangian framework, named after *Joseph-Louis Lagrange* (1736–1813), will be employed, which offers a distinct approach for representing atmospheric fluid flows. In the Lagrangian framework (see Figure 1.2a), the evolution of the flow is described by tracking individual fluid parcels that move with the flow through space and time. This way of describing the flow provides a direct analogy to point mechanics and is the most intuitive way to generalise from a set of mass points to a continuum. Therefore, the Lagrangian framework is particularly useful, for example, in deriving the equations of motion of fluid dynamics, or in understanding atmospheric phenomena such as temperature extremes. In this context, the Lagrangian framework allows for determining where air masses originate from and how they are transformed over time—factors that play a critical role in shaping the final temperature of the air mass at a given location. However, from a practical point of view, the Eulerian framework (see Figure 1.2b), named after *Leonhard*

Euler (1707–1783), is often more convenient, as solving the equations of motion, for example, is quite complex within the Lagrangian framework. In the Eulerian framework, the evolution of the flow is described at fixed points in space as time passes. Most atmospheric models, for example numerical weather prediction models or climate models, work within this framework. Unfortunately, as a result, these models do not provide Lagrangian information at hand, which is key to gaining a comprehensive understanding of the physical processes that drive certain atmospheric phenomena. With some additional effort, however, Lagrangian information can be extracted from these models.

The most common approach to extracting Lagrangian information from Eulerian fields is the calculation of trajectories; either in forward or in backward mode. These trajectories track the pathways of individual parcels through space and time, providing time-resolved data on their geographical locations. Typically, additional variables such as temperature or pressure are then mapped onto the trajectories, offering a vast amount of information. However, this information is limited to those parcels that are explicitly tracked. For a proper analysis, either a large number of trajectories must be computed to ensure comprehensive coverage—probably resulting in a large amount of data—or a suitable preselection of air parcels must be made; a limitation that, in our view, has substantially constrained the ability of previous Lagrangian studies to draw meaningful conclusions.

One example that illustrates this limitation is the study by Zschenderlein et al. (2019), where only those near-surface air masses were tracked that contributed to a European heatwave which had already persisted for at least two days. This means that both the air masses responsible for the onset of heatwaves and all other air masses not associated with heatwaves were excluded from the analysis right from the beginning. Zschenderlein et al. (2019) found that air masses during heatwaves experience subsidence, associated with adiabatic warming, and concluded that adiabatic warming plays a crucial role in European heat extremes. Many other trajectory-based studies (e.g. Bieli et al., 2015; Quinting and Reeder, 2017; Villiers, 2020; Hochman et al., 2021), including the comprehensive study by Röthlisberger and Papritz (2023b), have reported similar findings and drawn comparable conclusions. Collectively, these studies infer—based on the finding that air masses undergo subsidence and associated adiabatic warming during heat extremes—that this process contributes substantially to the formation of such events. However—and this is a crucial point—none of these studies have compared the air masses during heat extremes with those not associated with heat extremes; a limitation that can likely be attributed, at least in part, to the inherent need for preselection imposed by the trajectory method. In other words, all of these trajectory-based studies lack a comparison with typical climatological conditions. In light of the findings presented in this thesis, we are convinced that, had such a comparison been conducted, many of these studies would likely have found that the degree of subsidence and associated adiabatic warming during heat extremes was not

substantially greater than that found for typical near-surface air masses; since most such air masses are likely to have experienced some degree of subsidence.

This line of thought leads to the core of this work: In this thesis, we systematically compute, for the first time from a Lagrangian perspective, a climatological reference for the processes thought to contribute to heat extremes. By comparing their contributions during heat extremes to their climatological reference, we then provide a suitable new framework to address the fundamental question of which processes behave anomalously during periods of anomalous temperature conditions. In other words, we focus on the idea that, to understand the origin of a pronounced anomaly, the key is to determine which process contributes to it in an anomalous way—rather than identifying the processes that generally warm air masses.

While this idea remains largely unexplored in Lagrangian analyses, it is well established in Eulerian studies (e.g. Sousa et al., 2018; Tamarin-Brodsky et al., 2019; Garfinkel et al., 2024); likely because the grid-point-based structure of the Eulerian framework is by far more convenient for compiling climatologies than the parcel-based nature of the Lagrangian framework. To take advantage of the computational convenience related to the Eulerian framework, we developed in this thesis a novel method that serves as an alternative to the traditional trajectory approach. The method enables the straightforward computation of Lagrangian climatologies while operating entirely within the Eulerian framework. More broadly, the method provides a novel way to access Lagrangian information from grid-point-based data, bridging the gap between parcel-based diagnostics and Eulerian analysis. While the method involves some temporal aggregation and thus a reduction in Lagrangian detail, it makes up for this loss in information by offering continuous, three-dimensional coverage in space and time. This four-dimensional completeness is especially beneficial for compiling climatologies such as those of adiabatic or diabatic heating, but may also prove useful in a wide range of other Lagrangian applications. Although the method does not provide information that could not, in principle, also be derived from the trajectory method, we consider a key advantage to be that the resulting Lagrangian diagnostics are directly accessible on an Eulerian grid, facilitating their handling and integration into data analysis workflow, such as the computation of climatologies. Moreover, for certain applications, the method proves to be more computationally efficient.

The thesis is structured as follows. In Chapter 2, we will introduce the mathematical concept of the new method along with a numerical implementation, while we will also highlight potential application examples in a qualitative manner. In Chapters 3 and 4, we will then proceed to the core of this thesis: Using our new method, we will systematically quantify the roles of horizontal advection, subsidence, and diabatic heating in the formation of heat extremes by assessing, for the first time within the Lagrangian framework, their contributions in relation to what can be expected from climatology. For this purpose, we

will follow the Lagrangian temperature anomaly decomposition approach introduced by Röthlisberger and Papritz (2023b), which we will expand to include the climatological behaviour of air masses. In Chapter 3, we will examine two specific heat events from recent history, investigating both the temporal evolution and the vertical structure of the individual contributions of each process. In Chapter 4, we will extend the Lagrangian analysis to the entire globe focusing on the near-surface. In both chapters, we will begin with an assessment that disregards the climatological behaviour of the individual terms, only to show that evaluating the contributions as deviations from their climatological averages fundamentally alters the results. Chapter 5 will summarise our key findings, while Chapter 6 will offer an outlook. Taken together, this thesis will provide a fresh and compelling perspective on the relative importance of the processes driving heat extremes. According to our new assessment, horizontal advection—rather than subsidence or diabatic heating—ultimately emerges as the primary driver of heat extremes across most of the globe.

Author's note: Chapters 2 and 3 have been published as articles in peer-reviewed journals, while the article presented in Chapter 4 is currently under review. For integration into this document, sections, figures, and equations of these articles have been renumbered. Formal edits have been made to ensure consistency in spelling, punctuation, abbreviations, symbol notation, bibliography formatting, and other stylistic elements. These editorial changes have not affected the original content. Any modifications to the content itself are clearly indicated in italic footnotes. In the case of co-authored articles, the individual contributions of each author are specified at the end of the respective chapter.

Chapter 2

2 Lagrangian Description of the Atmospheric Flow from Eulerian Tracer Advection with Relaxation

This chapter has previously been published in:

Mayer, A. and V. Wirth (2023). "Lagrangian description of the atmospheric flow from Eulerian tracer advection with relaxation". *Quarterly Journal of the Royal Meteorological Society* 149.753, pp. 1271–1292. DOI: 10.1002/qj.4453

Abstract The Lagrangian representation of fluid flows offers a natural perspective to study many kinds of physical mechanisms. By contrast, the Eulerian representation is more convenient from a diagnostic point of view. This article attempts to combine elements of both worlds by proposing an Eulerian method that allows one to extract Lagrangian information about the atmospheric flow. The method is based on the offline advection of passive tracer fields and includes a relaxation term. The latter device allows one to run the integration in a continuous fashion without the need for reinitialisation. As a result one obtains accumulated Lagrangian information, for example, about the recent parcel displacement or the recent parcel-based diabatic heating, at each point of an Eulerian grid at any time step. The method is implemented with a pseudospectral algorithm suitable for gridded global atmospheric data and compared with the more traditional trajectory method. The method's utility is demonstrated on the basis of a few examples, which relate to cloud formation and the development of temperature anomalies. The examples highlight that the method provides a convenient diagnostic of parcel-based changes, paving an intuitive way to explore the physical processes involved. Due to its grid-point-based

nature, the proposed method can be applied to large data sets in a straightforward and computationally efficient manner, suggesting that the method is particularly useful for climatological analyses.

2.1 Introduction

One of the primary goals in meteorology is arguably to understand the underlying physical mechanisms that shape atmospheric phenomena on Earth. The laws of physics such as Newton's laws of motion or the laws of thermodynamics inherently apply to air parcels. A natural way to study meteorological phenomena is, therefore, the Lagrangian perspective, which follows individual fluid parcels and determines their physical properties and how they change with time. However, numerical atmospheric models usually take the Eulerian perspective, which means that they describe the flow in terms of fields on a fixed grid. The Eulerian perspective is very convenient from a diagnostic point of view, since variables are available at known grid points and thus can easily be processed further; moreover, it also conforms to many observing systems. The disadvantage of Eulerian models is that their output usually does not allow direct access to Lagrangian information.

A widely used method for teasing out Lagrangian information from grid-point-based fields is the calculation of trajectories (Reed, 1955; Danielsen, 1961). Trajectories allow one to study a variety of meteorological phenomena such as heat waves (e.g. Harpaz et al., 2014; Zschenderlein et al., 2019; Zschenderlein et al., 2020; Spensberger et al., 2020), extratropical cyclones and warm conveyor belts (e.g. Wernli, 1997; Eckhardt et al., 2004; Madonna et al., 2014), troposphere–stratosphere exchange (e.g. Wernli and Bourqui, 2002; Birner and Bönisch, 2011; Škerlak et al., 2014), moisture transport (e.g. Stohl et al., 2008; Knippertz and Wernli, 2010; Ryoo et al., 2015), and air pollution (for references see Fleming et al., 2012, their Table 1). A wealth of information can be obtained from trajectories, as they provide time-resolved knowledge about the physical properties along the pathways of individual parcels. For many applications this is useful or even necessary, but for certain applications this may be more than is needed. For instance, it is sometimes sufficient to restrict attention to time-accumulated Lagrangian information, and in such a situation it would be convenient to have a method that is tailored to provide accumulated Lagrangian information only.

In the current article, we propose such a method, which combines elements of both Lagrangian and Eulerian worlds. The method is based on the advection of passive tracers in combination with a relaxation term. A passive tracer can be any kind of substance or physical quantity that is advected by the flow without feeding back to the dynamics. This allows one to track air motion and to visualise the result of atmospheric transport

through the use of passive tracers. For instance, chemical species with distinct sources in the atmosphere such as carbon monoxide or ozone have been used as tracers, allowing one to measure (or model) their atmospheric concentration and hence retrieve important information about atmospheric transport pathways. While this method has often been applied in the context of the stratospheric circulation and troposphere–stratosphere exchange (e.g. Brewer, 1949; Dobson, 1956; Fischer et al., 2000; James, 2003; Bönisch et al., 2009; Hegglin et al., 2009; Hoor et al., 2002; Hoor et al., 2010; Ploeger and Birner, 2016; Ploeger et al., 2017), passive tracers have been used much less frequently to study tropospheric dynamics. This is what we aim to focus on in the present article.

Our method builds upon an approach initially proposed by Schär and Wernli (1993) in the framework of a semigeostrophic model and explored further by Gheusi and Stein (2002) with regard to mesoscale numeric modelling. Their approach is based on the advection of three Eulerian passive tracer fields initialised with the coordinates of each grid cell. Likewise, we draw on the ideas inherent in the potential vorticity tracer technique by Davis et al. (1993), which was later applied, for example, by Stoelinga (1996), Gray (2006), or Chagnon et al. (2013). Their technique is based on the advection of potential-vorticity-like tracer fields, each of which is subject to a modification by a certain diabatic process. Similarly to the aforementioned methods, our method uses fields of latitude, pressure, or potential temperature as passive tracers on an Eulerian grid. The novelty of our method is that it incorporates a relaxation term, which turns out to be beneficial for practical reasons.

It is the goal of this article to present the underlying idea of our method and motivate its utility for various types of Lagrangian analysis on the synoptic scale. The article is organised as follows. In Section 2.2, we outline the basic idea of the method. Section 2.3 presents an algorithm for the implementation to gridded model data on the synoptic scale. In Section 2.4, we compare the results of our algorithm with the results from trajectory calculations, before we provide a few short, illustrative examples in Section 2.5 regarding the method's utility. Finally, a summary is given in Section 2.6.

2.2 The method

2.2.1 Basic idea

We start by presenting the basic idea with the help of an example. Consider the vertical displacement Δ_Z of an air parcel, which is defined as

$$\Delta_Z(t) := Z(t) - Z(t_0) \,, \tag{2.1}$$

where $Z(t)$ denotes the parcel's altitude at time t and t_0 denotes the initial time. The definition implies that the vertical displacement is zero at the initial time, that is,

$$\Delta_Z(t_0) = 0 \ . \tag{2.2}$$

Taking the time derivative of Equation (2.1), one obtains

$$\frac{d\Delta_Z(t)}{dt} = W(t) \ , \tag{2.3}$$

where

$$W(t) = \frac{dZ(t)}{dt} \tag{2.4}$$

represents the vertical motion of the parcel, that is, the vertical wind at the location of the parcel. Note also that we use the notation d/dt for the time derivative of a variable that depends on time only. If we consider Equation (2.3) as a differential equation for $\Delta_Z(t)$, this can be integrated to yield

$$\Delta_Z(t) = \int_{t_0}^{t} W(t') \, dt' \ , \tag{2.5}$$

where Equation (2.2) was used to determine the constant of integration. Note that Equation (2.5) is not an integral of the vertical wind at a certain location; instead, as denoted by Equation (2.4), it is an integral of the vertical wind at the position of the parcel, that is, an integral along the trajectory of the parcel.

Equation (2.5) yields the vertical displacement of the air parcel within the time interval of length $t - t_0$. The length of this time interval is growing with time t, since t_0 is the (fixed) initial time. However, for some applications it would be desirable to limit this time interval to a finite length like a window that moves with the considered time t. This motives us to add a relaxation term on the right-hand side of Equation (2.3), yielding the following modified initial-value problem for the evolution of $\Delta_Z(t)$, namely

$$\frac{d\Delta_Z(t)}{dt} = W(t) - \lambda \Delta_Z(t) \ , \quad \Delta_Z(t_0) = 0 \ . \tag{2.6}$$

The relaxation term in itself effectively models an exponential decay of $\Delta_Z(t)$ with the rate $\lambda > 0$. As we will see shortly, this decay results in a finite memory of the parcel for its vertical displacement.

From a mathematical point of view, Equation (2.6) is an inhomogeneous ordinary differential equation with $W(t)$ representing the inhomogeneous term, that is, the forcing.

The equation can be solved using mathematical standard methods such as separation of variables and variation of the constant. The solution of Equation (2.6) reads

$$\Delta_Z(t) = \int_{t_0}^{t} W(t')\, e^{-\lambda(t-t')}\, dt' \;, \tag{2.7}$$

which can be readily verified by direct substitution into Equation (2.6). Obviously, for $\lambda = 0$ this solution recovers Equation (2.5), which means that the solution takes into account the vertical wind $W(t')$ throughout the integration with equal weight for any time t'. By contrast, for $\lambda > 0$, the contribution of $W(t')$ at earlier times is exponentially damped away, such that the solution makes substantial use of information from $W(t')$ only during the recent past $t' > t - \lambda^{-1}$. In other words, a positive value of λ represents a finite memory of the parcel for accumulating the vertical wind in the expression for the vertical displacement.

The equation for $\Delta_Z(t)$ can be reformulated in an alternative manner, which turns out to be useful in practice (see below). With the help of Equation (2.4), Equation (2.6) becomes

$$\frac{d\Delta_Z(t)}{dt} = \frac{dZ(t)}{dt} - \lambda\Delta_Z(t) \;, \quad \Delta_Z(t_0) = 0 \;. \tag{2.8}$$

Defining

$$\Psi(t) := Z(t) - \Delta_Z(t) \;, \tag{2.9}$$

which satisfies the initial condition $\Psi(t_0) = Z(t_0)$, and taking the time derivative, we obtain the following initial-value problem:

$$\frac{d\Psi(t)}{dt} = -\lambda[\Psi(t) - Z(t)] \;, \quad \Psi(t_0) = Z(t_0) \;. \tag{2.10}$$

The solution $\Psi(t)$ can be used to retrieve the vertical displacement through Equation (2.9), that is,

$$\Delta_Z(t) = Z(t) - \Psi(t) \;. \tag{2.11}$$

2.2.2 Generalisation

Now consider a more general pair of parcel variables $(A, \dot{A})$ satisfying

$$\dot{A}(t) = \frac{dA(t)}{dt} \;. \tag{2.12}$$

In the special case of the previous example, these generalised variables can be identified as $(A, \dot{A}) = (Z, W)$ owing to Equation (2.4). A generalised displacement $\Delta_A(t)$ is then, by analogy with Equation (2.6), defined through

$$\frac{d\Delta_A(t)}{dt} = \dot{A}(t) - \lambda\Delta_A(t) \;, \quad \Delta_A(t_0) = 0 \;, \tag{2.13}$$

and (2.10) and (2.11) turn into

$$\frac{d\Psi(t)}{dt} = -\lambda[\Psi(t) - A(t)] \;, \quad \Psi(t_0) = A(t_0) \;, \tag{2.14}$$

from which the desired quantity $\Delta_A(t)$ can be obtained through

$$\Delta_A(t) = A(t) - \Psi(t) \;. \tag{2.15}$$

Pairs of variables satisfying Equation (2.12) can be, for example,

$$(X, U), \;\; (Y, V), \;\; (P, \Omega), \;\; (\Theta, Q) \;, \tag{2.16}$$

where X denotes the position of the parcel in the zonal direction, Y is the position of the parcel in the meridional direction, P is the pressure of the parcel, Θ its potential temperature, U is the zonal wind, V is the meridional wind, Ω is the vertical wind in pressure coordinates, and $Q = d\Theta/dt$ is the diabatic heating, defined as the material rate of change of potential temperature, all of these taken at the position of the parcel at time t. The corresponding "generalised displacements" are denoted as Δ_X, Δ_Y, Δ_P, and Δ_Θ, and they represent the parcel's displacement in the zonal direction, the parcel's displacement in the meridional direction, the parcel's vertical displacement in terms of pressure, and the accumulated diabatic heating (as defined through potential temperature), respectively.

The special case of the (Θ, Q) pair explains why the formulation in Equation (2.14) may sometimes be more straightforward to apply than the formulation in Equation (2.13): the former requires only knowledge about the parcel's potential temperature (which usually is readily available), while the latter requires explicit knowledge about the diabatic heating (which is typically much harder to obtain from, or even unavailable in, standard data sets).

2.2.3 Formulation as an Eulerian method

So far we have only considered the evolution of the property of a specific parcel, which corresponds to the Lagrangian perspective. This resulted in a simple inhomogeneous linear ordinary differential equation. We now shift to the Eulerian perspective and consider the parcel displacement as a function of space and time, that is, $\delta_a(\boldsymbol{x}, t)$, where $\boldsymbol{x} = (x, y, z)$

denotes the parcel's location in three-dimensional space and t is time (as before). This change in perspective can be achieved through replacing the time derivative along the air parcel, d/dt, by the total (or material) derivative D/Dt operating on the respective Eulerian field. The material derivative can be related to partial derivatives in time and space through the following well-known relation:

$$\frac{D}{Dt} = \frac{\partial}{\partial t} + \boldsymbol{u}(\boldsymbol{x}, t) \cdot \nabla \; . \tag{2.17}$$

Here, $\boldsymbol{u}(\boldsymbol{x}, t) = (u, v, w)$ denotes the three-dimensional Eulerian wind field, $\partial/\partial t$ is the partial time derivative, and $\nabla = (\partial/\partial x, \partial, \partial y, \partial/\partial z)$ is the Nabla operator. Effectively, Equation (2.17) turns Equation (2.13) into an equation for the evolution of $\delta_a(\boldsymbol{x}, t)$, namely

$$\frac{\partial \delta_a(\boldsymbol{x}, t)}{\partial t} = -\boldsymbol{u}(\boldsymbol{x}, t) \cdot \nabla \delta_a(\boldsymbol{x}, t) - \lambda \, \delta_a(\boldsymbol{x}, t) + \dot{a}(\boldsymbol{x}, t) \; , \quad \delta_a(\boldsymbol{x}, t_0) = 0 \; . \tag{2.18}$$

Note that we switched consistently from upper-case to lower-case notation in order to clarify that we are now dealing with Eulerian fields, for example, $\psi(\boldsymbol{x}, t)$ instead of $\Psi(t)$ and $\delta_a(\boldsymbol{x}, t)$ instead of $\Delta_A(t)$. In analogy with Equation (2.14), the problem in Equation (2.18) is equivalent to solving a problem for $\psi(\boldsymbol{x}, t)$:

$$\frac{\partial \psi(\boldsymbol{x}, t)}{\partial t} = -\boldsymbol{u} \cdot \nabla \psi(\boldsymbol{x}, t) - \lambda [(\psi(\boldsymbol{x}, t) - a(\boldsymbol{x}, t)] \; , \quad \psi(\boldsymbol{x}, t_0) = a(\boldsymbol{x}, t_0) \tag{2.19}$$

in combination with

$$\delta_a(\boldsymbol{x}, t) = a(\boldsymbol{x}, t) - \psi(\boldsymbol{x}, t) \; . \tag{2.20}$$

Both formulations, that is, Equation (2.18) and Equations (2.19) and (2.20), represent an advection–relaxation problem, which can be solved on an Eulerian grid using standard numerical methods. As pointed out earlier, the formulation in Equations (2.19) and (2.20) is potentially easier to use in practice because the inhomogeneous term on the right-hand side is a instead of $\dot{a}$.

The formulation in Equations (2.19) and (2.20) constitutes the basis of what we call our tracer method. This method involves the advection of a passive tracer field $\psi(\boldsymbol{x}, t)$, the values of which are gradually relaxed towards the field $a(\boldsymbol{x}, t)$. The major advantage of the relaxation is that it fades out the past "on the fly" and thus allows one to carry on with the integration uninterrupted over an unspecified and potentially very long period of time; in other words, there is no need for any reinitialisation. This avoids any recalculation of overlapping time intervals, making the tracer method potentially very efficient in certain cases. Unfortunately, there is no option to choose the weighting kernel representing the gradual fade-out of the earlier parcel information freely; rather, the inclusion of the relaxation term in the differential equation simply results in an exponential kernel in the

solution. However, the decay time associated with this exponential kernel can be controlled by the user via the parameter λ.

Note that the interpretation of the resulting fields in terms of accumulated Lagrangian information during a specific time interval requires that the integration time is considerably longer than λ^{-1}. As a consequence, we consider the time $t \leq t_{\text{spinup}} = \lambda^{-1}$ as a spinup time. For integration times shorter than t_{spinup}, the effective window size for accumulation from the past increases with t, while for integration times longer than t_{spinup} the effective window size becomes independent of t. The latter property is desirable for a consistent interpretation of the results.

2.3 Technical implementation

Obviously, there are various options for the numerical implementation of the general method outlined above. The optimum choice is likely to depend on the type of input data, whether they are regional or global, two-dimensional or three-dimensional, and so forth. In the following, we present the algorithm chosen for this work along with the input data we use.

2.3.1 Pseudospectral algorithm

Our algorithm is designed to solve the advection–relaxation problem of Equations (2.19) and (2.20)[1] for given gridded data on a three-dimensional, global, atmospheric domain. We apply the pseudospectral method (Orszag, 1972), which uses grid-point-based as well as spectral field representations. The algorithm's key characteristics are the following (see the pseudocode in Figure S2.1 for illustration).

- Input fields are given on a global regular latitude–longitude grid with a height coordinate that is terrain-following in the lower troposphere.
- Horizontal spatial derivatives are computed in spectral space using a series expansion in spherical harmonics with triangular truncation. This representation implies a uniform spatial resolution over the entire globe, which is beneficial in terms of numerical stability (Durran, 2010).
- The vertical gradient is approximated by second-order centred differences.
- Product terms of fields are computed in physical space.

[1] Later, the algorithm has been adapted to also solve the problem in the form of Equation (2.18).

- Time integration is performed in spectral space using the explicit third-order Runge–Kutta scheme proposed by Williamson (1980).

- For numerical stability, a hyperdiffusion term of the form $D = -\nu \cdot \nabla^4 \psi$ (with ν being the diffusion coefficient) is added to the right-hand side of Equation (2.19). The term compensates for aliasing errors that are inherent in pseudosepctral methods and can cause nonlinear instabilities (Durran, 2010). In spectral space, the term $\nabla^4 \psi$ can be evaluated in a straightforward manner, as the spherical harmonics are eigenfunctions of the Laplacian operator on the sphere. Generally, we try to keep the amount of hyperdiffusion as low as possible. As a consequence, we choose the magnitude of ν dependent on the grid spacing, since a finer horizontal grid spacing turns out to require less hyperdiffusion for numerical stability. We determined the minimum necessary amount of hyperdiffusion by trial and error and found $\nu = 3 \times 10^{13}\,\mathrm{m^4\,s^{-1}}$ and $\nu = 3 \times 10^{14}\,\mathrm{m^4\,s^{-1}}$ for horizontal resolutions of 0.5° and 1°, respectively, to be acceptable for our application.

To be sure, the algorithm could be fine-tuned and improved with respect to accuracy, stability, or efficiency. In particular, our algorithm is limited by the requirement of a relatively small time step to ensure numerical stability. The use of more advanced methods such as implicit or semi-implicit schemes would allow a much larger time step, which presumably leads to enhanced efficiency. However, we did not attempt any further optimisation in this regard, since the focus of this article is on proof of concept and illustration of the method.

2.3.2 Application to reanalysis data

We apply our algorithm to data from ERA5 (Hersbach et al., 2020). ERA5 is the latest reanalysis product of the European Centre for Medium-Range Weather Forecasts, providing hourly estimates of a large number of atmospheric, land, and oceanic variables. Unless noted otherwise, we retrieved the data (Hersbach et al., 2017; Hersbach et al., 2023b) with a horizontal resolution of 1° and a temporal resolution of 3 hours. Since required by our algorithm, we interpolated the data linearly to smaller time steps. In the vertical, we use the ERA5 hybrid model levels (Simmons and Burridge, 1981; ECMWF, 2016). In our applications, we restricted ourselves to the lowest 88 model levels, which encompass the entire troposphere as well as the lower stratosphere. To generate the final output, we performed a linear interpolation from model levels to pressure levels.

2.4 Comparison with trajectories

The traditional technique to retrieve Lagrangian information from grid-point-based data involves the computation of trajectories, and there is a large body of literature where this technique has been applied successfully (see references in Section 2.1). Since our new method also aspires to provide Lagrangian information, it seems desirable to compare these two methods. We do this by first highlighting the conceptual relationship between the two methods, and second comparing the results of our method with results from trajectory calculations for the special case of no relaxation (i.e. $\lambda = 0$). This comparison allows us to test the core of our developed pseudospectral algorithm, namely the advection of tracer fields, and to point out limitations of the methods generally.

2.4.1 Conceptual relationship between the tracer method and the trajectory method

Any trajectory is meant to represent the location $\boldsymbol{X}(t)$ of a parcel in three-dimensional space at time t. As pointed out later, this concept is well-defined as long as the parcel is infinitesimally small. The trajectory is obtained through

$$\boldsymbol{X}(t) = \boldsymbol{X}(t_0) + \int_{t_0}^{t} \mathbf{U}(t')dt' \,, \tag{2.21}$$

where $\mathbf{U}(t)$ denotes the three-dimensional wind at the parcel's location at time t. In typical applications, $\mathbf{U}(t)$ is not known a priori; rather the flow is given in Eulerian representation $\boldsymbol{u}(\boldsymbol{x}, t)$, that is, on a regular spatial grid at discrete points in time. In that case, the integrand $\mathbf{U}(t')$ must be obtained by interpolation in space and time.

The knowledge of a trajectory allows one to retrieve detailed information about the respective parcel. In particular, the zonal, meridional, and vertical displacements are given by

$$\Delta_X(t) = X(t) - X(t_0), \;\; \Delta_Y(t) = Y(t) - Y(t_0), \;\; \Delta_Z(t) = Z(t) - Z(t_0) \,, \tag{2.22}$$

respectively, thus providing information about $\Delta_X(t)$, $\Delta_Y(t)$, and $\Delta_Z(t)$ at any time in the history of the parcel. Other Lagrangian displacements can be obtained by integrating the respective variable in time as the parcel travels along its trajectory. Per design, this information is restricted to the points on the trajectory, which is a one-dimensional manifold. To obtain information about an atmospheric volume at a given time, one has to consider a large number of trajectories that terminate in the volume of interest at that time. In addition, since usually the flow field is nonstationary, this computation has to be repeated many times. In theory this is straightforward, and even in practice it has

been shown to work well, given modern computing infrastructures and the possibility of parallelisation (e.g. Madonna et al., 2014; Škerlak et al., 2014; Kremer et al., 2020). However, in certain situations we suggest that our method based on Eulerian tracer fields provides a more convenient approach.

The main advantage of our tracer method lies in the fact that it provides accumulated Lagrangian information in the form of gridded fields available at any time step. Potentially, this allows one to analyse large data sets such as reanalysis data or output from climate models using standard Eulerian techniques without the need for any data preparation beforehand. The trade-off is that our Eulerian method does not yield time-resolved information along parcel trajectories; rather, it only provides accumulated Lagrangian information about the recent past, where "recent past" is determined by the time-scale λ^{-1}. In addition, each Lagrangian property requires its own tracer variable. However, as long as the number of properties is not too large, the increase in computational cost is modest. We thus conclude that our tracer method could facilitate the Lagrangian analysis substantially in those situations where the focus is on accumulated information about a modest number of parcel properties. For specific research questions, our tracer method should, therefore, be a useful tool complementing the trajectory method—even though in principle trajectories allow one to retrieve the same information.

2.4.2 Calculation of pseudotrajectories

As explained above, the tracer method and the trajectory method do not provide exactly the same information. Thus, in an attempt to compare the two methods this requires one to either map the results from the tracer method to those of the trajectory method, or vice versa. Here, we choose the first way and explain below how we extract information from the tracer method in such a way that it can directly be compared to the trajectory method. Note that this exercise requires quite some effort and is carried out exclusively for the purpose of comparison and validation. The explicit calculation of particle trajectories is and remains the core competence of the trajectory method.

The computation of a backwards trajectory provides time-resolved information about the location of the parcel that eventually reaches a specific grid point at time t. For instance, storing the parcel's location every 3 hours during the integration, one obtains the relevant Lagrangian information at times t, $t-3$ hours, $t-6$ hours, $t-9$ hours, and so forth. Figure 2.1a serves for illustration. We can extract the same information from our tracer method by applying the method in a somewhat unorthodox way. First, as mentioned before, we set $\lambda = 0$, because the computation of traditional trajectories does not involve any relaxation and the associated memory about parcel properties is effectively assumed to be infinite. Using a separate tracer for each of the three geometric dimensions,

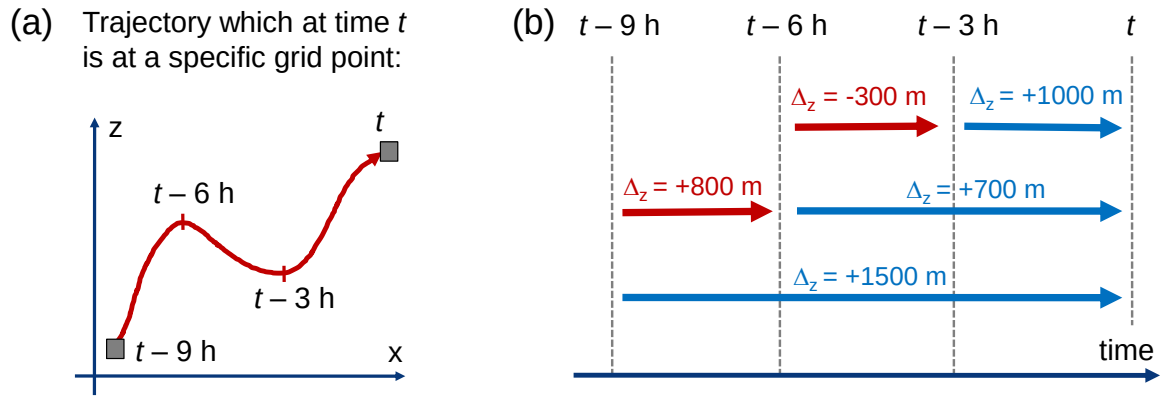

Figure 2.1 – Schematic to illustrate the computation of pseudotrajectories from the Eulerian tracer method. Panel (a) depicts a true trajectory, which intersects a specific grid point at time t. The blue arrows in panel (b) represent three different runs with our tracer algorithm, spanning durations of 3, 6, and 9 hours, respectively, with the integration ending at time t for all three simulations. The values of Δ_z associated with each blue arrow in panel (b) represent the vertical displacement for the respective time interval associated with the arrow, in qualitative agreement with the sketch in panel (a). The red arrows in panel (b) represent information obtained from difference formation between two neighbouring tracer runs.

we are able to describe the net parcel displacement in each spatial direction at any given grid point: $\delta_x(\boldsymbol{x}, t)$, $\delta_y(\boldsymbol{x}, t)$, $\delta_z(\boldsymbol{x}, t)$. However, by design these Eulerian fields only provide aggregated parcel information: they represent the net displacement in each of the variables over the duration of the entire integration (see Equation (2.5)). Of course, this information is less detailed than what can be obtained from the true trajectory with output every 3 hours.

Without careful consideration, it may seem as if the issue could be addressed by splitting the Eulerian integration into segments of 3 hours duration, since this procedure would yield the displacements during each of the 3-hour time intervals, which could then be concatenated. Unfortunately, however, this concatenation would not be straightforward, since the tracer method (only) provides information at grid points, whereas the parcel travels along the true trajectory and is almost never located right at a grid point except (by construction) at the final time.

We circumvent this problem in the following way. Consider a specific grid point for which a backward trajectory was computed (Figure 2.1a). We now perform several independent integrations of increasing length (3, 6, and 9 hours, ...) that span the time intervals $[t - 3 \text{ hours}, t]$, $[t - 6 \text{ hours}, t]$, $[t - 9 \text{ hours}, t]$. These integrations are represented as blue arrows in Figure 2.1b; they provide information about the net displacement of the parcel along the true trajectory during the corresponding time intervals $[t - 3 \text{ hours}, t]$,

$[t - 6 \text{ hours}, t]$, $[t - 9 \text{ hours}, t]$, and so forth. The displacements associated with the 3-hour segments along the trajectory can then be obtained from the differences between the net displacements of adjacent intervals (red arrows in Figure 2.1b). We refer to the procedure described as the calculation of "pseudotrajectories". Note that we calculate *backwards* pseudotrajectories by integrating forward in time. To the extent that the tracer advection is not fraught by substantial numerical diffusion, the pseudotrajectories should yield very similar results to traditional trajectories.

2.4.3 Comparison of pseudotrajectories with traditionally computed trajectories

We are now going to compare traditional trajectories with pseudotrajectories using data from a specific episode. The chosen episode contains cyclone Vladiana, which crossed the Atlantic in September 2016 (Schäfler et al., 2018) and exhibited a strong warm conveyor belt (Oertel et al., 2019). The latter was associated with large vertical displacements, which makes it a suitable case for our purpose.

First, we calculated an ensemble of traditional trajectories with the well-established Lagrangian analysis tool LAGRANTO (Wernli and Davies, 1997; Sprenger and Wernli, 2015). The ensemble encompasses backwards trajectories initialised on 25 September 2016 at 12 UTC over central Europe (20° W–50° E and 40°–90° N) on multiple vertical levels in the troposphere. We computed the trajectories from three-hourly ERA5 data on a grid with 0.5° horizontal resolution. We then calculated pseudotrajectories with our tracer method; for that purpose we used a grid of either 0.5° or 1° horizontal resolution, allowing us to test the sensitivity of our results with respect to grid spacing. The results from the comparison are presented in the following two subsections, in which we focus on relatively short and relatively long integration times, respectively.

2.4.3.1 Comparison for short integration times

We start the comparison using a situation with a relatively short integration time of two days. As detailed in the next section, on such a short time-scale the concept of an air parcel can generally be considered as sound for synoptic-scale flow; moreover, the error of a trajectory is likely to be small (e.g. Stohl et al., 2001), such that the trajectory method can be regarded as "ground truth".

The right column in Figure 2.2 depicts two-day LAGRANTO backwards trajectories terminating at a specific location over the Atlantic. The same figure also shows the corresponding pseudotrajectories calculated with the tracer method, using the two different grid spacings. The figure indicates that, for all three variables considered, the different

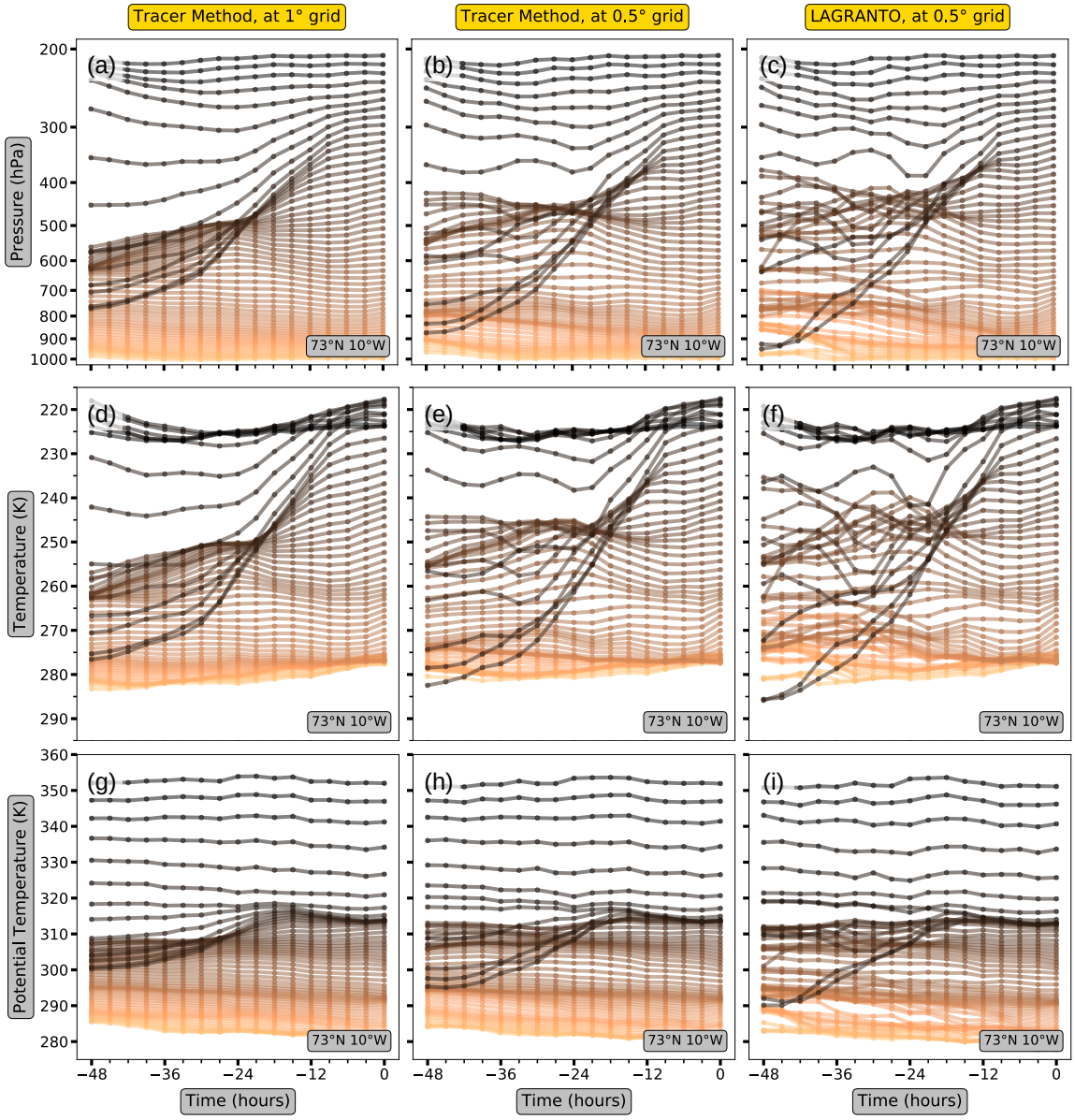

Figure 2.2 – Comparison between pseudotrajectories and LAGRANTO trajectories. The figure shows two-day backwards trajectories at 73° N 10° W for 25 September 2016 at 12 UTC. The horizontal axis represents time relative to this date. The evolution is depicted in terms of (a–c) pressure, (d–f) temperature, and (g–i) potential temperature. (a,d,g) Pseudotrajectories calculated on a grid with 1° horizontal resolution. (b,e,h) Pseudotrajectories calculated on a grid with 0.5° horizontal resolution. (c,f,i) LAGRANTO trajectories calculated on a grid with 0.5° horizontal resolution.

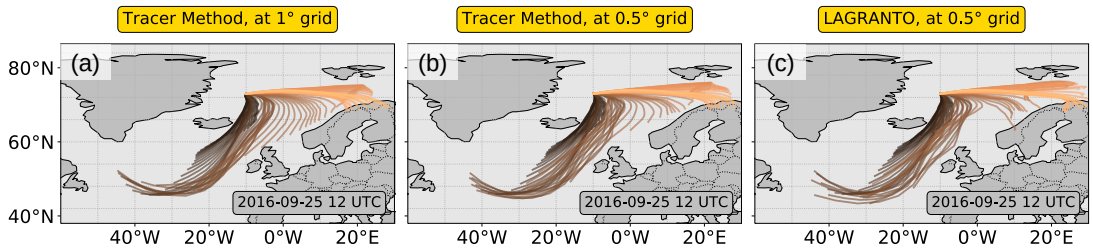

Figure 2.3 – Horizontal maps illustrating the pseudotrajectories and the LAGRANTO trajectories, respectively, from Figure 2.2. The colours denote the terminating pressure level and correspond to the colours used in Figure 2.2a–c.

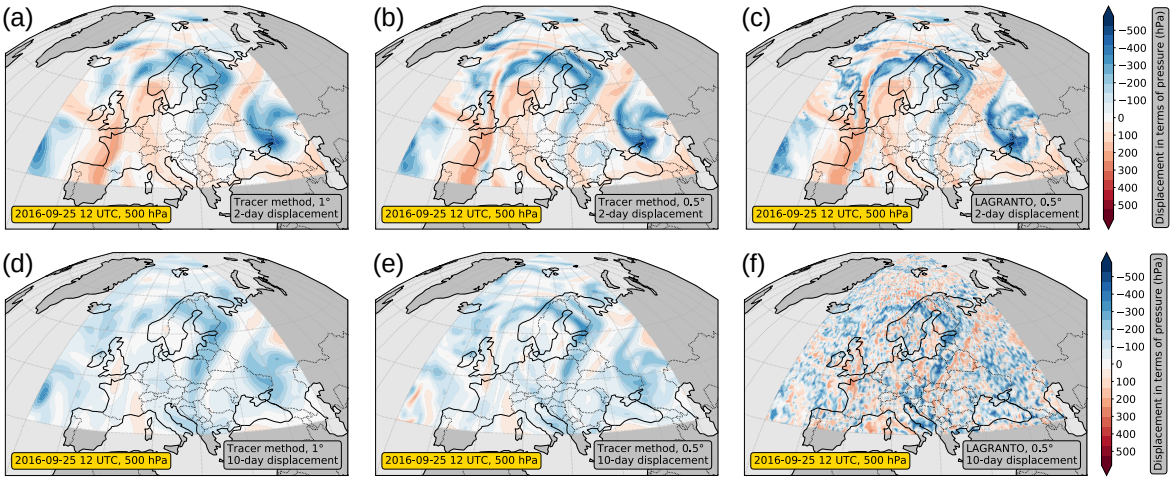

Figure 2.4 – Comparison of displacement in terms of pressure within (a–c) two days and (d–f) 10 days for 25 September 2016 at 12 UTC at a level of 500 hPa. (a,d) Results from the tracer algorithm with $\lambda = 0$ computed on a grid with 1° horizontal resolution. (b,e) Results from the tracer algorithm with $\lambda = 0$ computed on a grid with 0.5° horizontal resolution. (c,f) Results from LAGRANTO computed on a grid with 0.5° horizontal resolution.

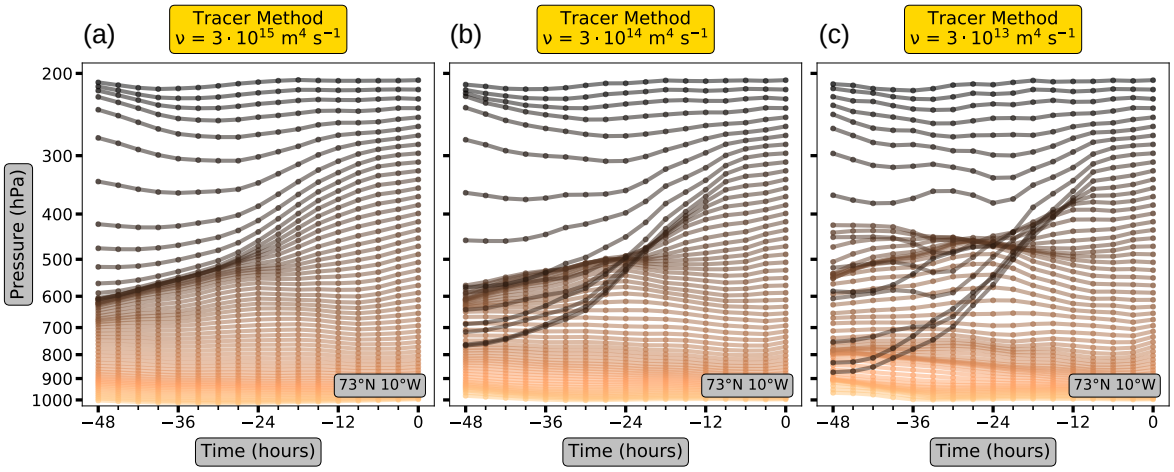

Figure 2.5 – Sensitivity of pseudotrajectories with respect to the diffusion coefficient ν. All three panels show the Lagrangian evolution in terms of pressure along two-day backwards pseudotrajectories for 25 September 2016 at 12 UTC at 73° N 10° W calculated with the tracer algorithm on a grid with 0.5° horizontal resolution. (a) $\nu = 3 \times 10^{15}\,\mathrm{m^4\,s^{-1}}$. (b) $\nu = 3 \times 10^{14}\,\mathrm{m^4\,s^{-1}}$. (c) $\nu = 3 \times 10^{13}\,\mathrm{m^4\,s^{-1}}$.

methods yield similar results: they all show a pronounced Lagrangian decrease in pressure (Figure 2.2a–c), indicating strong ascent of air masses from the boundary layer to the upper troposphere within the warm conveyor belt of Vladiana. This ascent is accompanied consistently by strong cooling (Figure 2.2d–f), attributable to adiabatic expansion, and diabatic warming (Figure 2.2g–i), attributable to condensation of water vapour (e.g. Eckhardt et al., 2004; Madonna et al., 2014). Furthermore, both the pseudotrajectories and the LAGRANTO trajectories are very consistent with regard to their horizontal patterns (Figure 2.3). For yet another perspective, in Figure 2.4a–c we show horizontal maps of the net displacement in terms of pressure at 500 hPa after two days of integration. Again, all three panels exhibit similar behaviour, showing consistent displacements in terms of pressure. The overall good agreement between the pseudotrajectories and the LAGRANTO trajectories for short integration times provides confidence that our implementation of the tracer method works adequately from a technical perspective.

Despite the overall good agreement, there are also systematic differences: the results obtained from the pseudotrajectories are generally smoother than the results obtained from the LAGRANTO trajectories, especially when using the coarser grid for the pseudotrajectories. The underlying reason for this difference is the fact that the pseudotrajectories are based on an Eulerian technique, that is, tracer advection on an Eulerian grid, and Eulerian techniques are generally known to be subject to diffusion. Part of the diffusion is numerical diffusion, and another part in our algorithm is due to the hyperdiffusive term that we incorporated for numerical stability. As described earlier, we adjusted the coefficient ν to the horizontal resolution with the aim of minimising the amount of hyperdiffusion. We

therefore tested the effect of the magnitude of ν on a fixed grid. Figure 2.5 reveals that, indeed, the observed ascent within the warm conveyor belt depends on the magnitude of ν, with stronger ascent for weaker hyperdiffusion. The hyperdiffusion is a drawback of our algorithm, but unavoidable in its current implementation. A less diffusive advection algorithm would be desirable, especially for the coarser grid resolution; however, we will never be able to eliminate effects from numerical diffusion completely, because the tracer method is an Eulerian technique by design.

2.4.3.2 Comparison for longer integration times including the discussion of limitations

We now proceed with the method intercomparison for longer integration times. For an integration time of 10 days, the displacement fields obtained from LAGRANTO trajectories look spotty and rather detailed (Figure 2.4f), while the inherent diffusion of our tracer method yields considerably smoother fields (Figure 2.4d,e). These differences are more substantial than those that we found for short integration times. We do not consider this fact as an indication of failure of either method, but the results from both methods are now likely to be subject to uncertainties and depend on the underlying assumptions. In particular, it is not so clear any longer whether the trajectories can be used as "ground truth", as we did for short integration times.

Assessing and validating Lagrangian information is difficult. In contrast to Eulerian fields produced by a numerical model, Lagrangian diagnostics can hardly be observed or measured directly. Sometimes in situ or satellite observations of chemical tracer concentrations such as ozone or carbon monoxide could be used as a reference; however, it is sometimes difficult to extract the desired Lagrangian information from chemical tracers such as diabatic heating or meridional displacement. Therefore, we refrain from such a comparison here; instead, we aim to sketch the limitations of both methods in order to facilitate a safe interpretation of the results.

Limitations generally arise from computational errors as well as conceptual assumptions, both of which may become critical for long integration times. Computational errors (that is, inaccuracies in the numerical solution) result from errors in the underlying wind field, limited spatial and temporal resolution of the wind field, and errors due to finite-difference approximations. The contribution from the finite-difference approximations is likely to be larger for the tracer method than for the trajectory method, owing to the numerical diffusion inherent in grid-point-based techniques. Stohl (1998) estimate that the computational error of a trajectory amounts on average to 20% of the distance a parcel has travelled after a few days. In this context, errors resulting from the numerics are

generally considered to be much smaller than those resulting from the representation of the wind field (Stohl et al., 2001).

Despite rather small computational errors, the trajectory method sometimes fails to explain observed phenomena without any apparent reason (Stohl et al., 2002). This problem is likely to arise from the implicit assumption that air parcels are infinitesimally small. In reality, any air parcel takes up a finite volume; the latter implies that the value of a variable at the location of the parcel is not properly defined any longer, because it may vary over the volume of the parcel. The issue is highly relevant in flows with deformation, where parcels may be stretched out into thin filaments of exponentially increasing length. This effect is often referred to as "stirring" (e.g Haynes, 1999; Haynes, 2005) and implies that after some time each parcel samples widely different regions of the atmosphere and cannot be considered as representative of a specific point in space any longer. By that time, the concept of a parcel has lost its proper meaning. The issue is particularly severe in the case of flow bifurcations, as illustrated beautifully by Welander (1955; their Figures 2 and 3). On top of that, filamentation resulting from stirring may ultimately lead to "true mixing", which is the homogenisation of tracer fields by molecular diffusion (e.g Haynes, 1999; Haynes, 2005). Thus, the notion of a trajectory becomes—sooner or later—meaningless.

Quantifying trajectory uncertainty owing to the process of filamentation is difficult. Stohl et al. (2002) try to provide an estimate based on trajectory simulations with a particle dispersion model. They find the average uncertainty to be of the order of 20%–40% of the distance a parcel travelled after 10 days and state that "this is more than the errors resulting from wind field analysis, interpolation, and numerical truncation errors." Of course, these values should only be seen as a rough estimate; they may vary strongly with the size of the air parcels as well as the specific flow situation. However, filamentation as a result of stirring seems to be of vital importance when interpreting the significance of trajectories.

2.4.4 The role of the relaxation term

We close the section by highlighting the role of the relaxation term of our tracer method. This term does not usually appear in traditional trajectories methods. As explained in Section 2.2.1, the relaxation term effectively introduces an exponential weighting kernel, such that the "recent past" is accounted for to a larger extent than the "distant past" in the parcel's memory for its displacement. Translated into the framework of trajectory uncertainty, this means that information from the "recent past", which is generally less prone to error, is accounted for with a larger weight than information from the more "distant past", which is generally more prone to error. This design feature can thus

be interpreted as a way of accounting for uncertainty in the parcel's memory for its displacement. Owing to the exponential kernel function, the transition between "recent" and "distant" is gradual, which is desirable, as the growth of errors along trajectories is likely to be gradual rather than abrupt. Of course, the interpretation of the relaxation as a suppression of the accumulating errors has to be taken with some caution, because error growth may be flow-dependent, which is not accounted for with a fixed relaxation constant. A future implementation of our method may account for a flow-dependent value of λ, for example, as a function of the shear or the deformation of the wind field. However this is beyond the scope of the present article.

2.5 Illustration of the method

In the following, we are going to illustrate the intended use of our tracer method, which is to employ the method with a relaxation constant $\lambda > 0$. We exemplify this on the basis of a few simple examples. The first two examples link displacements in terms of pressure and parcel-based diabatic temperature changes to patterns in cloud fractions (similar to Schär and Wernli, 1993), while the third and forth examples relate meridional displacements to patterns in temperature anomalies and the Lagrangian mean circulation. In all examples we apply a relaxation constant of $\lambda^{-1} = 3$ days. Finally, we discuss the sensitivity of the results to the choice of this parameter. Our examples are qualitative in nature and meant to be intuitive in order to inspire the reader to further analysis.

2.5.1 Example 1: The vertical displacement and its relation to clouds

A prominent feature of the Earth's atmosphere is the occurrence of clouds. Clouds form in many parts of the atmosphere: for instance cyclones, convective systems, or the vicinity of orography. Figure 2.6a–c shows an example of the evolution of cloud fractions in the upper troposphere. The question we want to address here is whether we can understand, to some extent, why the patterns in the field of cloud fraction look as they do.

Although the details of cloud formation are complex, involving various processes all the way to the microphysical scale, a major forcing mechanism is simply ascending motion. Ascent is associated with decreasing pressure and adiabatic cooling, which increases relative humidity and eventually leads to saturation. Once formed, clouds often behave like a tracer, that is, they get advected by the wind, as long as they do not rain out or dissolve through adiabatic compression in descending motion. Thus, to broadly understand the patterns of cloud fractions in Figure 2.6a–c, one needs to diagnose which of the air masses have undergone ascent versus descent in the recent past. By contrast, instantaneous vertical wind fields (Figure 2.6d–f) do not provide this kind of insight, since they only

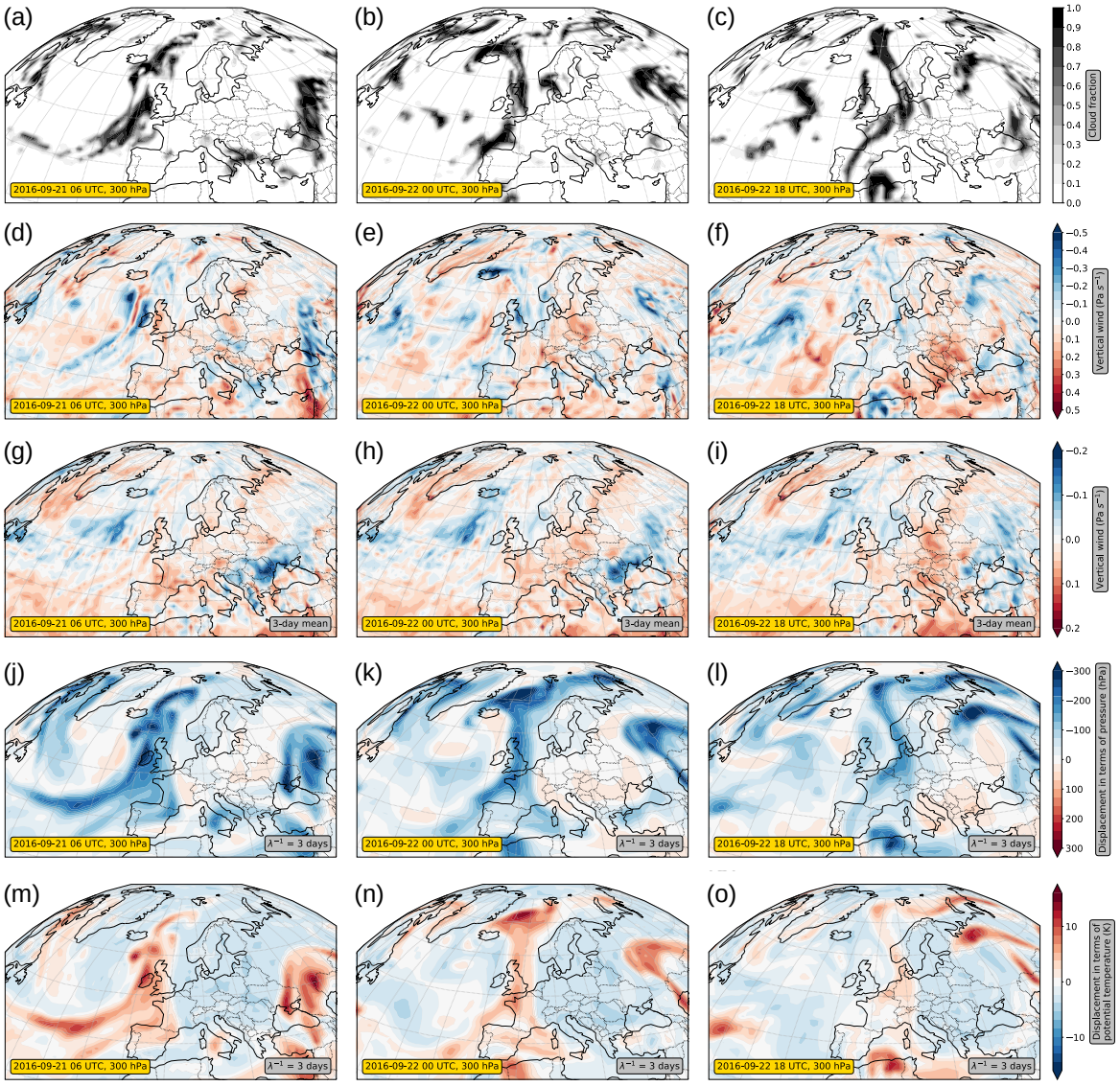

Figure 2.6 – Utility of the tracer method as a diagnostic for cloud occurrence. The figure shows horizontal cross-sections at 300 hPa for three consecutive dates in September 2016. (a–c) Cloud fraction from reanalysis (Hersbach et al., 2023a). (d–f) Vertical wind from reanalysis. Blue denotes ascent, whereas red denotes descent. (g–i) Three-day mean vertical wind from reanalysis; colours as in panel (d–f). (j–l,m–o) Two tracer diagnostics computed with a relaxation constant of $\lambda^{-1} = 3$ days. (j–l) shows the displacement in terms of pressure; blue denotes ascended air masses, whereas red denotes descended air masses. (m–o) depicts the displacement in terms of potential temperature; blue denotes diabatically cooled air masses, whereas red denotes diabatically heated air masses.

contain information about the instantaneous vertical motion, but not the (recent) past. Similarly, wind fields that have been time-averaged on the Eulerian grid (Figure 2.6g–i) are inappropriate because they lack parcel-based information. Both deficiencies can be overcome by using a Lagrangian method such as the tracer method.

Applied to the variable pressure, the tracer method yields the accumulated change of pressure along a parcel's trajectory. Usually, this Lagrangian change in terms of pressure can be taken as a proxy for the Lagrangian change in altitude. Correspondingly, the Lagrangian change or "displacement" in terms of pressure indicates which of the air masses have undergone ascent or descent in the recent past (Figure 2.6j–l). Besides small differences, the displacement in terms of pressure indeed resembles the cloud fractions and their evolution in Figure 2.6a–c. Cloudy regions mostly coincide with air masses that have undergone major ascent, whereas cloud-free regions mostly coincide with air masses that have undergone only slight ascent or even descent. With our tracer diagnostic we can, thus, demonstrate that ascending motion is indeed a major forcing mechanism for the formation of clouds.

2.5.2 Example 2: The parcel-based diabatic temperature change and its relation to latent heat release

Further insight into Example 1 can be obtained by considering an additional tracer, namely potential temperature. Similarly to the displacement in terms of pressure, the displacement in terms of potential temperature (Figure 2.6m–o) marks those air masses that have undergone diabatic heating or cooling, respectively, in the recent past. The plots reveal strong signs of diabatically heated air masses mainly in cloudy regions, consistent with the latent heat release associated with the cloud formation process during the recent past. By contrast, diabatically cooled air masses are mostly correlated with cloud-free areas, consistent with the general tendency towards radiative cooling of the free atmosphere.

2.5.3 Example 3: The meridional displacement and its relation to temperature anomalies

In the following, we want to illustrate that temperature anomalies in the extratropics are sometimes strongly associated with horizontal temperature advection. We address this topic from a Lagrangian point of view, linking horizontal temperature advection to meridional parcel displacements.

As an example, Figure 2.7a–c shows temperature anomalies in the lower troposphere for a six-day period in September 2016, which was associated with quite large warm anomalies over Europe (Zschenderlein et al., 2018). In particular, on 6 September (Figure 2.7a),

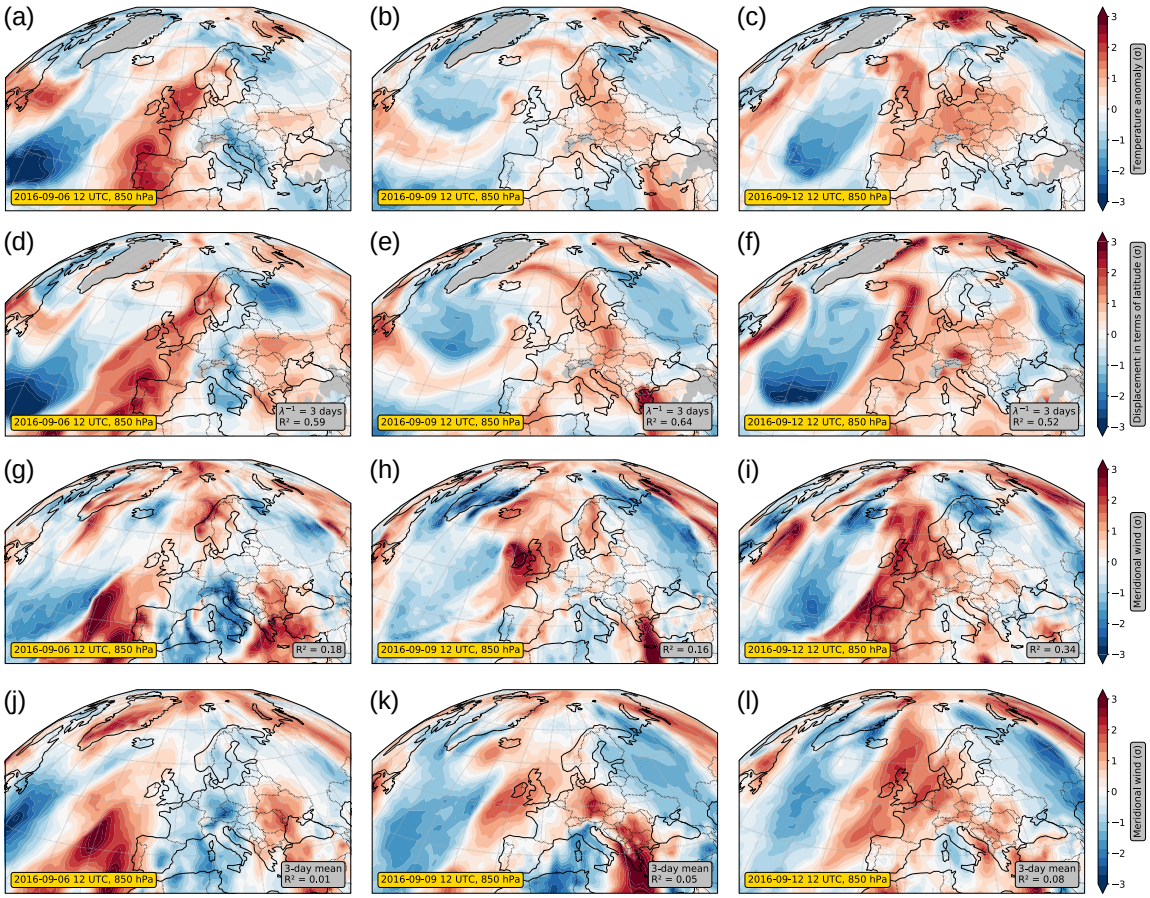

Figure 2.7 – Utility of the tracer method as a diagnostic for the occurrence of temperature anomalies. The figure shows horizontal cross-sections at a level of 850 hPa for three dates in September 2016. All variables are depicted in terms of normalised anomalies indicating the standard deviation from the two-month average of August and September 2016. R^2 denotes the squared correlation coefficient, which quantifies the quality of the correlation between the respective field and the temperature field. For the computation of R^2, data points between 40°–60° N and 50° W–50° E were considered. (a–c) Temperature from reanalysis. (d–f) Meridional displacement computed with a relaxation constant of $\lambda^{-1} = 3$ days; blue denotes air masses that have been anomalously displaced southward, whereas red denotes air masses that have been anomalously displaced northward. (g–i) Meridional wind from reanalysis; blue denotes anomalous northerly winds, whereas red denotes anomalous southerly winds. (j–l) Three-day mean meridional wind from reanalysis; colours as in (g–i).

a tongue of unusually warm air lay over Europe, extending from France via England to Scandinavia. On 12 September (Figure 2.7c), almost all of Europe experienced significantly higher temperatures than usual. In between (Figure 2.7b), somewhat lower temperature conditions prevailed in large parts of Europe.

To find out whether and to what extent the temperature anomalies can be related to meridional parcel displacement, we apply the tracer method to a latitude tracer. The resulting fields then indicate which air masses have originated from the south and which from the north during the recent past. Given that the climatological mean temperature gradient is mostly aligned in the meridional direction, one may generally expect an anomalously strong poleward displacement to be associated with a local warm anomaly and an anomalously strong equatorward displacement with a local cold anomaly.

In order to compare the displacement fields and the temperature anomalies in a meaningful manner, we provide both as standardised anomaly fields computed as deviations from a two-month average (see Section 2.5.4). By analogy with the temperature anomaly field, the meridional displacement field then shows the extent to which it is unusual compared with the climatology. In other words, the field indicates whether air masses originate more from the north or more from the south than usual. If temperature anomalies are due to meridional advection, the two fields are thus expected to be quite similar.

Figure 2.7d–f shows that the temperature anomalies from Figure 2.7a–c can be associated, to a substantial extent, with anomalous meridional displacements over large parts of Europe. More precisely, the fields reveal that air masses originating more from the south than usual mostly coincide with temperatures warmer than usual, whereas air masses originating more from the north than usual mostly coincide with temperatures colder than usual. For example, the elongated warm tongue of air on 6 September is represented quite well by anomalous northward displacement. Likewise, the cold anomaly over the Atlantic is captured well by the meridional displacement. The same applies to the other two examples. This suggests that temperature anomalies in the extratropics can generally be related quite significantly to meridional temperature advection.

The last statement is put on a more quantitative basis by computing the correlation between the corresponding fields. The squared correlation coefficient is given in the grey boxes in each panel; for all three dates it turns out to be well above 0.5, suggesting that at least half of the variance within the temperature anomaly field is described by the meridional displacement.

Of course, there are also differences between the meridional displacement and the temperature field: for example, over France on 6 September, where the meridional displacement anomaly extends further to the east than the temperature anomaly, or over England on 12 September, where the displacement anomaly is stronger than the temperature anomaly. These differences are to be expected, since there are two other

processes that induce parcel-based temperature changes and can thus contribute generally to the occurrence of temperature anomalies: adiabatic compression in vertical air motion and diabatic processes. Furthermore, differences may arise from the fact that air masses are significantly warmer or colder at their origin than expected from the zonal mean climatology; this is not taken into account in our simple argument. In addition, our argument does not account for zonal temperature gradients. A more detailed and quantitative analysis along these lines is planned in the near future.

Finally, note that the patterns of the temperature field show a closer resemblance to the meridional displacement than either the instantaneous meridional wind (Figure 2.7g–i) or the time-averaged meridional wind (Figure 2.7j–l). This illustrates, again, the merit of a Lagrangian method such as the tracer method. The tracer method provides Lagrangian information, namely the accumulation of meridional wind at the location of the parcel, as opposed to purely local Eulerian information, which is often of less relevance for the underlying physical mechanism.

2.5.4 Example 4: The Lagrangian versus the Eulerian mean meridional circulation

As mentioned before, the grid-point-based nature of our method allows a straightforward evaluation and post-processing, as, for instance, in the computation of climatologies. To illustrate this particular feature, we computed the two-month time-averaged field of the meridional displacement (Figure 2.8a,c), based on three-hourly grid-point-based fields of the meridional displacement of August and September 2016.

The time-averaged meridional displacement field reveals that the outcome of the tracer method is of truly Lagrangian nature, although the method itself is Eulerian from a technical point of view. The meridional displacement (Figure 2.8a) shows equatorward parcel displacements in the lower troposphere and poleward parcel displacements in the upper troposphere, with the displacement in the winter hemisphere being stronger than that in the summer hemisphere. The time-averaged meridional displacement thus has similar characteristics to the global Lagrangian mean circulation as diagnosed from the transformed Eulerian mean formalism (e.g. compare with Edmon et al., 1980, figure 6; Iwasaki, 1989, figure 4; Juckes, 2001, figure 4) or obtained from averaging the flow on isentropes (e.g. compare with Townsend and Johnson, 1985, Figure 9; Juckes, 2001, Figure 3; Pauluis et al., 2010, Figure 1): It suggests a one-cell structure of the Lagrangian circulation in each hemisphere, with a stronger circulation in the winter hemisphere. The large values of the meridional displacement at the poles result from the fact that the poles constitute an upper and lower boundary for the meridional displacement, so that for high

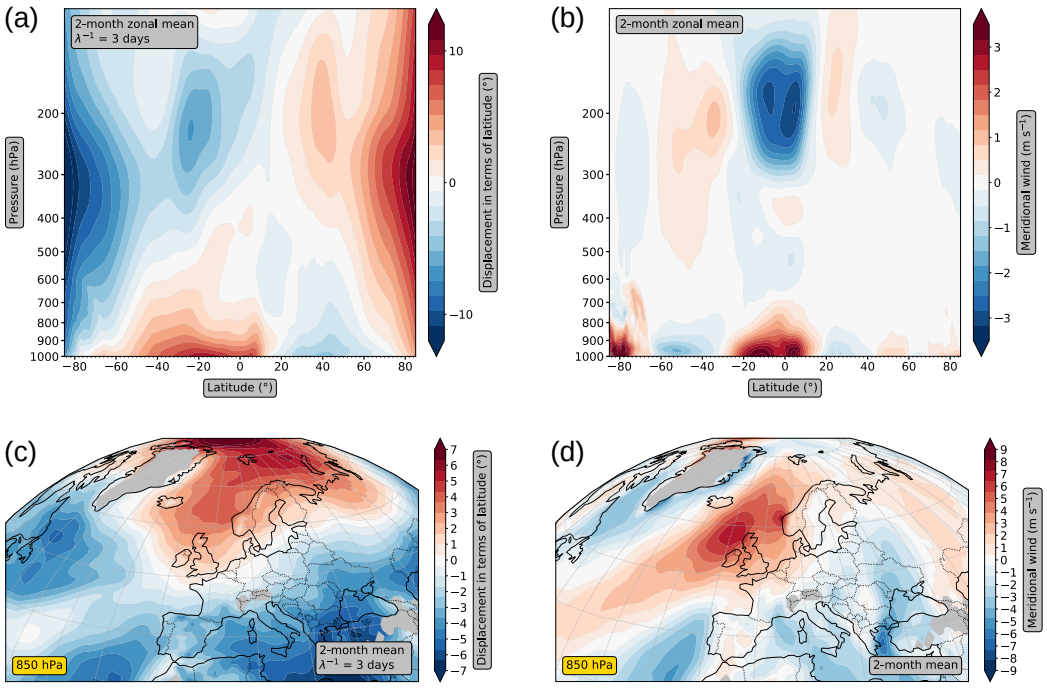

Figure 2.8 – Two-month time-averaged fields based on reanalysis data for August and September 2016. (a) Zonal mean of the meridional displacement (with $\lambda^{-1} = 3$ days); blue denotes air masses that have been displaced southward, whereas red denotes air masses that have been displaced northward. (b) Zonal mean of the meridional wind; blue denotes northerly winds, whereas red denotes southerly winds. (c) Meridional displacement at 850 hPa. (d) Meridional wind at 850 hPa.

latitudes a displacement from lower latitudes is statistically much more likely; the large values at high latitudes must, therefore, be considered as a geometric effect.

In contrast to the Lagrangian mean, the conventional Eulerian mean of the meridional wind (Figure 2.8b), exhibits the familiar three-cell structure consisting of the Hadley cell, the Ferrel cell, and the polar cell. The difference between Figure 2.8a,b highlights the power and beauty of the tracer method: it provides a Lagrangian description of the flow through a simple Eulerian zonal average of a variable that carries Lagrangian information.

Finally, note that the two-month time average is far from being zonally symmetric even in the two-month time average (Figure 2.8c); rather, it exhibits poleward parcel displacement in northern Europe and equatorward parcel displacement in southern and eastern Europe as well as over the Atlantic, which is probably related to either large-scale stationary waves or frequently recurring weather systems. Again, a qualitative difference in comparison with the mean meridional wind (Figure 2.8d) is clearly visible.

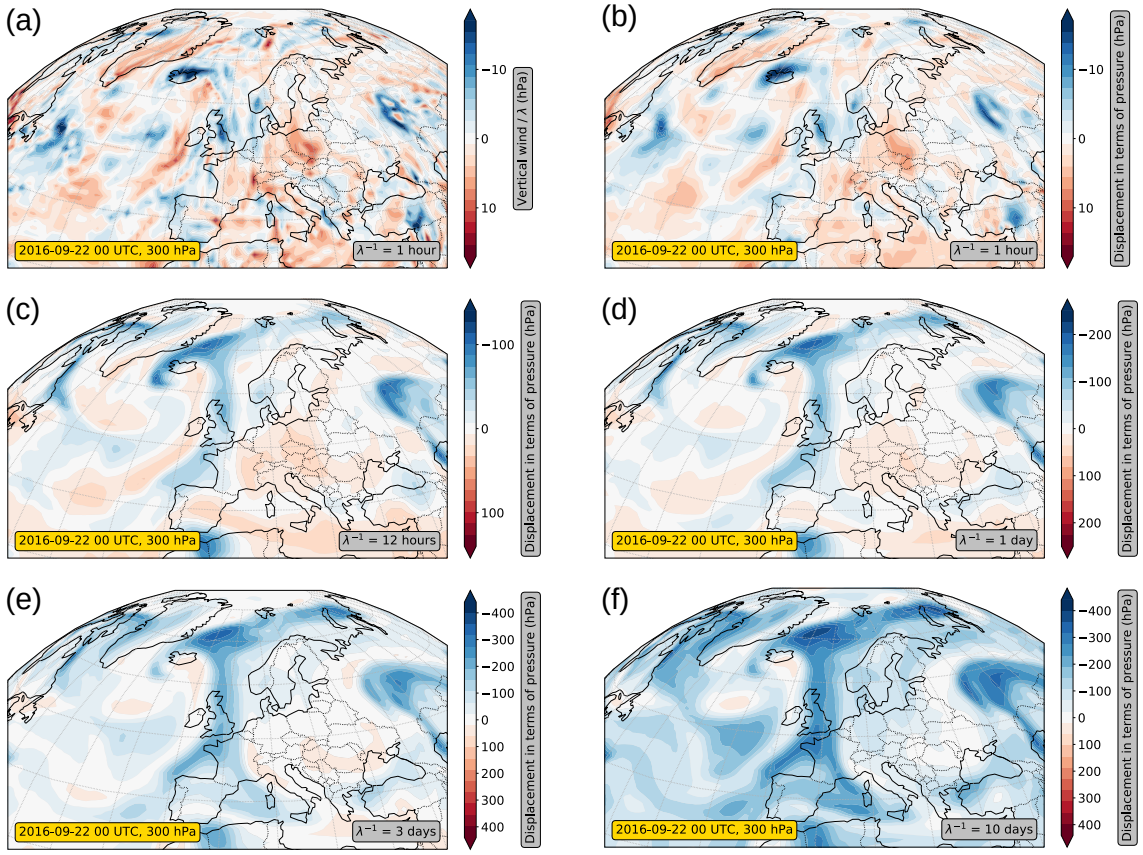

Figure 2.9 – Sensitivity of the tracer method with respect to the relaxation constant λ illustrated in the framework of the example from Figure 2.6. The figure shows horizontal cross-sections at 300 hPa for 22 September 2016 at 00 UTC. (a) Vertical wind divided by $\lambda = 1$ hour^{-1} . (b–h) Displacement in terms of pressure for different relaxation constants λ in the range $\lambda^{-1} = 1$ hour to $\lambda^{-1} = 10$ days.

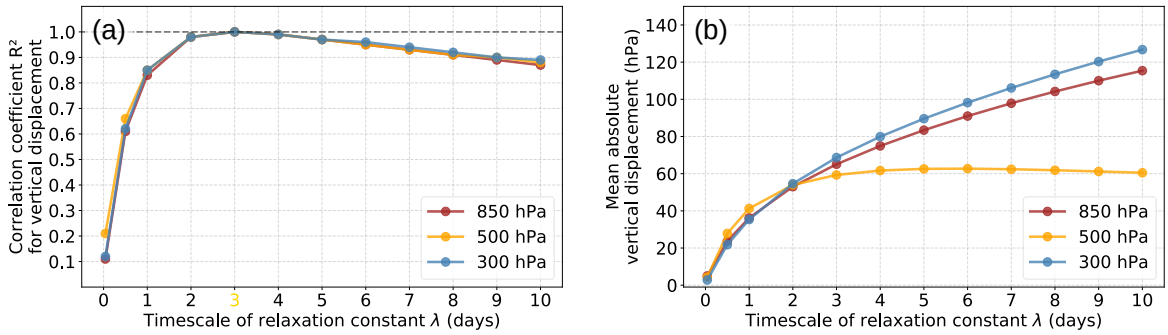

Figure 2.10 – Sensitivity of vertical displacement with respect to the relaxation constant λ depicted in terms of correlation coefficient and mean absolute displacement. (a) Squared correlation coefficient of the vertical displacement computed with $\lambda^{-1} = 3$ days and the vertical displacement computed with other values for λ. All data points between 30° and 60° N in the Northern Hemisphere at 00 UTC in September 2016 were considered. The different colours indicate different pressure levels. (b) Mean absolute vertical displacements as a function of λ^{-1}. All data points between 30° and 60° N in the Northern Hemisphere at 00 UTC in September 2016 were considered. The different colours indicate different pressure levels.

2.5.5 Sensitivity with respect to the relaxation parameter

A crucial feature of our method is the relaxation term, which determines the time-scale of accumulation to be considered. Based on two examples from above, we now examine the sensitivity of our results with respect to the relaxation parameter λ.

For this purpose it is instructive to consider, first, the limit of strong relaxation, that is, $\lambda T \gg 1$, where T denotes the time-scale on which the synoptic scale wind field changes. In this limit, Equation (2.7) can be approximated as

$$\Delta_z(t) = W(t) \int_{t_0}^{t} e^{-\lambda(t-t')}\, dt' = \frac{W(t)}{\lambda} \left[1 - e^{-\lambda(t-t_0)}\right]. \tag{2.23}$$

Assuming furthermore $\lambda(t - t_0) \gg 1$, the expression on the right-hand side becomes

$$\Delta_z(t) = \frac{W(t)}{\lambda}\,. \tag{2.24}$$

Translated to the Eulerian perspective, this result means that for strong relaxation the displacement field $\delta_z(\boldsymbol{x}, t)$ approaches the vertical wind field $w(\boldsymbol{x}, t)$ divided by λ.

The other limit of interest is the limit of weak relaxation, that is, $\lambda T \ll 1$. In this limit, Equation (2.7) turns approximately into Equation (2.5), meaning that the vertical displacement simply accumulates the vertical wind since the initial time t_0. For integrations where this time interval is much longer than the synoptic time-scale, that is, $t - t_0 \gg T$, we expect that the field $\delta_z(\boldsymbol{x}, t)$ does not provide useful information any longer, because the

parcels undergo subsequent episodes of upwelling and downwelling in a more or less random fashion, and the displacement field loses any meaningful relation to the instantaneous synoptic-scale flow. Moreover, as we pointed out above, for such long integrations the whole concept of a "parcel" becomes questionable anyway. Therefore, we refrain from taking a closer look at this limit.

Figure 2.9 confirms the above prediction for strong relaxation, based on the example presented in Section 2.5.1. In the case of strong relaxation ($\lambda^{-1} = 1$ hour, Figure 2.9b), the vertical displacement resembles, apart from a more diffusive behaviour, the vertical wind divided by λ (Figure 2.9a). Both fields diagnose, for example, distinctive upwelling over Iceland, western Russia, Turkey, and parts of the Atlantic, thereby differing significantly from the displacements obtained with λ^{-1} of no more than 12 hours (Figure 2.9c).

For larger values of λ, the qualitative appearance of the vertical displacements in Figure 2.9 is rather insensitive to the specific choice of λ. As long as λ^{-1} is smaller than the typical Lagrangian synoptic scale, the tracer essentially samples coherent air streams with steady upward or downward motion. Hence, the vertical displacements do not differ much in their patterns, but mostly in their intensity; the latter is because a weaker relaxation constant accumulates displacement information for a longer time interval. In our example, this is roughly the case for values of λ^{-1} in the range between 12 hours (Figure 2.9c) and three days (Figure 2.9e). Here, the tracer method mainly detects shorter or longer fractions of the ascent within the cyclone's warm conveyor belt, typically lasting about two days (Wernli and Davies, 1997; Eckhardt et al., 2004). Even for $\lambda^{-1} = 10$ days (Figure 2.9f), the vertical displacement field still shows broadly the same structure. However, the overall colour turns towards blue, which means that most of the parcels have experienced upwelling rather than downwelling. Given that the tropopause acts approximately as a rigid lid, this behaviour is plausible from a statistical point of view, since air parcels residing in the upper troposphere must originate, in the long term, from further below.

The foregoing can be made more quantitative as follows. We computed the spatial correlation between displacement fields associated with different values of λ and show the result in Figure 2.10a. This plot quantifies the pattern correlation between the vertical displacement field for $\lambda^{-1} = 3$ days and that for various other values of λ. This plot generalises the result from the previous figure by accounting for more than one pressure level and time step. Apparently, for very strong relaxation (small λ^{-1}), the squared correlation coefficients are low, consistent with the earlier result that the vertical displacement fields for $\lambda^{-1} = 1$ hour and $\lambda^{-1} = 3$ days differ substantially. For values of λ^{-1} in the range of 1–10 days, however, the squared correlation coefficients always exceed more than 80%, revealing a fairly strong correlation between the respective displacement fields. This

indicates, again, that the displacement fields obtained sustain a similar overall structure for quite a large range of values of λ.

While the overall patterns visible in the displacement fields in Figure 2.9 are nearly independent of λ over a broad range of values, this is not true for the typical magnitude of the fields (note the different contour intervals in the different panels). This fact is quantified further in Figure 2.10b, where we depict the mean absolute vertical displacement for the Northern Hemisphere midlatitudes as a function of λ^{-1}. Apparently, for small values of λ^{-1} (corresponding to short accumulation intervals) the magnitude of the vertical displacement increases with increasing λ^{-1}, but for larger values of λ^{-1} (corresponding to long accumulation intervals) this increase becomes more gradual or even saturates. As mentioned above, the general increase in magnitude with λ^{-1} is reasonable, since a larger λ^{-1} corresponds to a larger accumulation period. Understanding the precise shape of this curve and its dependence on altitude is beyond the scope of this article.

The meridional displacement exhibits a similar behaviour to the vertical displacement in terms of the sensitivity with respect to λ (Figure S2.2). For very strong relaxation, the meridional displacement (Figure S2.2b) represents, analogous to Equation (2.24), the meridional wind divided by λ (Figure S2.2a). For all other values of λ in that figure, the meridional displacements mostly differ in their intensity but not in their structure. Again, the same conclusion can be drawn from Figure S2.3 in a more quantitative sense.

The best choice for the relaxation parameter λ may depend, amongst other things, on the synoptic situation, the region of interest, the variable under consideration, and the specific research question. However, the observed robustness of the patterns obtained with respect to λ indicates that the exact value is of secondary importance, at least in a qualitative analysis. Furthermore, the observed robustness with respect to λ suggests that the results should be rather insensitive to the exact choice of the function used as weighting kernel in Equation (2.7). This finding justifies, a posteriori, our decision to employ an exponential kernel that corresponds to simple Newtonian relaxation in the underlying differential equation.

2.6 Summary and conclusions

In this article we proposed an Eulerian method for extracting Lagrangian information about the atmospheric flow. The method is based on the advection of passive tracer fields, which are subject to a judiciously chosen relaxation term. Mathematically, our method requires the solution of an advection–relaxation equation for a tracer field $\psi(\boldsymbol{x}, t)$ on an Eulerian grid. The tracer field $\psi(\boldsymbol{x}, t)$ can be defined through any scalar quantity that can be associated with an air parcel, such as altitude, pressure, latitude, or temperature. As

output, the method provides the accumulated Lagrangian change $\delta(\boldsymbol{x}, t)$ of the quantity considered. More specifically, the resulting field $\delta(\boldsymbol{x}, t)$ represents the Lagrangian change of the quantity considered for those air parcels that happen to be located at the respective grid points at the time of interest. The relaxation term guarantees that the accumulation time is essentially restricted to a finite length, which in a typical application is much shorter than the total integration time. The finite accumulation time effectively corresponds to an exponential decay of $\delta(\boldsymbol{x}, t)$ as one moves backward along the parcel's trajectory. This device allows us to run the integration in a continuous fashion without the need for repeated reinitialisation and, thus, leads to an efficient and convenient method for specific applications.

We implemented a pseudospectral algorithm to solve the advection–relaxation problem on a three-dimensional, global, atmospheric domain. For the purpose of validation, we switched off the relaxation term and calculated so-called pseudotrajectories, which essentially provide the same information as traditional "real" trajectories. We then compared these pseudotrajectories with real trajectories obtained with LAGRANTO. As long as the length of the integration time is not much longer than the time-scale of the flow phenomenon of interest, our pseudotrajectories show close resemblance to trajectories from LAGRANTO; the only systematic difference is the fact that the pseudotrajectories exhibit a more diffusive behaviour due to the grid-point-based nature of our algorithm. We interpreted this outcome as showing the correct implementation of our algorithm. Substantially larger differences appeared for time intervals that are considerably longer than the characteristic time-scale of deformation. In that case, the LAGRANTO trajectories provide spotty fields with sharp local gradients, which are familiar in the framework of "chaotic advection" (Aref, 1984; Pierrehumbert and Yang, 1992; Haynes, 1999). By comparison, our tracer algorithm yields considerably smoother fields owing to its inherent diffusion (both explicit and implicit). However, for such long time intervals the parcel approach becomes questionable, because a point cannot be taken as representative of an entire air parcel any longer; both approaches need to be considered as idealisations, and it remains unclear at this point to what extent either of them represents reality. This issue can be avoided by restricting the length of the trajectory to a finite time; in the framework of our tracer method this is effectively achieved by a finite value of λ. For synoptic-scale applications we suggest to use a value in the range $\lambda^{-1} = 1$–5 days, since this corresponds roughly to the typical time-scale of midlatitude synoptic-scale flow features.

We then demonstrated the intended use of our method with the help of a few intuitive examples related to synoptic-scale flow, using a finite relaxation constant $\lambda > 0$. The examples illustrated how our method can serve as a diagnostic tool to understand—not predict—the occurrence of certain atmospheric phenomena. For instance, in the first example we showed that observed patterns in cloud fraction correspond fairly well to the

patterns in the vertical displacement obtained from the tracer method. By contrast, the correlation with the vertical wind was considerably lower. This result is consistent with the fact that adiabatic cooling by expansion is a major mechanism for cloud formation, and that the amount of cloudiness is related to the accumulated cooling experienced by an air parcel. In another example we pointed out that meridional displacements obtained from the tracer method show some resemblance to the distribution of temperature anomalies. This correspondence indicates that horizontal advection may be an important mechanism for the formation of temperature anomalies. We also briefly considered the patterns of the time-averaged meridional displacement, which indicate a one-cell structure in the meridional plane as opposed to the more familiar three-cell structure of the Eulerian mean meridional circulation, and thus demonstrated the Lagrangian nature of the diagnosed field.

Finally, we showed that the overall patterns of the vertical and meridional displacements in our examples were similar in a fairly broad range of values for λ, but at the same time the mean amplitude was quite sensitive to λ. This result suggests that the exact choice of the relaxation constant may be uncritical for a qualitative application of the method, but that care must be exercised in quantitative applications. We are currently working to explore the utility of the method in a more quantitative sense. To be sure, a similar caveat applies to any trajectory method, where the results may depend partly on the length of the trajectory.

One major limitation of our method is the fact that it only provides Lagrangian information that is aggregated over a finite time interval. In this sense it provides less detailed information than can be achieved with trajectories. However, for certain applications aggregated information may be enough. These applications might include climatological analyses such as the Lagrangian characterisation of heat waves and warm conveyor belts, or studies regarding the waviness of the jet stream. In such applications, our method may facilitate analysis by providing continuous, volume-covering Lagrangian information as direct model output. Due to its Eulerian, grid-based nature, the method is rather easy to handle and can be applied readily to large data sets. Moreover it can easily be implemented as an online tool in traditional Eulerian models, which provides advantages such as the use of highly resolved (in time) wind information (Gheusi and Stein, 2002; Miltenberger et al., 2013). In summary, we think that our tracer method is an interesting alternative to the traditional trajectory method for certain applications and it may stimulate further investigations of atmospheric phenomena from a Lagrangian perspective.

Author contributions **Amelie Mayer**: data curation; formal analysis; investigation; methodology; software; validation; visualisation; writing – original draft; writing – review

and editing. **Volkmar Wirth**: conceptualisation; funding acquisition; investigation; methodology; project administration; supervision; writing – original draft; writing – review and editing.

Acknowledgements The research leading to the results in this article has been performed within the subproject C4 "Predictability of European heat waves" of the Transregional Collaborative Research Centre SFB/TRR 165 "Waves to Weather" (`https://www.wavestoweather.de`) funded by the German Research Foundation (DFG). We thank Alexander Lemburg and Philipp Zschenderlein for providing the LAGRANTO trajectories used in this study. Further, we thank the Copernicus Climate Change Service for granting free access to the ERA5 data. Open Access funding enabled and organised by Projekt DEAL.

2.7 Supporting information

Algorithm: Solve the advection-relaxation equation

Input: Gridded global three dimensional fields; for each computational time $t_{i,comp} \in t_{comp}$.
Fields are: $u(t)$ (zonal wind), $v(t)$ (meridional wind), $w(t)$ (vertical wind), $a(t)$ (variable which serves as tracer)

Output: Gridded global three dimensional fields; for each output time $t_{i,out} \in t_{out}$, where $t_{out} \subseteq t_{comp}$.
Fields are: $\psi(t)$ (tracer field), $\Delta_\psi(t)$ (displacement field)

$\psi \leftarrow$ read in initial tracer field $a(t_0)$
foreach $t_{i,comp}$ **do**
  U, V, $W \leftarrow$ read in fields $u(t)$, $v(t)$, $w(t)$
  $A \leftarrow$ read in field $a(t)$
  $gradU$, $gradV \leftarrow$ compute zonal and meridional gradients of ψ
  $gradW \leftarrow$ compute vertical gradient of ψ
  $advection \leftarrow U \cdot gradU + V \cdot gradV + W \cdot gradW$
  $relaxation \leftarrow \lambda \cdot (\psi - A)$
  $tendency \leftarrow -(advection + relaxation)$
  $\psi \leftarrow$integrate ψ one timestep further ...
    explicit 3rd order Runge Kutta scheme:
      $\psi \leftarrow \psi + \Delta t \cdot tendency$ ...
    implicit treatment of hyperdiffusion:
      $eig \leftarrow$ compute Laplacian eigenvalues of ψ
      $\psi \leftarrow \frac{\psi}{\Delta t \cdot \nu \cdot eig^2}$, with diffusion coefficient ν
  if $t_{i,comp} \in t_{out}$ **then**
    $\Delta_\psi \leftarrow A - \psi$
    $\psi, \Delta_\psi \rightarrow$ store fields
  end
end

Figure S2.1 – Pseudocode for the algorithm used to solve the advection–relaxation equation for given gridded data on a three-dimensional, global, atmospheric domain. For numerical reasons, the computational time step is much smaller than the output time step.

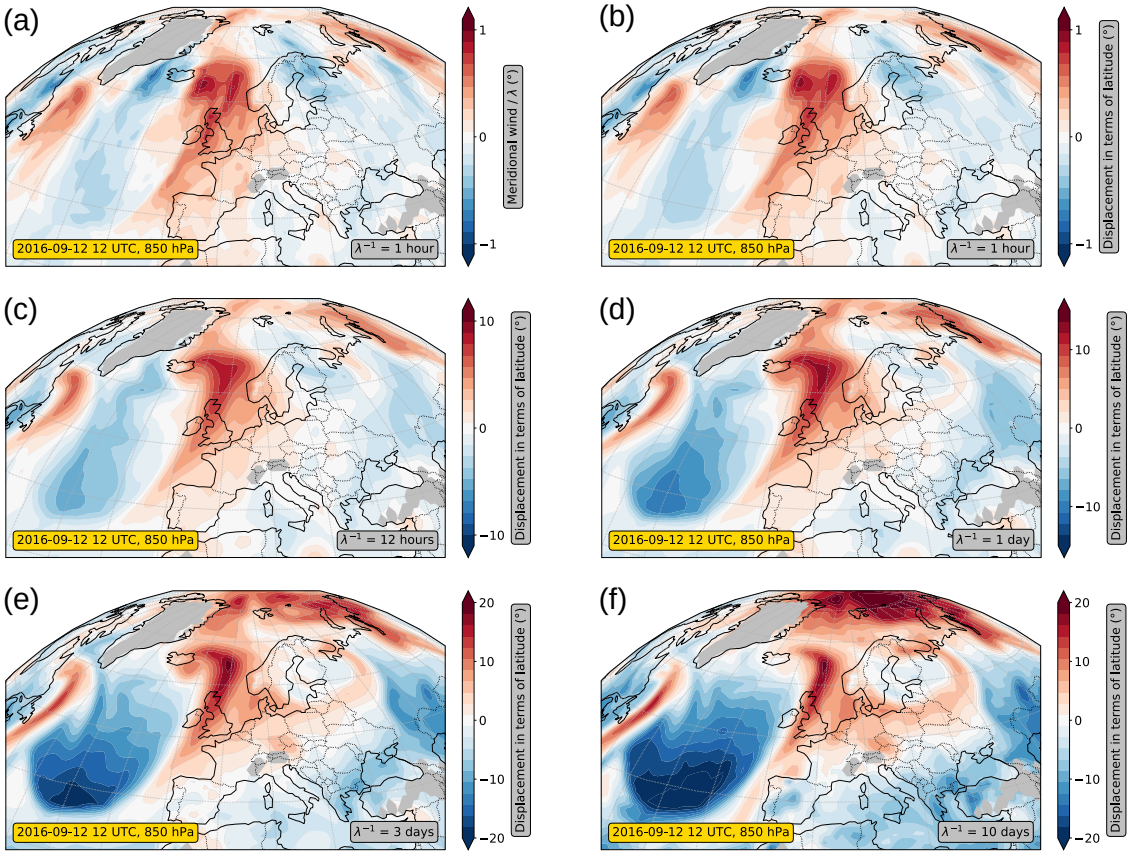

Figure S2.2 – Sensitivity of the tracer method with respect to the relaxation constant λ illustrated in the framework of the example from Figure 2.7. The panels show horizontal cross sections at 850 hPa for 14 September 2016 12 UTC. (a) Meridional wind divided by $\lambda = 1$ hour^{-1}. (b–h) Displacement in terms of pressure for different relaxation constants λ in the range of $\lambda^{-1} = 1$ hour to $\lambda^{-1} = 10$ days.

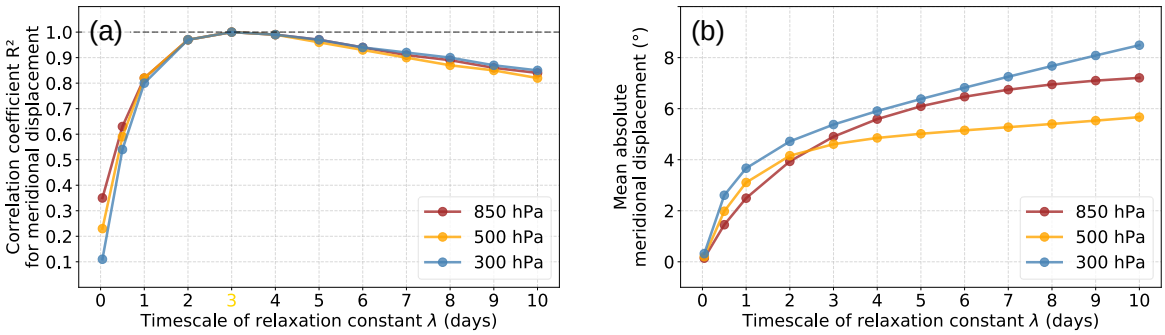

Figure S2.3 – Sensitivity of the meridional displacement with respect to the relaxation constant λ depicted in terms of correlation coefficient and mean absolute displacement. (a) Squared correlation coefficient of the meridional displacement computed with $\lambda^{-1} = 3$ days and the meridional displacement computed with other values for λ. All data points between 30° N and 60° N on the Northern Hemisphere at 00 UTC in September 2016 were considered. The different colours indicate different pressure levels. (b) Mean absolute meridional displacements as a function of λ^{-1}. All data points between 30° N and 60° N on the Northern Hemisphere at 00 UTC in September 2016 were considered. The different colours indicate different pressure levels.

3 Chapter 3

Two Different Perspectives on Heatwaves within the Lagrangian Framework

This chapter has previously been published in:

Mayer, A. and V. Wirth (2025). "Two different perspectives on heatwaves within the Lagrangian framework". *Weather and Climate Dynamics* 6.1, pp. 131–150. DOI: 10.5194/wcd-6-131-2025

Abstract Although heatwaves are one of the most dangerous types of weather-related hazards, their underlying mechanisms are not yet sufficiently understood. In particular, there is still no scientific consensus about the relative importance of the three key processes: horizontal temperature transport, subsidence accompanied by adiabatic heating, and diabatic heating. The current study quantifies these processes using an Eulerian method based on tracer advection, which allows one to extract Lagrangian information. For each grid point at any time, the method yields a decomposition of temperature anomalies into the aforementioned processes, complemented by the contribution of a pre-existing anomaly. Two different approaches for this decomposition are employed. The first approach is based on the full fields of the respective terms and has been established in prior research. In contrast, the second approach is based on the anomaly fields of the respective terms, i.e. deviations from their corresponding climatologies, and is introduced in this study. The two approaches offer two distinct perspectives on the same subject matter. By analysing two recent heatwaves, it is shown that the two decompositions yield substantial differences regarding the relative importance of the processes. A statistical analysis indicates that these differences are not coincidental but are characteristic of the respective regions. We conclude that the Lagrangian characterisation of heatwaves is a matter of perspective.

3.1 Introduction

Heatwaves stand out as one of the most perilous weather-related hazards. They threaten natural ecosystems and society in many ways (e.g. Perkins, 2015; Horton et al., 2016; Barriopedro et al., 2023, and references therein). Their frequency and intensity are projected to increase in the course of global warming (e.g. IPCC, 2021), likely posing an even greater danger to humanity in the future. The socioeconomic importance of heatwaves is thus abundantly clear.

Far less clear, however, are the mechanisms that determine the formation of heatwaves. While it is well known that heatwaves in the extratropics are invariably associated with large-scale upper-tropospheric ridging (Sousa et al., 2018) or anticyclonic flow (e.g. Stefanon et al., 2012; Zschenderlein et al., 2019), often in the form of atmospheric blocking (e.g. Pfahl and Wernli, 2012), a lack of consensus about how exactly air masses with anomalously high temperatures form in this large-scale setting remains.

Three processes are believed to play a role in the context of heatwaves: horizontal advection of warm air (e.g. Screen, 2014; Harpaz et al., 2014; Garfinkel and Harnik, 2017; Sousa et al., 2019; Garfinkel et al., 2024), adiabatic warming in subsiding air (e.g. Bieli et al., 2015; Zschenderlein et al., 2019), and diabatic heating near the surface (e.g. Miralles et al., 2014; Schumacher et al., 2019). The large-scale setting seems to be conducive to all three processes, and often more than one process has been considered important (e.g. Quinting and Reeder, 2017; Hochman et al., 2021; Röthlisberger and Papritz, 2023b). The question still under debate is to what extent each of the individual processes contributes to the formation of heat extremes.

A novel quantitative approach to address this question has recently been proposed by Röthlisberger and Papritz (2023b). This approach sees the decomposition of a temperature anomaly at a given location into (distinct) contributions from each of the three individual processes. More precisely, the approach quantifies the effect of horizontal advection across climatological temperature gradients, the combined effects of vertical advection across climatological temperature gradients and adiabatic warming, and the effect of parcel-based diabatic heating. Like many studies focusing on the processes within heatwaves (Harpaz et al., 2014; Bieli et al., 2015; Zschenderlein et al., 2019; Schielicke and Pfahl, 2022), the temperature anomaly decomposition approach by Röthlisberger and Papritz (2023b) adopts the Lagrangian framework. This is a natural framework for studying the processes under consideration since the laws of dynamics and thermodynamics inherently apply to air parcels. In the Lagrangian framework, individual fluid parcels can be tracked, their physical properties can be identified, and any temporal changes in these properties can be assessed. Therefore, the Lagrangian framework enables a physically meaningful quantification of desired quantities such as adiabatic and (parcel-based) diabatic heating.

Given that most common atmospheric models work in the Eulerian framework, obtaining Lagrangian information about the flow requires some extra effort. Often, backward trajectory models are employed for that purpose (e.g. LAGRANTO, see Sprenger and Wernli 2015; HYSPLIT, see Stein et al. 2015). In this study, however, we refrain from calculating trajectories and instead opt for an alternative approach. We will use the method of tracer advection proposed in Mayer and Wirth (2023) (Chapter 2 of this thesis) to extract the necessary Lagrangian information. The strength of this method is that it provides the required Lagrangian information directly in the form of global gridded fields available at any time step. Most importantly, this makes it quite straightforward to calculate climatologies for every grid point on a global Eulerian grid. We will take advantage of this and, for the first time, present climatologies of the contributions from horizontal transport, vertical transport, and diabatic heating. Based on these climatologies, we will show that the original temperature anomaly decomposition proposed by Röthlisberger and Papritz (2023b) may not be as unique as it appears at first sight. We will thus offer a fresh perspective on the relevance of the individual processes to the formation of heatwaves.

In this paper, we perform a temperature anomaly decomposition (Section 3.2.1), akin to the method proposed by Röthlisberger and Papritz (2023b). To this end, we apply a novel technique to extract the required Lagrangian information (Section 3.2.2). We then use this setup to analyse two recent heatwaves (Section 3.3.1) and to relate the contributions from the individual processes to their long-term averages (Section 3.3.2). Based on these long-term averages, we suggest an alternative decomposition based on anomaly fields (Section 3.3.3). Finally, we complement the two case studies with a short statistical analysis (Section 3.3.4). We close the paper with a brief discussion (Section 3.4) and a concluding summary (Section 3.5).

3.2 Method and data

3.2.1 Lagrangian θ' decomposition

In this study, we aim to quantify the extents to which horizontal transport, vertical transport, and diabatic heating contribute to the formation of temperature anomalies. For this purpose, we examine anomalies in potential temperature θ', which we decompose from a Lagrangian perspective into the aforementioned processes. We opt for potential temperature instead of temperature as our metric because potential temperature is materially conserved in adiabatic flow, rendering it more convenient for theoretical considerations.

We consider the potential temperature anomaly $\theta'(\boldsymbol{x}, t)$ of an air parcel located at grid point $\boldsymbol{x}$ at time t. This anomaly, $\theta'(\boldsymbol{x}, t)$, represents the deviation of the potential temperature $\theta(\boldsymbol{x}, t)$ from its climatological average $\overline{\theta}(\boldsymbol{x}, t)$:

$$\theta'(\boldsymbol{x}, t) = \theta(\boldsymbol{x}, t) - \overline{\theta}(\boldsymbol{x}, t). \tag{3.1}$$

Taking the material derivative D/Dt on both sides

$$\frac{D\theta'}{Dt} = \frac{D\theta}{Dt} - \frac{D\overline{\theta}}{Dt} \tag{3.2}$$

and applying Euler's relation (in pressure coordinates),

$$\frac{D}{Dt} = \frac{\partial}{\partial t} + \boldsymbol{v} \cdot \nabla_{\mathrm{h}} + \omega \frac{\partial}{\partial p} \tag{3.3}$$

to the last term on the right-hand side of Equation (3.2), one obtains

$$\frac{D\theta'}{Dt} = \frac{D\theta}{Dt} - \frac{\partial\overline{\theta}}{\partial t} - \boldsymbol{v} \cdot \nabla_{\mathrm{h}}\overline{\theta} - \omega \frac{\partial\overline{\theta}}{\partial p} \,, \tag{3.4}$$

where $\boldsymbol{v}$ denotes the horizontal wind, ∇_{h} is the horizontal gradient, p is pressure, and ω is the vertical wind in pressure coordinates. Finally, we accumulate the contributions from each of the individual terms in Equation (3.4) along the trajectory of the air parcel and obtain

$$\theta'(x, t) = -\int_{t_0}^{t} \boldsymbol{v} \cdot \nabla_{\mathrm{h}}\overline{\theta}\, dt' - \int_{t_0}^{t} \omega \frac{\partial\overline{\theta}}{\partial p}\, dt' + \int_{t_0}^{t} \frac{D\theta}{Dt'}\, dt' - \int_{t_0}^{t} \frac{\partial\overline{\theta}}{\partial t'}\, dt' + \theta'_0 \,, \tag{3.5}$$

where t_0 is the start time of the integration, t is the time of interest, and θ'_0 is the temperature anomaly at the start time. The integrals in Equation (3.5) represent Lagrangian integrals; i.e. they accumulate information along the trajectory of the air parcel that happens to be located at location $\boldsymbol{x}$ at time t.

Equation (3.5) decomposes a potential temperature anomaly of an air parcel into five contributions: (1) horizontal transport across climatological horizontal temperature gradients; (2) vertical transport across climatological vertical temperature gradients; (3) diabatic heating of the air parcel along its trajectory; (4) local changes in the climatological potential temperature, including seasonality and the diurnal cycle; and (5) the initial temperature anomaly of the air parcel at the start time of the integration. The above decomposition closely follows the approach by Röthlisberger and Papritz (2023b), except that they used temperature instead of potential temperature and chose the initial time t_0 such that the temperature anomaly is zero at that time.

The integrals on the right-hand side of Equation (3.5) can be extended to start at $-\infty$ if, at the same time, the integrand is multiplied by a Heaviside function that jumps from 0 to 1 at time t_0. For reasons that will become clear later, we prefer to use an exponential function instead of a Heaviside function. As shown in the Appendix (Section 3.6), this leads to the following equivalent formulation for $\theta'(\boldsymbol{x}, t)$, namely

$$\begin{aligned}\theta'(\boldsymbol{x},t) = &- \int_{-\infty}^{t} \boldsymbol{v} \cdot \nabla_{\mathrm{h}}\overline{\theta}\ e^{-\lambda(t-t')}\, dt' \\ &- \int_{-\infty}^{t} \omega \frac{\partial\overline{\theta}}{\partial p}\ e^{-\lambda(t-t')}\, dt' \\ &+ \int_{-\infty}^{t} \frac{D\theta}{Dt'}\ e^{-\lambda(t-t')}\, dt' \\ &- \int_{-\infty}^{t} \frac{\partial\overline{\theta}}{\partial t'}\ e^{-\lambda(t-t')}\, dt' \\ &+ R\end{aligned} \tag{3.6}$$

with[2]

$$R = \int_{-\infty}^{t} \left(-\boldsymbol{v} \cdot \nabla_{\mathrm{h}}\overline{\theta} - \omega \frac{\partial\overline{\theta}}{\partial p} + \frac{D\theta}{Dt} - \frac{\partial\overline{\theta}}{\partial t'}\right) \left(1 - e^{-\lambda(t-t')}\right)\, dt' \ .$$

Effectively, the contributions from the different processes in the first four terms of Equation (3.6) are multiplied by a weighting factor $W = \exp[-\lambda(t - t')]$ with $\lambda > 0$; thus, W decreases exponentially as the integration variable t' goes backward in time. The decay time related to the exponential weighting is governed by the parameter λ and effectively determines the timescale of accumulation. It is typically chosen to be on the same order of magnitude as $t - t_0$ in Equation (3.5). On the other hand, the different processes occurring in the residuum term R are multiplied by $1-W$, such that R essentially contains contributions that occurred during the more distant past. The residuum R in Equation (3.6) corresponds to the initial potential temperature anomaly θ'_0 in Equation (3.5), although they are not identical. Like in Equation (3.5), the integrals in the above equation represent the accumulation of processes in air parcels along their trajectories. The only difference is that now the accumulation is more gradually spread over time, such that the contributions fade away more gradually rather than suddenly at time t_0. The decomposition in Equation (3.6),

$$\theta' = \theta_{\mathrm{hor}} + \theta_{\mathrm{ver}} + \theta_{\mathrm{dia}} + \theta_{\mathrm{sea}} + \theta_{\mathrm{pre}} \ , \tag{3.7}$$

is the basis for the analysis in our paper. In the following, we are going to refer to the first three terms as the "process terms", comprising the contributions to the temperature anomaly θ' from (1) horizontal transport θ_{hor}, (2) vertical transport θ_{ver}, and (3) diabatic

[2] *In the expression for R a sign has been corrected.*

heating θ_{dia}. The fourth term, θ_{sea}, containing the seasonality, is much smaller than all other terms and will be neglected in the remainder of this paper. The last term, θ_{pre}, corresponds to the residuum R and will be referred to as the pre-existing potential temperature anomaly in the following. It reflects the accumulation of the three process terms from earlier times along the parcel's trajectory, i.e. up to about λ^{-1} before the point in time considered, t. In other words, θ_{pre} is analogous to the initial potential temperature anomaly θ'_0 of a trajectory of length λ^{-1}.

3.2.2 Eulerian tracer advection with relaxation

The integrals in the θ' decomposition are obtained through the method of tracer advection (Mayer and Wirth, 2023). This method is tailored to provide Lagrangian information that is aggregated over time. The method offers Lagrangian information in the form of gridded fields available at any time step, i.e. throughout the four-dimensional space–time domain. In theory, the same information could be obtained by calculating trajectories. However, gathering Lagrangian information about the full atmospheric volume at many time steps requires the computation of a very large number of trajectories. In contrast, the tracer method eliminates the need for this procedure and directly provides the time-aggregated information required by this study. We feel that this makes the method very convenient for our application. Note that the fields generated by the tracer method cover the entire global domain, but only a small portion of the available data is presented in this study. With the available data, the analysis could be carried out for any other region in the world.

The tracer method is based on the offline advection of passive tracer fields and includes a relaxation term. As a result, one obtains accumulated Lagrangian information at each point of an Eulerian grid at each time step, namely

$$\delta(\boldsymbol{x}, t) = \int_{-\infty}^{t} S(t')\, e^{-\lambda(t-t')}\, dt' \,, \tag{3.8}$$

where $S(t')$ is some source term, and λ is the relaxation constant. Note that the term on the right-hand side represents a Lagrangian integral and features the same exponential weighting as in our decomposition (3.6). That is, indeed, the primary reason why we introduced the exponential weighting earlier in our θ' decomposition approach. To obtain values for $\delta(\boldsymbol{x}, t)$, the tracer method numerically solves the partial differential equation

$$\frac{\partial \delta}{\partial t} = -\boldsymbol{u} \cdot \nabla \delta - \lambda \delta + S \tag{3.9}$$

with initial condition

$$\delta(\boldsymbol{x}, t_{\mathrm{init}}) = 0 \,. \tag{3.10}$$

In this equation, δ is a three-dimensional (tracer) field that is advected by the three-dimensional wind $\boldsymbol{u}$ and that is, in addition, subject to some source term S. The exponential weighting present in Equation (3.8) stems from the linear relaxation term $-\lambda\,\delta$ included on the right-hand side of Equation (3.9). The primary advantage of the relaxation is that it gradually diminishes the influence of past data on the fly, enabling us to obtain time-continuous Lagrangian information much more efficiently than without relaxation.

When S can be expressed as the material rate of change in some quantity a, i.e. $S = Da/Dt$, Equation (3.9) can be reformulated into

$$\frac{\partial \psi}{\partial t} = -\boldsymbol{u} \cdot \nabla \psi - \lambda(\psi - a) \quad , \quad \psi(\boldsymbol{x}, t_{\text{init}}) = a(\boldsymbol{x}, t_{\text{init}}) \tag{3.11}$$

in combination with

$$\delta = a - \psi. \tag{3.12}$$

Instead of δ itself, the field ψ now constitutes the tracer field, and the source term S is implicitly included in the relaxation term.

A separate tracer is required for each term in the θ' decomposition. To compute θ_{hor}, θ_{ver}, and θ_{sea}, we use Equation (3.9), with the source term S as $-\boldsymbol{v} \cdot \nabla_{\text{h}} \overline{\theta}$, $-\omega \, \frac{\partial \overline{\theta}}{\partial p}$, and $\frac{\partial \overline{\theta}}{\partial t'}$, respectively. For example, in order to compute θ_{hor}, we numerically integrate the following equation:

$$\frac{\partial \delta}{\partial t} = -\boldsymbol{u} \cdot \nabla \delta - \lambda \delta - \boldsymbol{v} \cdot \nabla_{\text{h}} \overline{\theta} \quad , \quad \delta(\boldsymbol{x}, t_{\text{init}}) = 0 \; . \tag{3.13}$$

The resulting solution is then equivalent to

$$\delta(\boldsymbol{x}, t) = \int_{-\infty}^{t} -\boldsymbol{v}(t') \cdot \nabla_{\text{h}} \overline{\theta}(t') \, e^{-\lambda(t-t')} \, dt' \; . \tag{3.14}$$

In contrast, θ_{dia} is computed via Equations (3.11) and (3.12). That is, we set a to $\theta(\boldsymbol{x}, t)$ and numerically integrate the following equation:

$$\frac{\partial \psi}{\partial t} = -\boldsymbol{u} \cdot \nabla \psi - \lambda(\psi - \theta) \quad , \quad \psi(\boldsymbol{x}, t_{\text{init}}) = \theta(\boldsymbol{x}, t_{\text{init}}) \tag{3.15}$$

in combination with

$$\delta = \theta - \psi \; . \tag{3.16}$$

The solution is equivalent to the desired integral,

$$\delta(\boldsymbol{x}, t) = \int_{-\infty}^{t} \frac{D\theta}{Dt} \, e^{-\lambda(t-t')} \, dt' \; . \tag{3.17}$$

Using Equations (3.11) and (3.12) instead of Equation (3.9) for the computation of θ_{dia} has the significant advantage of not requiring any information about the parcel-based diabatic heating rate, which is often unavailable or not fully available.

Finally, θ_{pre} is computed as the residuum from the actual potential temperature anomaly θ' and the other four terms:

$$\theta_{\mathrm{pre}} = \theta' - \theta_{\mathrm{hor}} - \theta_{\mathrm{ver}} - \theta_{\mathrm{dia}} - \theta_{\mathrm{sea}} \ . \tag{3.18}$$

For details about the tracer method and its implementation, the interested reader is referred to Mayer and Wirth (2023).

3.2.3 Data

This study is based on ERA5 reanalysis data (Hersbach et al., 2020) for the period of 2010 to 2022. We use global data on model levels (Hersbach et al., 2017), with a horizontal resolution of 1° and a temporal resolution of 3 hours. In the vertical dimension, we take every second model level between model levels 136 and 50, which cover the entire troposphere and parts of the lower stratosphere. Whenever we show or refer to data on pressure levels, we provide data that have been linearly interpolated from model levels to a set of pressure levels. For the relaxation constant, we use $\lambda^{-1} = 7$ days throughout this study.

The variables used are the zonal wind u, the meridional wind v, the vertical velocity $\dot{\eta}$ that corresponds to the vertical coordinate η, the pressure–coordinate vertical velocity ω, and pressure p. Potential temperature θ is computed from p and temperature T as

$$\theta = \left(\frac{p_0}{p}\right)^{\kappa} T \tag{3.19}$$

with $\kappa = R/c_{\mathrm{p}} = 0.285$ and $p_0 = 1013.25$ hPa. The climatological average $\bar{\theta}$ in Equation (3.6) depends on both the time of the year and the time of the day. It is obtained for each day of the year by computing a time-of-day-specific temporal average over the 13 years considered, followed by a 31 days smoothing; effectively, each climatological value is an average over $13 \times 31 = 403$ individual values. Note that the period and the procedure chosen to compute the temperature climatology are similar to those used in the study by Hotz et al. (2024), with which we compare our results later on.

The θ' decomposition is obtained every 3 hours and aggregated to yield daily means. Whenever we use the term “near-surface”, we refer to the average over the lowest 50 hPa above the surface.

3.3 Results

3.3.1 A first look at two recent heatwaves

In the following, we are going to present the results of our decomposition for two recent heat events, namely the Pacific Northwest heatwave in 2021 and the UK heatwave in 2022. In particular, we discuss the evolution of the near-surface θ' as well as the time-mean vertical θ' structure. In doing so, we follow the analysis of Hotz et al. (2024), who applied the temperature decomposition of Röthlisberger and Papritz (2023b) to the aforementioned heatwaves. In particular, we use the same definition of the heatwave regions (49–59° N, 125–115° W for the Pacific Northwest heatwave; 49–59° N, 6° W–4° E for the UK heatwave) and episodes (27 June to 1 July 2021 for the Pacific Northwest heatwave; 16 to 20 July 2022 for the UK heatwave) to enable a straightforward comparison between their results and ours.

3.3.1.1 The Pacific Northwest heatwave

In 2021, a severe heatwave struck the Pacific Northwest, marking unprecedented temperatures in Canada and the USA. Many cities experienced all-time maximum-temperature records being broken by several degrees (e.g. Philip et al., 2022; White et al., 2023). The heatwave was associated with a strong upper-tropospheric quasi-stationary anticyclone (e.g. Philip et al., 2022; Neal et al., 2022) fuelled by warm-conveyor-belt outflow from an upstream cyclone (e.g. Schumacher et al., 2022; Neal et al., 2022; White et al., 2023; Oertel et al., 2023; Röthlisberger and Papritz, 2023b; Papritz and Röthlisberger, 2023; Hotz et al., 2024). For this event, we will now showcase the results of our decomposition.

To start with, Figure 3.1 illustrates the evolution of the heatwave by showing θ' and its decomposition for 3 individual days during the heatwave. As already noted by previous authors (e.g. Neal et al., 2022; Hotz et al., 2024), the large temperature anomalies first appeared in the upper troposphere and only later emerged near the surface. Initially, a tongue of warm air intruded northward at upper levels (Figure 3.1a; see Neal et al. 2022), and this can be associated with significant positive contributions from horizontal transport and diabatic heating (Figure 3.1b,d), as well as a negative contribution from vertical transport (Figure 3.1c). Such contributions would be expected in the context of warm-conveyor-belt outflow. Later, the air mass associated with the tongue started to form a spiral and became enclosed in the anticyclone (Figure 3.1h,i). During the course of the event, the contribution from the pre-existing anomaly seemed to grow steadily (Figure 3.1e,j,o), which first occurred mostly in the upper troposphere and later also near the surface. At the same time, the contributions from horizontal transport, vertical transport, and diabatic heating decreased in the upper troposphere. This behaviour

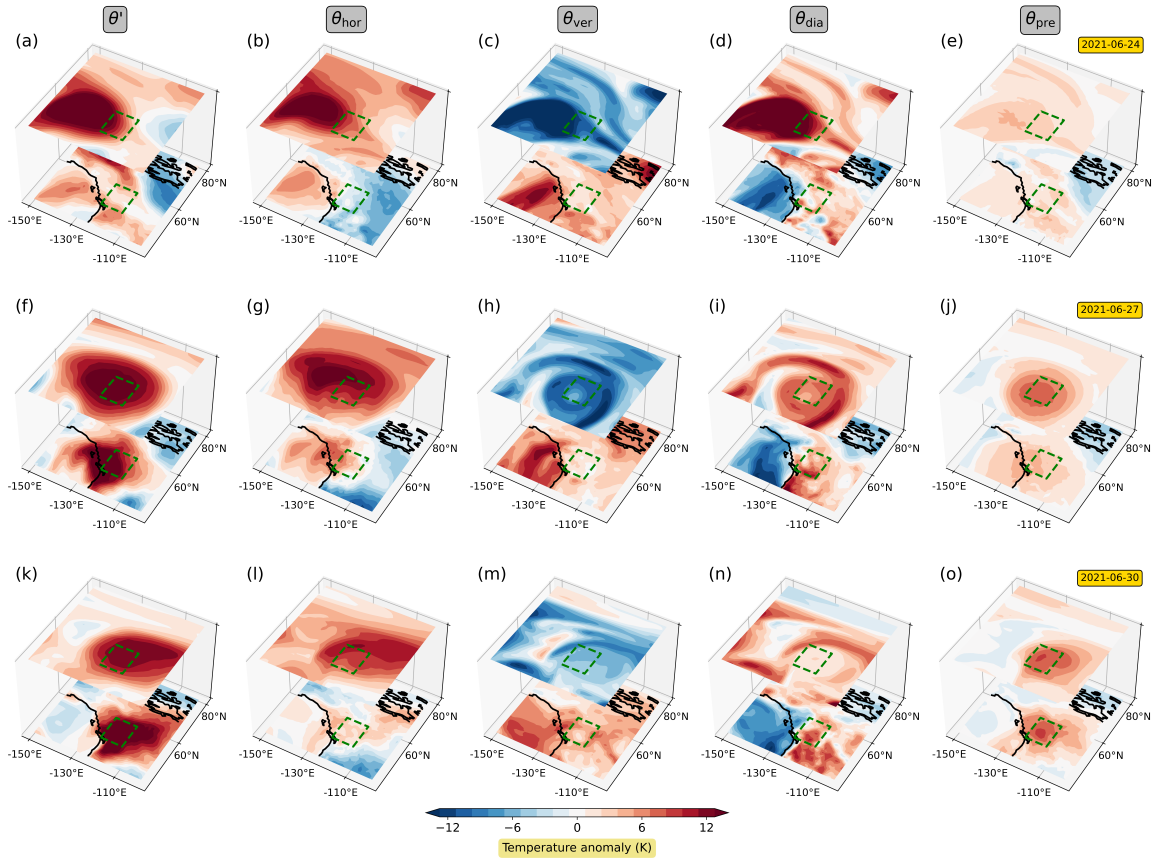

Figure 3.1 – Illustration of the three-dimensional structure of θ' and its contributions from horizontal transport, vertical transport, diabatic heating, and the pre-existing anomaly for three selected dates (24, 27, and 30 June 2021). The upper layer depicts fields averaged between 300 and 400 hPa, and the lower layer depicts fields near the surface. The green rectangle indicates the Pacific Northwest heatwave region.

suggests an effective transfer of heat from the three process terms to the pre-existing term: what was initially classified as horizontal transport, vertical transport, or diabatic heating gradually turned into the pre-existing term. This sequence likely indicates that the large temperature anomalies present at the later stage were generated at least partly before or during the early stage of the heatwave. This interpretation is consistent with the findings by, e.g. Papritz and Röthlisberger (2023), who identify warm-conveyor-belt air streams associated with two upstream cyclones as the main heat source for this event.

We next investigate the evolution of the near-surface θ' over the course of the heatwave. To this end, we show time series of the individual θ' terms near the surface, averaged over the core heatwave region (green box in Figure 3.1). Figure 3.2 reveals that during the heat event, all four decomposition terms contributed positively to θ', albeit with varying magnitudes. Throughout most of the event, the largest positive contribution from the three process terms was given by diabatic heating. The contribution from horizontal transport reached its maximum during the early phase and decreased throughout the

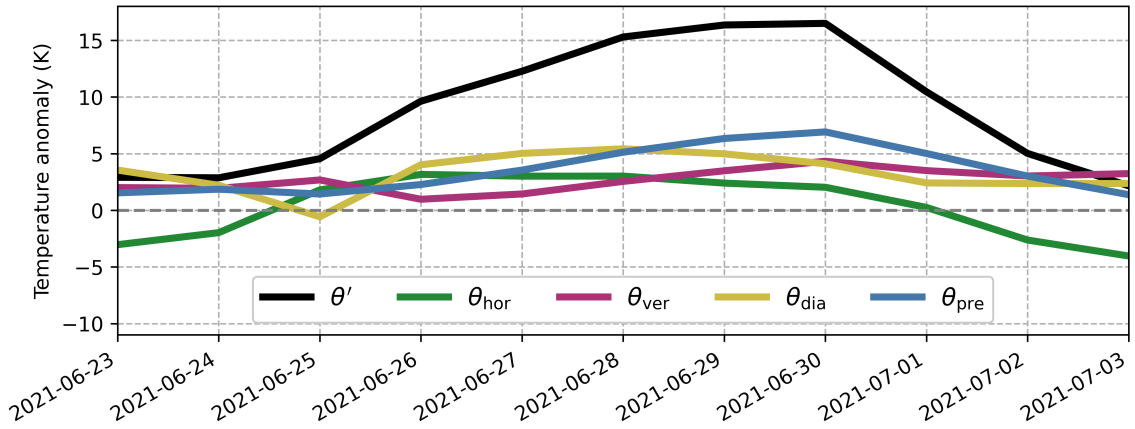

Figure 3.2 – Evolution of the near-surface potential temperature anomaly θ' and its decomposition into contributions from horizontal transport, vertical transport, diabatic heating, and the pre-existing anomaly during the Pacific Northwest heatwave. The time series have been obtained by averaging the different terms over the lowest 50 hPa above the surface within the Pacific Northwest heatwave region (49–59° N, 125–115° W).

course of the event, while the contribution from vertical transport was initially small and gradually increased as the heatwave progressed. Similarly, the pre-existing anomaly was initially small and grew steadily over the course of the event, until it finally made the largest contribution out of all the terms during the late stage of the heatwave. Overall, the evolution is similar to that shown by Hotz et al. (2024) (their Figures 3i and 4). For example, there is agreement that the near-surface diabatic heating makes the largest contribution of the three process terms throughout the course of the heatwave, even if it is somewhat larger in Hotz et al. (2024) than here. Likewise, in both analyses, the contributions from horizontal and vertical transport swap rankings on 28 June in terms of their positive contribution to θ'.

Finally, we present the time-mean vertical θ' structure during the heatwave in Figure 3.3. In essence, these plots show the same characteristics as discussed before, with the benefit of the full vertical resolution, but in a time-aggregated manner. The general structure of the time-mean vertical fields is, again, similar to the results in Hotz et al. (2024), even though there are differences in the exact values and some structural details. To be clear, we do not expect perfect agreement for two basic reasons: (1) we use potential temperature rather than temperature as our key variable, and (2) our decomposition includes the pre-existing anomaly, which does not exist in the formulation of Röthlisberger and Papritz (2023b) due to their specific choice of t_0. Item (1) can be expected to be an issue mostly in the upper troposphere where T and θ deviate substantially; in contrast, item (2) can generally be an issue throughout the atmosphere. During the episode considered, our term R in Figure 3.3e maximises in the middle troposphere. Note that this behaviour

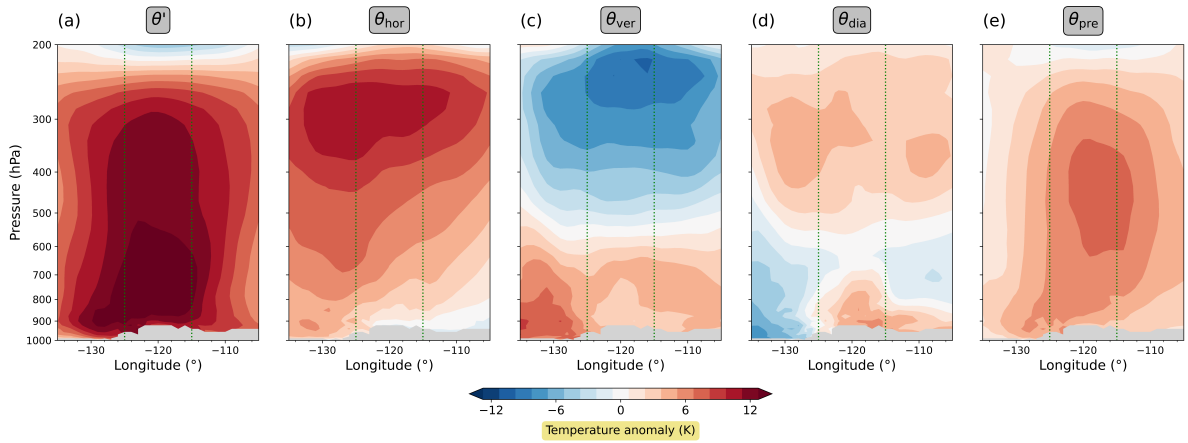

Figure 3.3 – The 5 day mean (27 June–1 July 2021) vertical cross-section showing the θ' decomposition during the Pacific Northwest heatwave. Fields are latitudinally averaged between 49 and 59° N. The panels show (a) the potential temperature anomaly θ', (b) the contribution from horizontal transport, (c) the contribution from vertical transport, (d) the contribution from diabatic heating, and (e) the contribution from the pre-existing anomaly. The topography is shown in grey. The two vertical green lines in each panel indicate the longitudinal extent of the Pacific Northwest heatwave region.

largely resembles the structure of the Lagrangian age shown by Hotz et al. (2024) (their Figure 4b), consistent with our interpretation of R as the pre-existing anomaly.

Overall, our results for the Pacific Northwest heatwave are in good agreement with those of Hotz et al. (2024), suggesting that both methods are able to quantitatively capture the key processes of temperature anomaly formation and their relative importance.

3.3.1.2 The UK heatwave

We now turn to analysing the UK heatwave in 2022. In comparison to the temperature anomalies reached during the Pacific Northwest heatwave, the UK heatwave was less severe. Nonetheless, it was sufficiently strong to break several all-time maximum-temperature records in multiple cities across the UK.

Again, we first illustrate the evolution of the heatwave by showing θ' and its decomposition for 3 individual days (Figure 3.4). Like the Pacific Northwest heatwave, the UK heatwave was also associated with anticyclonic flow, albeit with a much more transient character. High-temperature anomalies first occurred in the southwestern parts of Europe, then intensified and crossed the UK before shifting downstream (Figure 3.4a,f,k). As with the Pacific Northwest heatwave, a tongue of warm air initially appeared in the upper troposphere, accompanied by a significant positive contribution from horizontal transport (Figure 3.4b), and some positive contribution from diabatic heating (Figure 3.4d) as well as negative contribution from vertical transport (Figure 3.4c). Presumably, this is again a

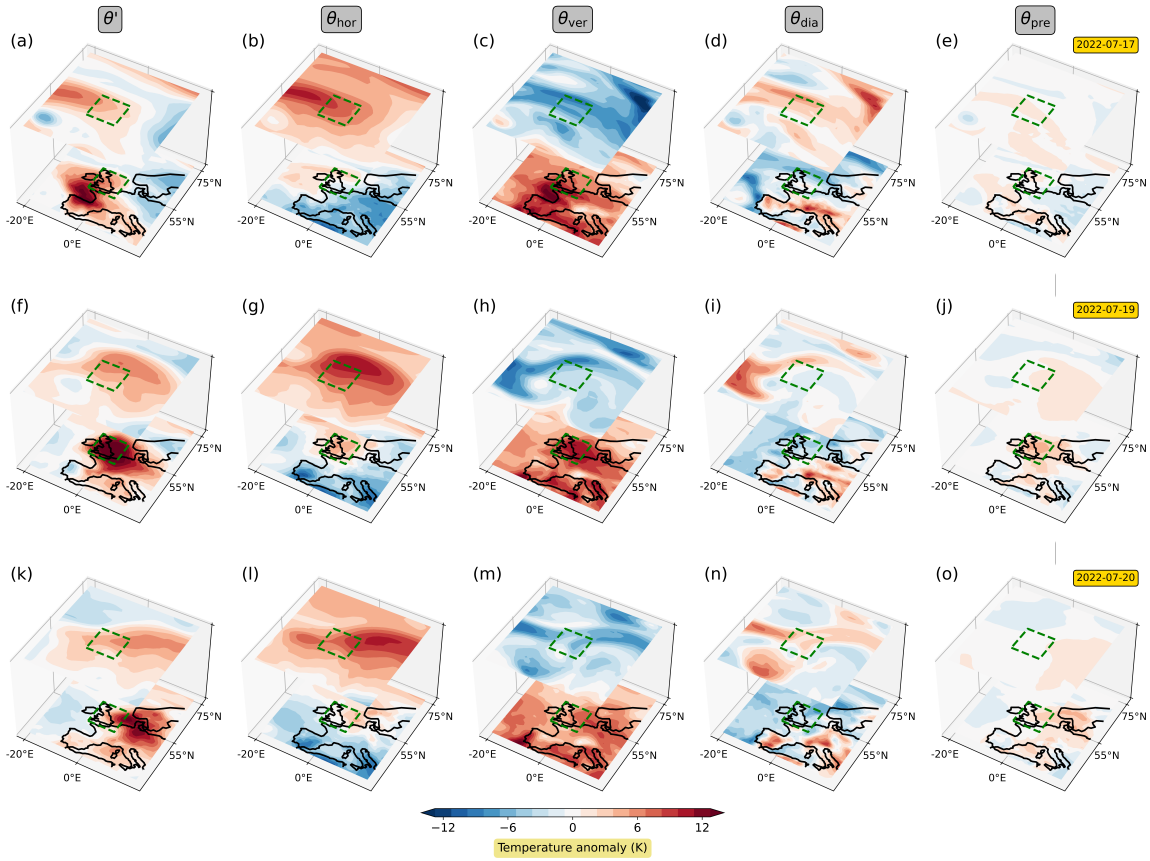

Figure 3.4 – Illustration of the three-dimensional structure of θ' and its contributions from horizontal transport, vertical transport, diabatic heating, and the pre-existing anomaly for three selected dates (17, 19, and 20 July 2022). The upper layer depicts fields averaged between 300 and 400 hPa, and the lower layer depicts fields near the surface. The green rectangle indicates the UK heatwave region.

signature of warm-conveyor-belt outflow, although the features are overall less coherent than in the Pacific Northwest case. Later, the tongue stretched around the core heatwave region, but unlike the Pacific Northwest heatwave, it did not develop a spiralling pattern.

The evolution of the near-surface θ' decomposition (Figure 3.5) reveals that the positive contribution from vertical transport was the highest throughout the event, jointly followed by the contributions from horizontal transport and the pre-existing anomaly. The contribution from diabatic heating, on the other hand, was negative. This is a noticeable difference from the Pacific Northwest heatwave. Our results align quite well with those found by Hotz et al. (2024): they also attribute the largest positive contribution to vertical transport, and in both cases, the diabatic heating did not make any substantial positive contribution. One noticeable difference is the contribution from vertical transport before and after the heatwave, which in our analysis is considerably larger.

We finally look at the time-mean vertical structure of the event's θ' decomposition (Figure 3.6). Once again, we find small quantitative differences between our analysis

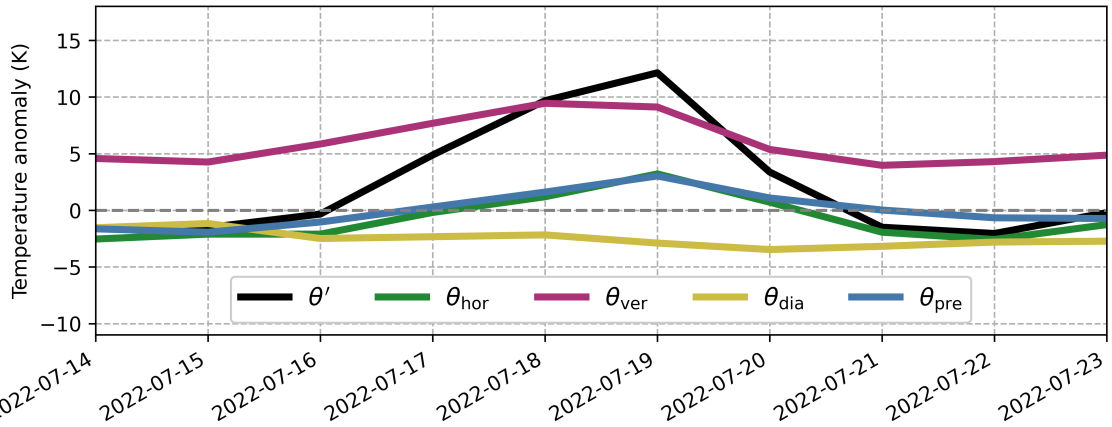

Figure 3.5 – Evolution of the potential temperature anomaly θ' and its decomposition into contributions from horizontal transport, vertical transport, diabatic heating, and the pre-existing anomaly during the UK heatwave. The time series have been obtained by averaging the different terms over the lowest 50 hPa above the surface within the UK heatwave region (6° W–4° E, 49–59° N).

and the analysis of Hotz et al. (2024), while the overall patterns of the fields are similar in both analyses. Again, for the reasons mentioned earlier, we do not expect perfect agreement between these two analyses. All in all, both analyses lead to essentially the same conclusions, and this suggests that the exact design of the temperature anomaly decomposition and its implementation is of minor importance.

3.3.2 Long-term averages of the terms in the decomposition

We now present long-term averages of the θ' decomposition for the two regions discussed above. Subsequently, this will allow us to adopt a novel perspective on the relevance of the different terms in the decomposition. We believe that this is an important step because, as we will see shortly, many of the features of the individual terms described above are part of the climatological behaviour and, therefore, may not be helpful in explaining an anomalous temperature.

The long-term averages of the terms in the θ' decomposition are determined by calculating temporal averages for each individual day of the year, based on the period of 2010 to 2022. Subsequently, these day-specific temporal averages are smoothed using a 31 day running average. Note that this procedure is identical to the one used for the temperature climatology (see Section 3.2.3). The period to compute the long-term averages comprises (only) 13 years, which is admittedly shorter than the traditional definition of a climatological mean. However, we deliberately chose this relatively short period of time to ensure that the climatological mean calculated mostly reflects the current state of the changing climate. This way, the anomalies we present are considered anomalous compared

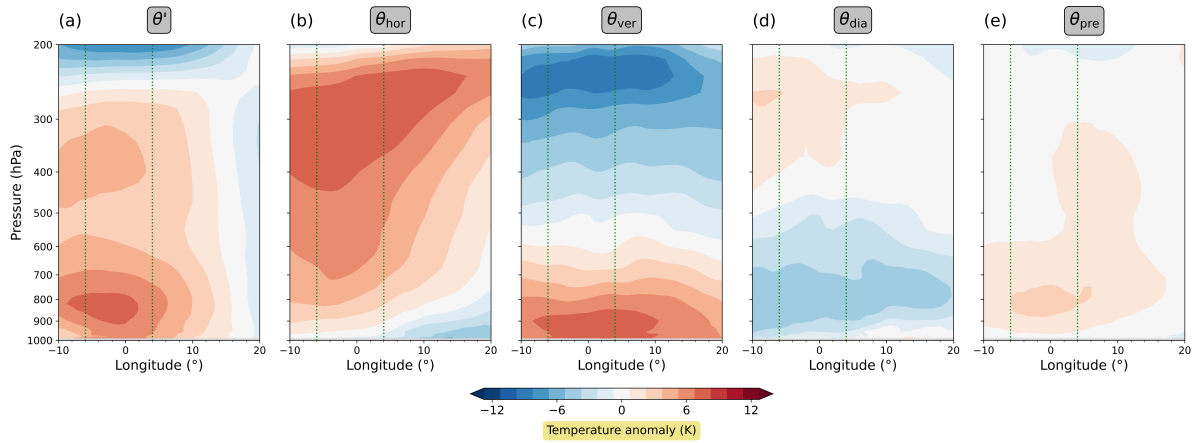

Figure 3.6 – The 5 day mean (16–20 July 2022) vertical cross-sections showing the θ' decomposition during the UK heatwave. Fields are latitudinally averaged between 49 and 59° N. The panels show (a) the potential temperature anomaly θ', (b) the contribution from horizontal transport, (c) the contribution from vertical transport, (d) the contribution from diabatic heating, and (e) the contribution from the pre-existing anomaly. The two vertical green lines in each panel indicate the longitudinal extent of the UK heatwave region.

to today's conditions rather than to those from the past. In the end, the chosen length of the period was a compromise between the robustness of the statistics and the stationarity of the climate.

We start with the long-term averages in the Pacific Northwest region (Figure 3.7[3]). Here, the contribution from horizontal transport (Figure 3.7a,e) is positive in the upper troposphere and mostly negative close to the surface. This behaviour aligns well with the characteristics of the zonal-mean Lagrangian circulation (e.g. Townsend and Johnson, 1985; Iwasaki, 1989; Juckes, 2001), which exhibits poleward motion in the upper troposphere (implying a positive contribution from horizontal transport) and equatorward motion near the surface (implying a negative contribution from horizontal transport). Deviations from this overall behaviour are most likely due to local land–sea contrasts in temperature. The long-term average of the contribution from vertical transport (Figure 3.7b,f) exhibits behaviour opposite to that of the horizontal transport, namely a negative contribution in the upper troposphere and a positive contribution near the surface. From a statistical point of view, this makes perfect sense, as air masses close to the surface can only originate from higher above (implying a positive contribution from vertical transport); just below the tropopause, the situation is more or less opposite, to the extent that the tropopause is a barrier to vertical transport. The contribution from diabatic heating (Figure 3.7c,g) is positive in the upper troposphere, possibly due to latent-heat release within frequently occurring warm conveyor belts within the north Pacific storm track region. Near the

[3] *A bar has been added to the variables in the legend in panel (i).*

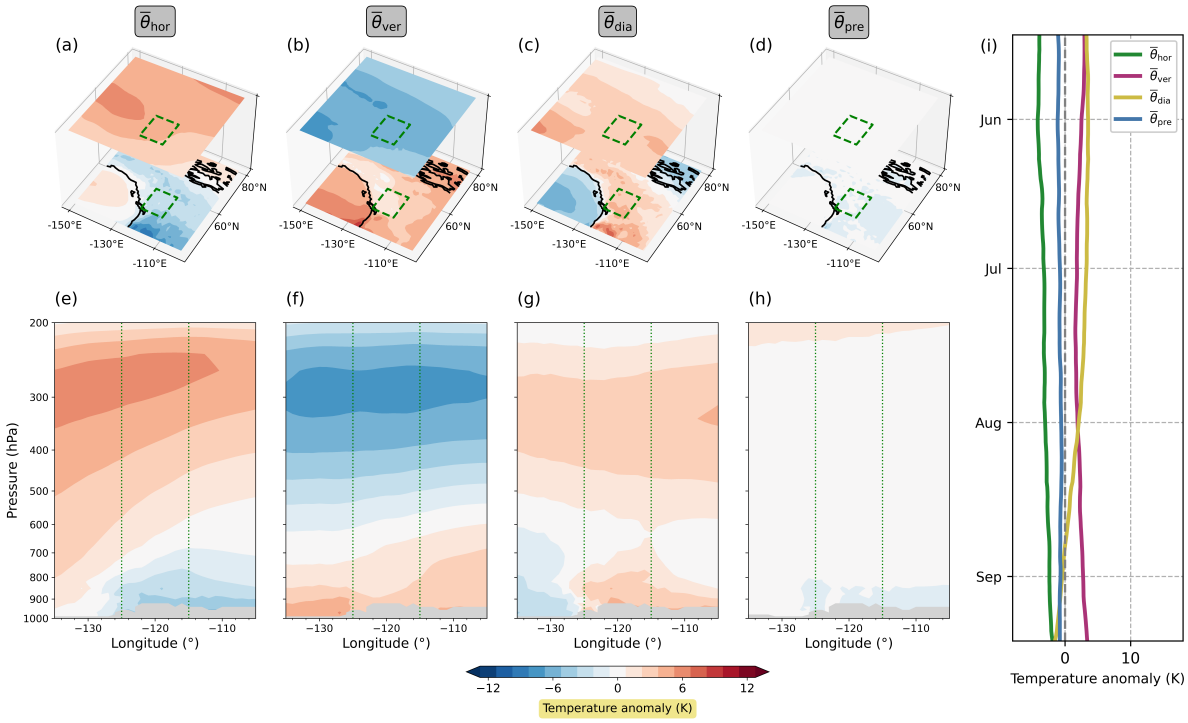

Figure 3.7 – The long-term average (2010–2022) of the θ' decomposition for the Pacific Northwest. Panels (a) to (h) depict the long-term averages for the time period during which the Pacific Northwest heatwave happened; i.e. they show the 5 day averages of the daily climatologies from 27 June to 1 July. Panel (i) shows the evolution of the long-term average near-surface θ' decomposition during the summer season, averaged over the Pacific Northwest heatwave region. The three-dimensional plots in panels (a)–(d) are analogous to those in Figure 3.2b–p, and the vertical cross-sections in panels (e)–(h) are analogous to those in Figure 3.3b–e.

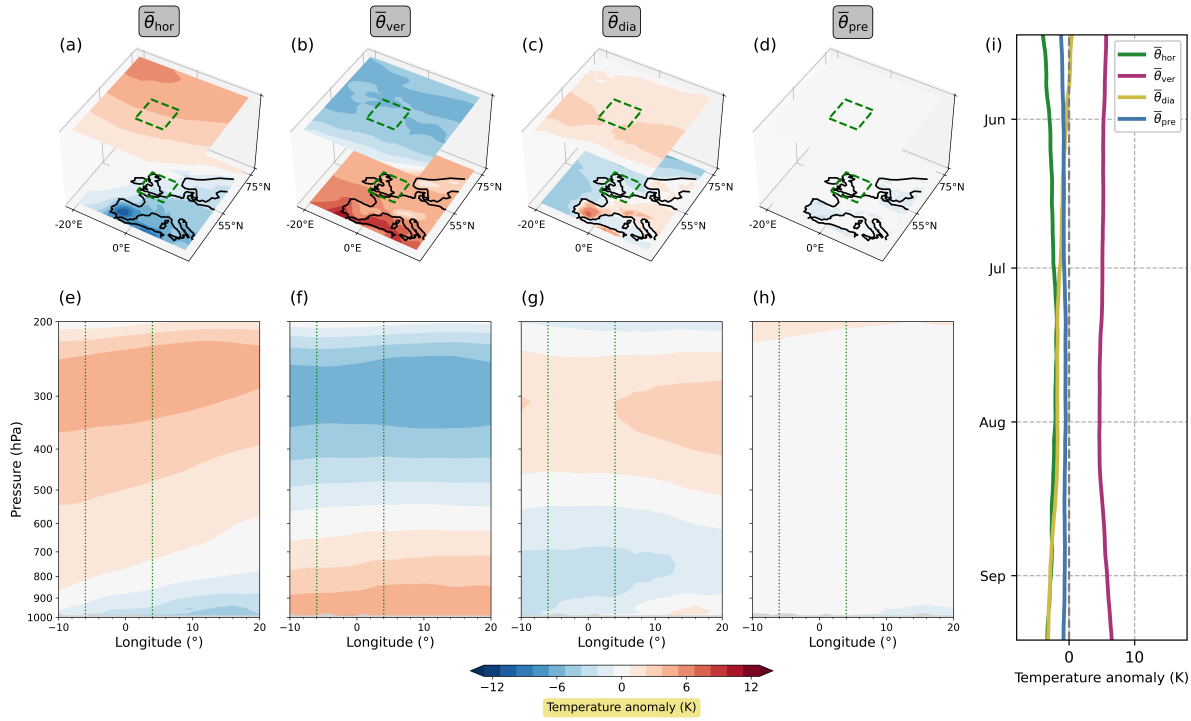

Figure 3.8 – The long-term average (2010–2022) of the θ' decomposition for the UK region. Panels (a) to (h) depict the long-term averages for the time period during which the UK heatwave happened; i.e. they show the 5 day averages of the daily climatologies from 16 to 20 July. Panel (i) shows the evolution of the long-term average near-surface θ' decomposition during the summer season, averaged over the UK heatwave region. The three-dimensional plots in panels (a)–(d) are analogous to those in Figure 3.5b–p, and the vertical cross-sections in panels (e)–(h) are analogous to those in Figure 3.6b–e.

surface, the contribution from diabatic heating is positive over the land and negative over the ocean, which is most likely related to the influence of surface heat fluxes. The contribution from the pre-existing anomaly (Figure 3.7d,h) is small throughout the whole troposphere. All terms show little variation over the summer season (Figure 3.7i), except for the diabatic one. The latter exhibits a range of about 5 K, with positive values until mid-August and negative values thereafter. Arguably, this behaviour reflects the seasonal cycle in solar radiation.

The long-term averages from the UK region (Figure 3.8[4]) exhibit mostly the same characteristics as those from the Pacific Northwest. The only notable difference manifests near the surface. Here, the contribution from diabatic heating is significantly lower in the UK region compared to the Pacific Northwest, ranging from near zero to even slightly negative values. Presumably, this feature can be attributed to the fact that the UK is surrounded by the ocean, which implies that air masses located over the UK have a larger chance of originating over the ocean and, therefore, are less exposed to sensible heat fluxes over land.

3.3.3 A second look at the two heatwaves from an anomaly-based perspective

We now continue with the analysis of whether and to what extent the terms in the decomposition were anomalous with respect to their corresponding climatologies. To this end, we compute the anomaly fields of the individual decomposition terms and use these in our alternative decomposition. More specifically, we define the anomaly field of a variable ψ as the deviation ψ' from its long-term average $\overline{\psi}$, i.e.

$$\psi' = \psi - \overline{\psi} \, . \tag{3.20}$$

Using this definition, the original θ' decomposition (3.7) can be expressed as

$$\theta' = (\overline{\theta}_{\mathrm{hor}} + \theta'_{\mathrm{hor}}) + (\overline{\theta}_{\mathrm{ver}} + \theta'_{\mathrm{ver}}) + (\overline{\theta}_{\mathrm{dia}} + \theta'_{\mathrm{dia}}) + (\overline{\theta}_{\mathrm{sea}} + \theta'_{\mathrm{sea}}) + (\overline{\theta}_{\mathrm{pre}} + \theta'_{\mathrm{pre}}) \, , \tag{3.21}$$

where each term is now represented as the sum of its climatological mean and a deviation from this mean. Taking the time average on both sides turns Equation (3.21) into

$$\overline{\theta'} = \overline{(\overline{\theta}_{\mathrm{hor}} + \theta'_{\mathrm{hor}})} + \overline{(\overline{\theta}_{\mathrm{ver}} + \theta'_{\mathrm{ver}})} + \overline{(\overline{\theta}_{\mathrm{dia}} + \theta'_{\mathrm{dia}})} + \overline{(\overline{\theta}_{\mathrm{sea}} + \theta'_{\mathrm{sea}})} + \overline{(\overline{\theta}_{\mathrm{pre}} + \theta'_{\mathrm{pre}})} \, . \tag{3.22}$$

[4] *A bar has been added to the variables in the legend in panel (i).*

Given that the time-averaging scheme is linear, this equation can be rewritten as [5]

$$\overline{\theta'} = (\overline{\overline{\theta}}_{\text{hor}} + \overline{\theta'}_{\text{hor}}) + (\overline{\overline{\theta}}_{\text{ver}} + \overline{\theta'}_{\text{ver}}) + (\overline{\overline{\theta}}_{\text{dia}} + \overline{\theta'}_{\text{dia}}) + (\overline{\overline{\theta}}_{\text{sea}} + \overline{\theta'}_{\text{sea}}) + (\overline{\overline{\theta}}_{\text{pre}} + \overline{\theta'}_{\text{pre}}) \; . \quad (3.23)$$

Assuming further that the time-averaging scheme obeys the rules of Reynolds averaging, i.e.

$$\overline{\psi'} = 0 \;\; ; \;\; \overline{\overline{\psi}} = \overline{\psi} \quad (3.24)$$

Equation (3.23) can be simplified to

$$0 = \overline{\theta}_{\text{hor}} + \overline{\theta}_{\text{ver}} + \overline{\theta}_{\text{dia}} + \overline{\theta}_{\text{sea}} + \overline{\theta}_{\text{pre}} \; . \quad (3.25)$$

Substituting Equation (3.25) into Equation (3.21) yields the following new θ' decomposition:

$$\theta' = \theta'_{\text{hor}} + \theta'_{\text{ver}} + \theta'_{\text{dia}} + \theta'_{\text{sea}} + \theta'_{\text{pre}} \; . \quad (3.26)$$

In contrast to the original θ' decomposition (3.7), which relies on full (absolute) fields, the new θ' decomposition (3.26) is based on anomaly fields. Both formulations are mathematically sound; they differ in that they offer two distinct perspectives on the same subject matter. Note that our daily climatologies imply some 31 days smoothing, such that the assumption of a Reynolds average is, strictly speaking, not satisfied. However, as we will see below, the corresponding error is negligible.

In the following, we will show that the anomaly-based perspective on the θ' decomposition leads to substantial differences regarding the relative importance of horizontal transport, vertical transport, and diabatic heating compared to the perspective in terms of the full fields.

3.3.3.1 The Pacific Northwest heatwave revisited

Once again, we begin by discussing the Pacific Northwest heatwave and first look at time-mean vertical cross-sections from the anomaly-based perspective (Figure 3.9). In the upper troposphere, the contributions from horizontal transport, vertical transport, and diabatic heating are substantially smaller in magnitude than their contributions in terms of the full fields. As a consequence, only the horizontal transport, together with the pre-existing anomaly, still yields a substantial positive contribution to θ'. In the lower troposphere, positive contributions from vertical transport and diabatic heating persist, albeit smaller in magnitude. In contrast, the contribution from horizontal transport changes in such a way that it now provides positive contributions throughout the entire

[5] *Equation (3.23) has been corrected.*

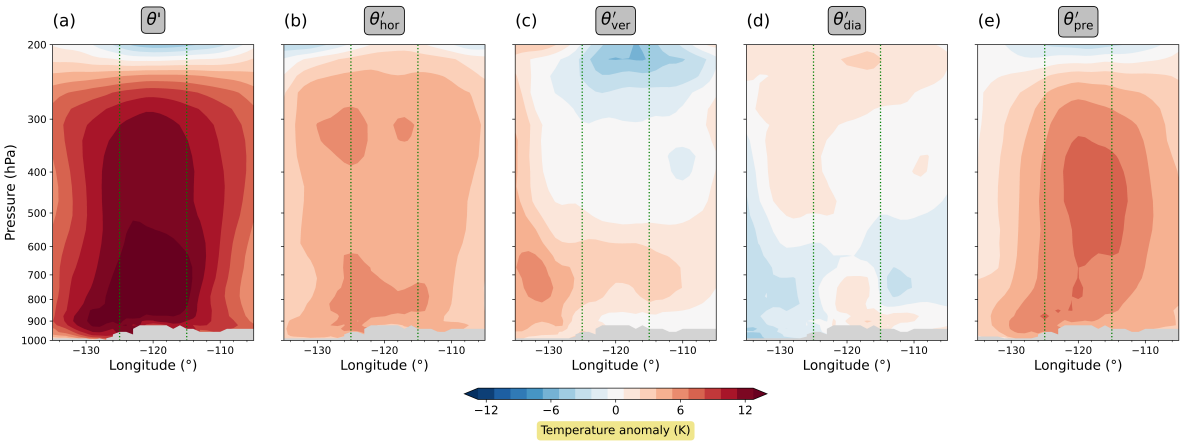

Figure 3.9 – Same as Figure 3.3, but the θ' decomposition terms are now depicted as deviations from their long-term averages.

lower troposphere, constituting the largest contribution to θ' alongside the pre-existing anomaly.

Second, we show the evolution of the near-surface θ' decomposition from the anomaly-based perspective (Figure 3.10). Like before, all terms yield mostly positive contributions, but the magnitudes differ. Most notably, the diabatic heating no longer dominates among the three process terms; instead, its contribution is significantly smaller than that of horizontal transport throughout the episode. As before, the contribution from vertical transport increases throughout the evolution of the heatwave but no longer overtakes the contribution from horizontal transport at any point in time. Only the pre-existing term manages to overtake the contribution from horizontal transport at some point, albeit 2 days later than before. Note that the slopes of the individual curves are nearly identical in both decompositions because the time rate of change in the corresponding climatology terms is very small (see Figure 3.7i). This means that both decompositions yield almost the same results if one aims to diagnose the rate of change in the individual terms. However, in the current paper, we focus on the temperature anomalies themselves rather than their tendencies.

The change from the original to the anomaly-based perspective swaps the roles, broadly speaking, of the diabatic heating and the horizontal transport regarding their contributions to the temperature anomaly θ'. The new perspective takes into account that normally the contribution from horizontal transport is negative, such that a slight positive contribution to the original decomposition actually represents a rather strong positive contribution to the anomaly-based decomposition. In contrast, the diabatic heating, which makes a strong contribution to the original decomposition, turns out to be less important in the new decomposition because it is just a little stronger than usual.

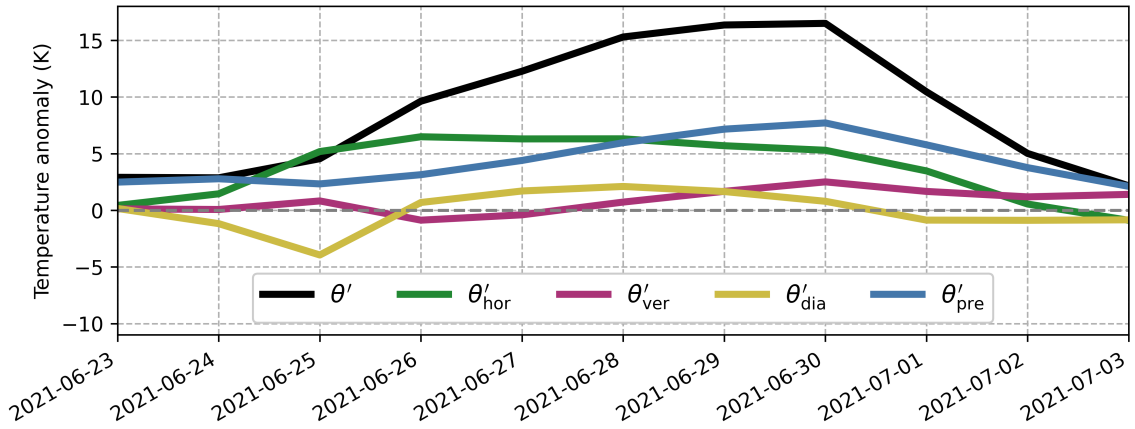

Figure 3.10 – Same as Figure 3.2, but the θ' decomposition terms are now depicted as deviations from their long-term averages.

3.3.3.2 The UK heatwave revisited

Finally, we show the anomaly-based perspective on the UK heatwave. The new decomposition for the time-mean vertical structure (Figure 3.11) also shows substantial differences with respect to the original decomposition. In particular, now the contribution from vertical transport in the lower troposphere does not dominate the decomposition any longer; instead, the contributions from horizontal transport and the pre-existing anomaly are of similar magnitudes. The same behaviour is revealed in the near-surface time series in Figure 3.12.

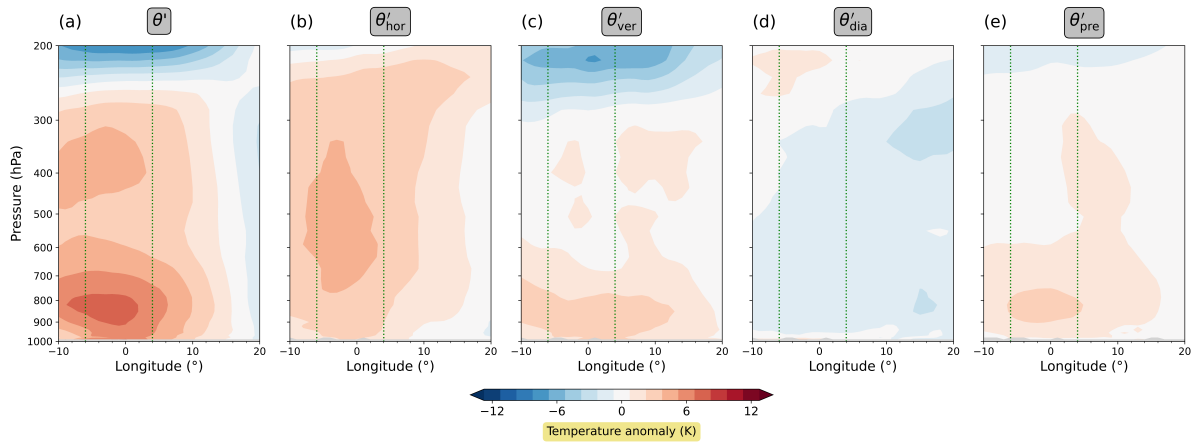

Figure 3.11 – Same as Figure 3.6, but the θ' decomposition terms are now depicted as deviations from their long-term averages.

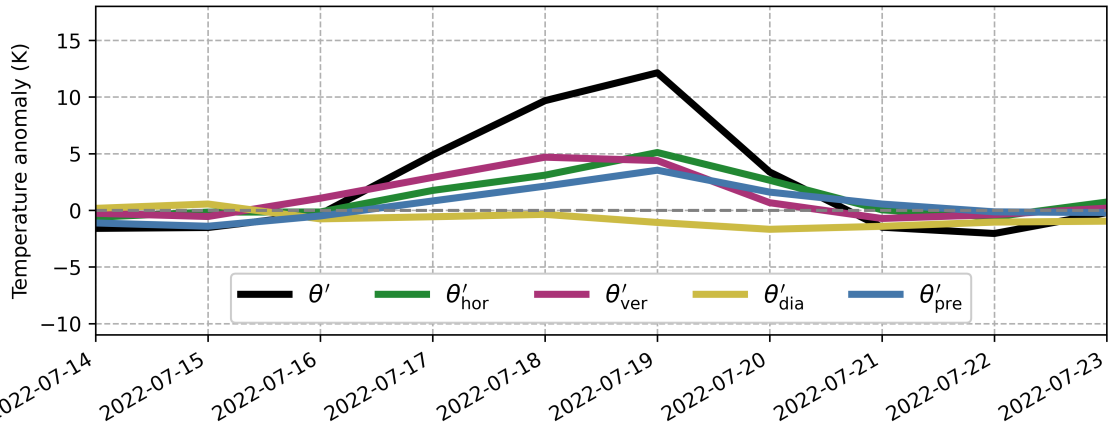

Figure 3.12 – Same as Figure 3.5, but the θ' decomposition terms are now depicted as deviations from their long-term averages.

3.3.4 Statistics for heat extremes in the two heatwave regions

In a final step, we now want to generalise the above results by looking at statistics about heat extremes in the two regions considered. In this section, we will focus on the anomaly-based decomposition.

We choose the following simple definition for a heat extreme. We calculate the spatial average of the near-surface potential temperature anomaly in the respective region for each day between 15 May and 15 September and subsequently select the days on which the 90th percentile is exceeded. This procedure results in 162 days, which we refer to as hot days from the respective region. Our statistical analysis is then based on these selected hot days.

To start with, Figure 3.13 shows vertical cross-sections of θ' and its (anomaly-based) decomposition averaged over all hot days in the respective region. In both regions, near-surface heat extremes are most notably associated with an anomalous positive contribution from horizontal transport throughout the whole troposphere (Figure 3.13b,g), contributing around +3 K on average. Moreover, as indicated by the contour lines, at least 80% of these extremes show an anomalous positive contribution from horizontal transport up to the tropopause. Additionally, in the lower half of the troposphere, the contribution from vertical transport (Figure 3.13c,h) is anomalously positive by about 1–2 K on average, reflecting downwelling in anticyclonic flow during heatwaves. The overall contribution from diabatic heating (Figure 3.13d,i) tends to be anomalously negative (around −1 K), presumably due to anomalous radiative cooling in strongly subsiding air masses. Pre-existing anomalies (Figure 3.13e,j) of 1–2 K on average seem to be nearly always present during heat extremes.

Next, we focus on the near surface and examine the distributions of the near-surface θ' decomposition across all hot days in the respective regions (Figure 3.14, blue histograms).

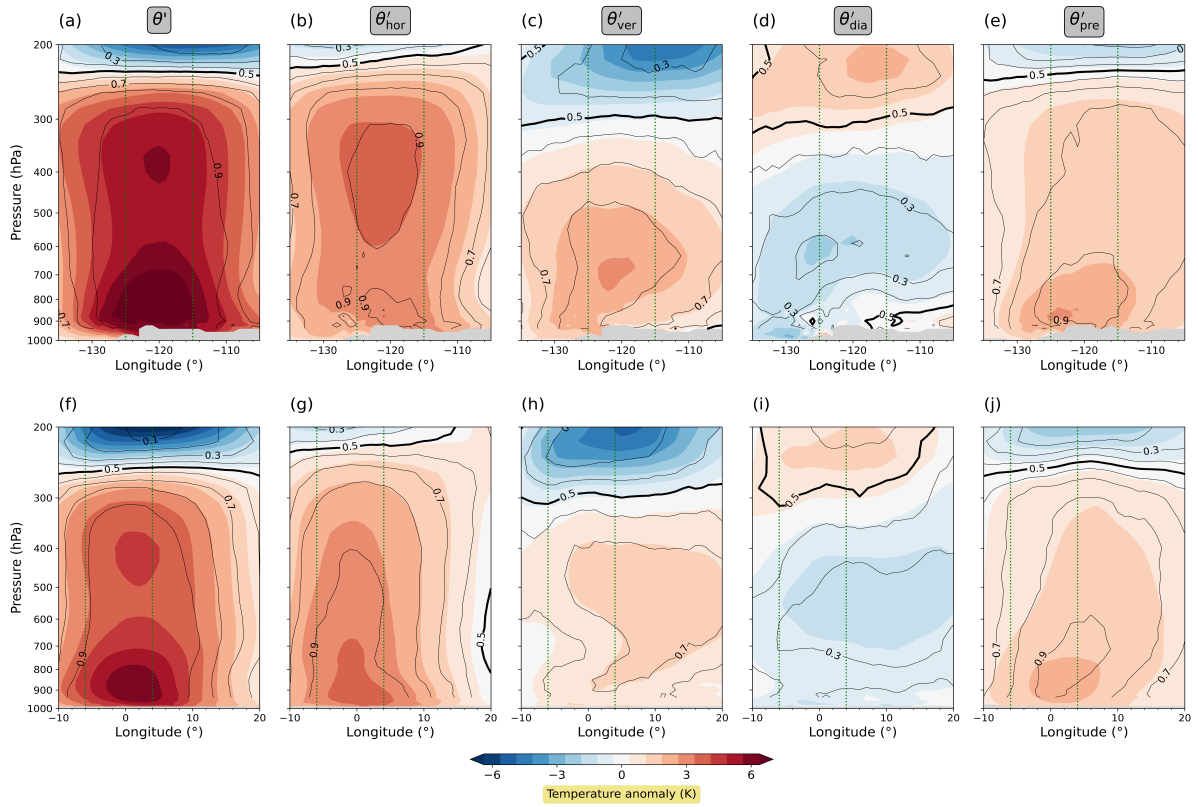

Figure 3.13 – Vertical cross-section displaying statistical parameters of θ' and its decomposition (anomaly-based perspective) for hot days in the Pacific Northwest region (a–e) and in the UK region (f–j). Colours depict the mean, whereas lines depict the fraction of data points that has a positive sign. Fields are latitudinally averaged between 49 and 59° N. The two vertical green lines in each panel indicate the longitudinal extent of the respective region on which the selection of hot days was based.

Most striking is that the distribution of the contribution from horizontal transport is (nearly) exclusively in the positive range of values in both regions (Figure 3.14b,g). This means that (almost) every hot day in the two regions is associated with an anomalous positive contribution from horizontal transport. Similarly, the distribution of the vertical transport also shows a clear shift towards positive values (Figure 3.14c,h), indicating that hot days are usually (94% or 70%, respective to the Pacific Northwest or the UK) associated with an anomalous positive contribution from vertical transport. Likewise, the contribution from the pre-existing anomaly is typically positive (Figure 3.14e,j).

In contrast, the distribution of the diabatic heating is shifted towards negative values, indicating that hot days tend to be associated with less diabatic heating than average. At first glance, this fact may appear paradoxical, given that hot days are typically characterised by cloud-free skies and intense insolation, which may give rise to strong surface fluxes. However, one needs to keep in mind that our contributions represent an accumulation over the past few days of the parcel's trajectory, such that the local processes at the parcel's

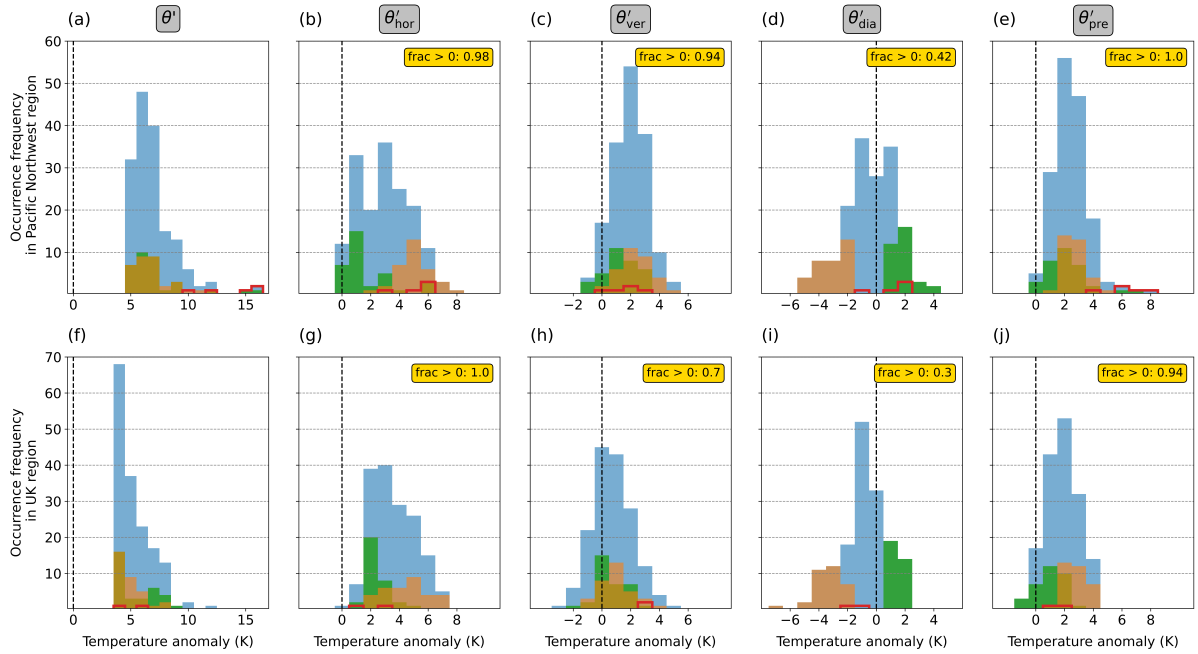

Figure 3.14 – Histograms of occurrence frequency of the near-surface θ' and its (anomaly-based) decomposition for hot days in the Pacific Northwest region (a–e) and in the UK region (f–j). The histograms are based on area mean values. Blue bars depict all data points. Green bars mark those data points that exceed the 80th percentile in diabatic heating, and orange bars mark those data points that are below the 20th percentile in diabatic heating. Red bars denote data points belonging to the heatwaves in 2021 (Pacific Northwest) and in 2022 (UK), respectively. The labels in the top-right corner of each panel give the respective fractions of positive values.

final destination do not necessarily play the dominant role. Substantial surface sensible heating at the parcel's final location will result in a large contribution from diabatic heating only if the parcel is close to the surface for a substantial length of time; otherwise, the surface sensible heating will not have enough time to heat the parcel. As indicated by a larger-than-usual contribution from vertical transport (Figure 3.14c,h), this may not be the case here. Moreover, strong insolation and associated warm soil can only result in anomalously strong transfer of heat from the surface to the atmosphere if at the same time the atmosphere itself is not substantially warmer than usual. However, the latter seems to be the case here. Most air masses have been unusually warm in their recent past (e.g. Figure 3.14e,j), which thus suggests an anomalously weak transfer of heat from the surface to the atmosphere.

In fact, the above reasoning is consistent with our results from Figure 3.14. Apparently, air masses that have undergone unusually strong diabatic heating (indicated by the green bars) are often linked to anomalously small contributions from horizontal transport; on the other hand, the air masses that have undergone unusually weak diabatic heating (indicated by orange bars) tend to be associated with anomalously large contributions

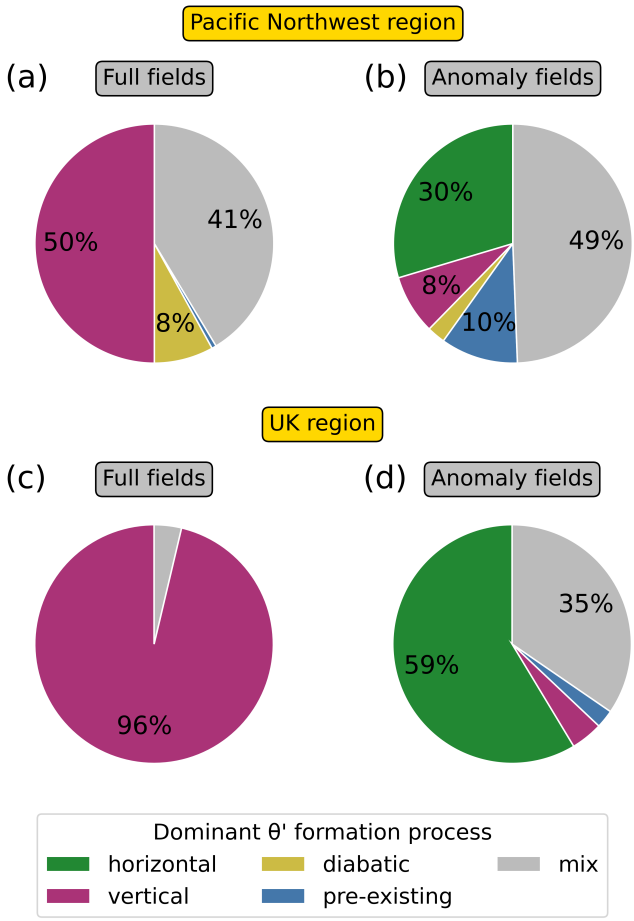

Figure 3.15 – Pie charts displaying the relative frequency of the dominant near-surface θ' formation processes for hot days during summer in the Pacific Northwest region (a,b) and in the UK region (c,d). A single process is considered dominant if it contributes at least 1.5 times as much as the second-highest term. If no single process is identified as dominant, the day is counted as "mix". The pie charts are based on area mean values. In panels (a) and (c), the pie charts are based on the θ' decomposition in terms of the full fields, whereas in panels (b) and (d), the pie charts are based on the θ' decomposition in terms of the anomaly fields.

from horizontal transport. The same qualitative behaviour, albeit less pronounced, can be observed for vertical transport and the pre-existing anomaly, respectively.

It is interesting to contrast this general statistical behaviour with the situation observed in the Pacific Northwest heatwave. During that episode, clearly positive diabatic heating was observed despite strongly positive contributions from horizontal transport (red bars in Figure 3.14b,d). This is consistent with other work suggesting that dry soil contributed to the Pacific Northwest heatwave (e.g. Schumacher et al., 2022; Li et al., 2024). Dry soil can enable unusually strong sensible-heat fluxes despite an already warm atmosphere.

Finally, Figure 3.15 presents an overview of how frequently each of the θ' decomposition terms emerges as the dominant one (see figure caption). We provide results for both decompositions to highlight the contrasts in the θ' decomposition in terms of the full fields versus the anomaly fields. Examining the θ' decomposition through the full fields (Figure 3.15a) reveals that in the Pacific Northwest region, vertical transport can be identified as the dominant process in 50% of all hot days, followed by the diabatic heating in 8% of all hot days. These proportions change drastically when the anomaly-based perspective is adopted (Figure 3.15b). Now, it is the horizontal transport—never identified as dominant in the previous perspective—that most frequently emerges as the dominant process. The same behaviour but even more pronounced can be observed in the UK region (Figure 3.15c,d). Note that the results may be sensitive to the precise definition of dominant, so the exact numbers may not be interpreted too literally. Nevertheless, the stark qualitative differences apparent in Figure 3.15 underscore how strongly the Lagrangian characterisation of heatwaves depends on the perspective.

3.4 Discussion

One of the key findings of our study is that horizontal transport—if viewed from the anomaly-based perspective—makes a strong, if not the strongest, positive contribution to near-surface heat extremes in the regions examined. What we want to emphasise is that this result does not contradict previous studies that concluded that horizontal advection is negligible (e.g. Bieli et al., 2015; Zschenderlein et al., 2019). Instead, our finding should be viewed as an indication that different perspectives result in different interpretations, although the underlying physics remains the same.

For example, Bieli et al. (2015) analysed heat extremes over the British Isles and found "no substantial meridional transport associated with hot extremes and, in particular, no strong advection of air masses from southerly regions". Naturally, they concluded from this finding that "horizontal advection of warm air to locations where its temperature represents a large positive deviation from the climatological mean is thus not the primary mechanism

in the development of hot extremes". However, based on their observation that air masses during colder days originate significantly further north compared to warm extremes, they could have just as reasonably concluded that horizontal advection is relevant for heat extremes in the sense that cold-air advection is weaker than usual. In this context, there seems to be no right or wrong; instead the conclusions drawn are a matter of interpretation or definition.

To be sure, the idea of comparing Lagrangian characteristics of hot air masses with average conditions has been proposed before. For instance, Schielicke and Pfahl (2022) examined variables such as air mass origin, adiabatic heating, and parcel-based diabatic heating for low-level air masses during heatwaves and contrasted them with values that would typically occur in summer. After an extensive analysis, they found no unusual subsidence or diabatic heating during heatwaves over the British Isles and concluded that enhanced transport from warm continental regions in the east is of primary importance for high temperatures. These findings are consistent with our results from the anomaly-based θ' decomposition, which showed that horizontal transport from climatologically warmer regions contributes more on average than vertical transport and diabatic heating to a positive near-surface temperature anomaly in the UK region. The strength of our anomaly-based θ' decomposition is that it provides a systematic and straightforward framework, while other approaches, like the one of Schielicke and Pfahl (2022), may be less generic.

In our method, there is one user-defined parameter, namely λ. In this study, we selected this parameter to be $\lambda^{-1} = 7$ days. We repeated the analysis with $\lambda^{-1} = 3$ days to examine the sensitivity of our results to the value of λ. In the decomposition in terms of the full fields, the contributions from horizontal transport, vertical transport, and diabatic heating were generally smaller in magnitude with $\lambda^{-1} = 3$ days compared to the analysis with $\lambda^{-1} = 7$ days. On the other hand, the contribution from the pre-existing anomaly was generally larger with $\lambda^{-1} = 3$ days compared to the analysis with $\lambda^{-1} = 7$ days. This behaviour can be broadly expected: the analysis with a smaller λ^{-1} captures a smaller fraction of the processes that are accounted for by the larger λ^{-1}, attributing the rest to the pre-existing anomaly. In other words, contributions that are assigned to horizontal transport, vertical transport, or diabatic heating are more likely to be transferred to contributions from the pre-existing anomaly when a small value of λ^{-1} is applied. However, and most importantly, in both heatwaves, the overall vertical structure of the decomposition terms was similar for both values of λ. Similarly, in the anomaly-based decomposition, only small differences between both values of λ occurred. This suggests that, overall, the exact value of λ is of secondary importance.

A further characteristic of our temperature diagnostics is that the pre-existing anomaly usually exhibits the same sign as the actual temperature anomaly. This pattern holds true for not only positive temperature anomalies (see heatwave examples and statistical analysis)

but also negative temperature anomalies (not shown). At first glance, this behaviour might seem disappointing, as our method often fails to completely attribute the observed temperature anomaly to the three physical processes. On the other hand, the existence of a pre-existing anomaly may be the reflection of a very fundamental atmospheric property, namely its persistence. Persistence is a well-known phenomenon over a wide range of timescales and variables (e.g. Pelletier, 1997; Pelletier and Turcotte, 1997; Koscielny-Bunde et al., 1998). Persistence of temperature, for instance, means that warm days (or months or years) are, more often than not, followed by warm days and cold days by cold days. In other words, persistence means that a variable (e.g. temperature) exhibits autocorrelation. This autocorrelation is particularly strong on the synoptic timescale (e.g. Talkner and Weber, 2000; Eichner et al., 2003). Considering the autocorrelation of temperature, it is not surprising that the pre-existing anomaly tends to be (strongly) positive during heatwaves: if there is a large temperature anomaly present today, it is very likely that a temperature anomaly already existed in the vicinity a few days earlier. Therefore, we do not consider our pre-existing term and its behaviour as weaknesses of our method but rather consider it to be a term with genuine physical significance, providing, in some sense, true added value.

Lastly, it is important to acknowledge that Lagrangian methods are generally subject to errors (e.g. Stohl, 1998; Stohl et al., 2002; Mayer and Wirth, 2023). This caveat applies to our analysis just as much as it applies to most previous trajectory-based studies of near-surface heat extremes (e.g. Harpaz et al., 2014; Bieli et al., 2015; Zschenderlein et al., 2019; Spensberger et al., 2020; Catalano et al., 2021; Hochman et al., 2021; Schielicke and Pfahl, 2022; Röthlisberger and Papritz, 2023b; Hotz et al., 2024). One prominent issue is the atmospheric boundary layer, where turbulent mixing and convection are particularly pronounced. These processes are not fully accounted for when simply using mean wind fields from reanalysis data. Nevertheless, we believe that Lagrangian analyses such as ours and previous ones do provide valuable information when carefully interpreted. For instance, we never show results for a single grid point but rather provide information that is aggregated over time or space. The premise is that this aggregation reflects the mean behaviour of real air parcels to a fair approximation. While this assumption may seem strong, questioning it would also cast doubt on the validity of most other trajectory-based studies. Moreover, presumably most of the air parcels spend at least some of their recent history in the free atmosphere, where uncertainties in Lagrangian information are likely to be much smaller.

3.5 Summary and conclusions

In this paper, we analysed heatwaves from a Lagrangian perspective. Core to our Lagrangian analysis was a Lagrangian θ' decomposition based on the T' decomposition proposed by Röthlisberger and Papritz (2023b). Our Lagrangian θ' decomposition partitions a potential temperature anomaly at a given location into contributions from horizontal transport, vertical transport, diabatic heating, and a pre-existing temperature anomaly in order to quantify the relative importance of these processes for the formation of heatwaves.

To obtain the Lagrangian information required for the analysis, we used the method of tracer advection with relaxation introduced by Mayer and Wirth (2023). This sets us apart from the majority of other Lagrangian studies on heatwaves, as we do not rely on trajectory calculations. The tracer method offers the advantage that long periods of data can be processed efficiently, facilitating the computation of climatologies.

First, we applied a decomposition closely resembling the original decomposition by Röthlisberger and Papritz (2023b). We presented the results of that decomposition for two recent heat events, namely the Pacific Northwest heatwave in 2021 and the UK heatwave in 2022. In this context, the preceding study of Hotz et al. (2024), who also used the decomposition by Röthlisberger and Papritz (2023b), served as a template and reference. In both heatwaves, we observed that the upper troposphere experienced positive contributions from horizontal transport and diabatic heating, which were partly compensated by negative contributions from vertical transport. Near the surface, during the Pacific Northwest heatwave, diabatic heating dominated most of the event, whereas during the UK heatwave, vertical transport was clearly dominant. Overall, these results are consistent with the results of the reference study and differ only in details.

Next, we provided, for the first time, long-term averages of the respective terms in the temperature anomaly decomposition. Interestingly, these averages showed similar characteristics to those observed during the heatwave periods. For instance, we observed that in the Pacific Northwest, air masses near the surface typically undergo significant diabatic heating, while in the UK, they experience a substantial positive contribution from vertical transport. This suggested that the notable positive contribution from diabatic heating (observed during the Pacific Northwest heatwave) or from vertical transport (observed during the UK heatwave) may not have been the decisive factor in the unusually high temperatures. Their contributions were substantial, although not exceptionally so. This motivated us to introduce a new temperature anomaly decomposition based on the *anomaly* fields of the respective terms.

Compared to the decomposition in terms of the full fields, the anomaly-based decomposition led to significant differences regarding the relative importance of the respective terms. For example, during the Pacific Northwest heatwave, diabatic heating no longer

constituted one of the largest contributions but was clearly second to the contribution from horizontal transport. Similarly, in the UK heatwave, vertical transport no longer stood out as the sole dominant factor; instead, horizontal transport contributed significantly as well. Loosely speaking, near the surface, the horizontal transport thus emerged as the winner of this shift in perspective.

Finally, we complemented our study with a statistical analysis of hot days in the respective regions. Most notably, this analysis revealed that hot days in both regions consistently coincide with abnormally positive contributions from horizontal transport near the surface, often extending all the way to the tropopause. This suggests that anomalously positive horizontal transport can be regarded as a necessary (but possibly not sufficient) prerequisite for the formation of a heat extreme.

We believe that a lot can be learned from the anomaly-based decomposition, as it inherently provides an intuitive comparison to what can be expected from climatology. However, we are aware that even the anomaly-based decomposition, which may be regarded as an extension of the decomposition originally suggested by Röthlisberger and Papritz (2023b), does not provide answers to all questions. For instance, while we can learn from the anomaly-based perspective that anomalously positive horizontal transport seems to be an inevitable ingredient in the formation of unusually warm temperatures, it does not fully elucidate why certain warm events are more extreme than others. For instance, drier-than-usual soil may be a contributing factor. However, its effect would be clearly reflected in an anomalously strong diabatic heating only if other variables, such as horizontal transport, were not also affecting the diabatic heating. Conditioning on specific factors, such as prescribed dynamics (i.e. prescribed horizontal and vertical transport), might offer a potential avenue to disentangle such effects. Nonetheless, the existing correlations between the respective variables in the decomposition still pose a challenge for drawing causal conclusions.

In summary, our paper suggests that there are at least two different ways to perform a meaningful decomposition of a given temperature anomaly into distinct processes. At the same time, the analysis focused exclusively on the Lagrangian framework; a decomposition in an Eulerian framework would most likely provide yet another perspective. The variety in possible decompositions implies that there is no unique answer regarding the extents to which horizontal transport, vertical transport, and diabatic heating contribute to a given temperature anomaly. Ultimately, the answer to this question seems to be a matter of perspective.

Code and data availability The data presented in this study is available at https://doi.org/10.5281/zenodo.14679142 (Mayer, 2025f). The tracer advection code used to create the data can be accessed at https://doi.org/10.5281/zenodo.14697529

(Mayer, 2025c). The code used to create the plots in this paper is accessible at https://doi.org/10.5281/zenodo.14717758 (Mayer, 2025e). All results are based on the ERA5 reanalysis (Hersbach et al., 2017; Hersbach et al., 2023b)[6] from the European Centre for Medium-Range Weather Forecasts (ECMWF) provided by the Copernicus Climate Change Service (C3S).

Author contributions Amelie Mayer carried out the analysis with some advice from Volkmar Wirth. Both authors jointly wrote the paper.

Disclaimer The results contain modified Copernicus Climate Change Service information 2023. Neither the European Commission nor the ECMWF is responsible for any use that may be made of the Copernicus information or data it contains.

Acknowledgements We thank the Copernicus Climate Change Service for granting free access to the ERA5 data. Parts of this research were conducted using the supercomputer MOGON 2 and/or advisory services offered by Johannes Gutenberg University Mainz (https://hpc.uni-mainz.de, last access: 17 January 2025), which is a member of the AHRP (Alliance for High-Performance Computing in Rhineland Palatinate, https://www.ahrp.info, last access: 17 January 2025) and the Gauss Alliance e.V. The authors gratefully acknowledge the computing time granted on the supercomputer MOGON 2 at Johannes Gutenberg University Mainz. We made occasional use of ChatGPT to refine sentence structures and improve the formulations of an earlier version of this paper.

Financial support This research has been supported by the Deutsche Forschungsgemeinschaft (grant no. SFB/TRR 165).

3.6 Appendix: Reformulation of the equation for θ'

Let τ be the sum of all terms that bring about a change in a parcel's potential temperature anomaly θ', i.e.

$$\tau = \frac{D\theta}{Dt} - \frac{\partial\overline{\theta}}{\partial t} - \boldsymbol{v} \cdot \nabla_{\mathrm{h}}\overline{\theta} - \omega \frac{\partial\overline{\theta}}{\partial p} \,, \tag{A3.1}$$

such that

$$\frac{D\theta'}{Dt} = \tau \,. \tag{A3.2}$$

[6] *The second reference has been added.*

Integrating τ along the parcel's trajectory yields

$$\theta' = \int_{t_0}^{t} \tau \, dt' + \theta'_0 \, . \tag{A3.3}$$

where t_0 is the start time of the integration, t is the time of interest, and θ'_0 is the temperature anomaly at the start time. The integral in Equation (A3.3) can be extended to start at $-\infty$ if, at the same time, the part of the integral that arises from the time interval $(-\infty, t_0)$ is subtracted:

$$\theta' = \int_{-\infty}^{t} \tau \, dt' - \int_{-\infty}^{t_0} \tau + \theta'_0 \, . \tag{A3.4}$$

The latter equation is equivalent to

$$\theta' = \int_{-\infty}^{t} \tau e^{-\lambda(t-t')} \, dt' + \int_{-\infty}^{t} \tau \, \left(1 - e^{-\lambda(t-t')}\right) \, dt' - \int_{-\infty}^{t_0} \tau \, dt' + \theta'_0 \, , \tag{A3.5}$$

where we introduced the exponential weighting that allows the application of our tracer method. Defining

$$R = \int_{-\infty}^{t} \tau \, \left(1 - e^{-\lambda(t-t')}\right) \, dt' \tag{A3.6}$$

and positing that

$$\int_{-\infty}^{t_0} \tau \, dt' = \theta'_0 \tag{A3.7}$$

one obtains

$$\theta' = \int_{-\infty}^{t} \tau e^{-\lambda(t-t')} \, dt' + R \, . \tag{A3.8}$$

Chapter 4

4 A New Global Lagrangian Analysis of Near-Surface Temperature Extremes

A minimally revised version of this chapter was published in:

Mayer, A. (2025g). "A new global Lagrangian analysis of near-surface temperature extremes". *GRL*, 52, e2025GL116696. DOI: 10.1029/2025GL116696

Abstract Temperature extremes strongly affect the society and the environment, yet a complete physical understanding of their formation mechanisms is still lacking. Specifically, the relative importance of the three key processes—horizontal advection, subsidence accompanied by adiabatic warming, and diabatic heating—remains controversial. This paper presents a global quantification of the contributions from these processes to near-surface temperature extremes using the Lagrangian framework. Two Lagrangian potential temperature anomaly decompositions are applied: one based on the full fields of the respective terms, and the other one based on the anomaly fields of the respective terms (i.e. deviations from their corresponding climatologies). The results from the decomposition based on full fields mostly align with those of a previous study, while the decomposition based on anomaly fields offers a different assessment of the roles of the different processes. Most importantly, horizontal transport is attributed the primary role for both extremes globally.

Plain language summary Temperature extreme events can have serious impacts on the society and the environment. However, a full understanding of how temperature extremes form in the Earth's atmosphere is still lacking. What remains especially unclear is whether temperature extremes result from horizontal or vertical transport of air masses or from the heating and cooling of these air masses on their way. This study takes a global approach to assess the roles of these processes in the formation of warm and cold extremes. By tracing the evolution of air masses, the study evaluates the contribution of each process. Following a previous approach, the analysis suggests that warm and cold extremes form

quite differently: While horizontal transport appears to dominate the formation of cold extremes globally, warm extremes seem to result from a variety of processes. However, the current study then reveals that, when considering deviations from climatological conditions for each process, anomalies in the horizontal transport dominate the formation of both warm and cold extremes. Thus, globally, horizontal transport appears to be the key factor in the formation of both extremes.

4.1 Introduction

Temperature extremes, both warm and cold, have a wide-ranging impact on the society and the environment. They can strain energy systems (e.g. Thornton et al., 2016; Añel et al., 2017), threaten public health (e.g. Conlon et al., 2011; Gasparrini et al., 2015; Forzieri et al., 2017), and cause agricultural and economic losses (e.g. García-Herrera et al., 2010; Lesk et al., 2016). Given the socio-economic importance of such temperature extremes, scientists have aimed to develop a comprehensive physical understanding of the processes driving these extreme events. However, this understanding still lacks a scientific consensus on the relative importance of the processes believed to be crucial for the formation of temperature extremes.

Cold extremes have primarily been attributed to the horizontal advection of cold air (e.g. Bieli et al., 2015; Schneider et al., 2015; Garfinkel and Harnik, 2017; Tuel and Martius, 2024), with diabatic cooling sometimes also considered important (e.g. Turner et al., 2013; Papritz, 2020; Hartig et al., 2023). In contrast, warm extremes seem to be more diverse in terms of their underlying mechanisms. Horizontal advection of warm air, adiabatic warming in subsiding air, and diabatic heating have all been identified as key contributors (e.g. Miralles et al., 2014; Sousa et al., 2019; Zschenderlein et al., 2019; Hochman et al., 2021; Schumacher et al., 2022; Hotz et al., 2024). Yet, assessing the relative importance of the different processes remains challenging, and a comprehensive global understanding of their relevance is only about to emerge. A major step forward in this direction was made by Röthlisberger and Papritz (2023a) and Röthlisberger and Papritz (2023b), who conducted the first global quantification of hot and cold extremes, considering all the three processes involved. They employed a novel Lagrangian diagnostic, in which the temperature anomaly changes of an air parcel are tracked separately for each individual process and accumulated along its trajectory. Based on this approach, Röthlisberger and Papritz (2023a) and Röthlisberger and Papritz (2023b) concluded that advection dominates cold extremes globally, while warm extremes show high spatial variability in the contributions from the three processes, with no single process clearly dominant across the globe.

Röthlisberger and Papritz' Lagrangian temperature anomaly decomposition approach is valuable in that it quantifies the extent to which each individual process has acted on an air parcel to form a final anomaly. However, in some respects, the approach may fail to address the key question of which process is actually most relevant to the formation of a given temperature anomaly. One could argue that a particularly large contribution from one term may be irrelevant if a large contribution from this term is a typical feature, i.e. part of the climatology. This issue was recognised by Mayer and Wirth (2025) (Chapter 3 of this thesis), who proposed an alternative decomposition based on anomalies of the individual terms. This decomposition addresses the arguably most relevant question, namely: What is unusual about the processes' contributions in situations where temperatures are unusual? Focusing on two specific regions and episodes, Mayer and Wirth (2025) showed that, for warm extremes, the anomaly-based decomposition can lead to substantially different conclusions about the relative importance of the processes compared to the original decomposition. This finding raises the question of to what extent the decomposition based on anomaly fields might change the conclusions of Röthlisberger and Papritz (2023a) and Röthlisberger and Papritz (2023b) regarding the role of the three processes in the formation of temperature extremes on a global scale.

In this paper we present a new global analysis of near-surface warm and cold extremes with respect to their contributions from horizontal transport, vertical transport, and diabatic heating. We apply both a Lagrangian decomposition based on full fields, similar to that of Röthlisberger and Papritz (2023a) and Röthlisberger and Papritz (2023b), as well as a decomposition based on anomaly fields. We follow Mayer and Wirth (2025) and gain the Lagrangian information required by means of Eulerian tracer advection (Mayer and Wirth, 2023). We will show that our results from the decomposition in terms of full fields mostly align with those of Röthlisberger and Papritz (2023a) and Röthlisberger and Papritz (2023b), who used trajectory calculations to determine the contributions, while the decomposition in terms of anomaly fields offers a rather different assessment, especially with regard to warm extremes.

4.2 Methods and data

4.2.1 Lagrangian θ' decompositions

In this study, the Lagrangian potential temperature anomaly decomposition from Mayer and Wirth (2025) is employed. The decomposition is based on five terms: (1) horizontal transport along climatological horizontal potential temperature gradients; (2) vertical transport along climatological vertical potential temperature gradients; (3) diabatic heating of the air parcel along its trajectory; (4) the local rate of change of the climatological

potential temperature due to seasonality; and (5) a pre-existing potential temperature anomaly. The full contributions from the first four terms can be described via the following Lagrangian integrals:

$$\theta_{\mathrm{hor}}(\boldsymbol{x},t) = \int_{-\infty}^{t} -\boldsymbol{v}\cdot\nabla_{\mathrm{h}}\overline{\theta}\ e^{-\lambda(t-t')}\,dt' \ , \tag{4.1}$$

$$\theta_{\mathrm{ver}}(\boldsymbol{x},t) = \int_{-\infty}^{t} -\omega\,\frac{\partial\overline{\theta}}{\partial p}\ e^{-\lambda(t-t')}\,dt' \ , \tag{4.2}$$

$$\theta_{\mathrm{dia}}(\boldsymbol{x},t) = \int_{-\infty}^{t} \frac{D\theta}{Dt'}\ e^{-\lambda(t-t')}\,dt' \ , \tag{4.3}$$

$$\theta_{\mathrm{sea}}(\boldsymbol{x},t) = \int_{-\infty}^{t} -\frac{\partial\overline{\theta}}{\partial t'}\ e^{-\lambda(t-t')}\,dt' \ , \tag{4.4}$$

where $\boldsymbol{v}$ and ω are the horizontal and vertical winds, respectively, θ is potential temperature with $\overline{\theta}$ its climatology, ∇_{h} is the horizontal gradient, and p is pressure. The integrals accumulate information along the trajectory of the air parcel that happens to be located at location $\boldsymbol{x}$ at time t. The accumulation involves an exponential weighting as one goes backward in time along the parcel trajectory. The decay time associated with the exponential weighting is governed by the parameter λ and effectively determines the timescale of accumulation. The fifth term, the pre-existing potential temperature anomaly, θ_{pre}, reflects the accumulation of the four other terms from earlier times, i.e. up to about λ^{-1} before the considered point in time (see the term R in Equation (6) in Mayer and Wirth (2025)).

Based on the aforementioned terms, a given potential temperature anomaly θ' can be decomposed into the contributions from the respective processes. In Mayer and Wirth (2025), two different approaches for this decomposition have been employed. The first approach is based on the full fields of the respective terms, following the approach of Röthlisberger and Papritz (2023b):

$$\theta' = \theta_{\mathrm{hor}} + \theta_{\mathrm{ver}} + \theta_{\mathrm{dia}} + \theta_{\mathrm{sea}} + \theta_{\mathrm{pre}} \ . \tag{4.5}$$

In contrast, the second approach is based on the anomaly fields of the respective terms, i.e. deviations from their corresponding climatologies (denoted with primes):

$$\theta' = \theta'_{\mathrm{hor}} + \theta'_{\mathrm{ver}} + \theta'_{\mathrm{dia}} + \theta'_{\mathrm{sea}} + \theta'_{\mathrm{pre}} \ . \tag{4.6}$$

The two decompositions (4.5) and (4.6) capture slightly different aspects of the formation of temperature anomalies. Both are mathematically sound, although they are somewhat

complementary. As we will argue, selecting decomposition (4.6) over (4.5) will offer a more meaningful approach to understanding anomalous temperatures, as it eliminates the atmosphere's climatological behaviour, which is of limited use in explaining anomalies. In the following, we apply both decompositions to warm and cold near-surface temperature extremes globally to analyse how the two decompositions differ in the relative importance they assign to the respective processes.

For the accumulation timescale λ^{-1} we selected 3 days for warm extremes and 7 days for cold extremes. This choice reflects the typical Lagrangian lifetimes of temperature anomalies, which have been found to be approximately 3 days on average globally for warm extremes (Röthlisberger and Papritz, 2023b), and somewhat longer for cold extremes (Röthlisberger and Papritz, 2023a). Note that the choice of a fixed and static parameter for λ is a limitation of our approach, as it cannot account for individually varying lifetimes of anomalies. However, experimenting with different values of λ has shown that the main findings of our paper do not sensitively depend on the exact choice of the parameter. In particular, the results for the decomposition in terms of anomaly fields proved to be quite insensitive to the precise value chosen.

In the following analysis, θ_{hor}, θ_{ver} and θ_{dia} will be referred to as the process terms. The seasonality θ_{sea} is usually small and will be neglected. For further details regarding the θ' decompositions the reader is referred to Mayer and Wirth (2025).

4.2.2 Eulerian tracer advection with relaxation

The integrals in Equations (4.1)–(4.4) are obtained using the tracer advection method by Mayer and Wirth (2023). A key feature of this method is that it provides the required time-accumulated Lagrangian information directly as gridded fields available at any time step. The method is based on the offline advection of passive tracer fields including a relaxation term. A separate tracer is required to get a solution for each of the integrals. The term θ_{pre} is computed from Equation (4.5) as a residuum. For more information on the tracer method and its use in calculating the terms in the θ' decomposition the reader is directed to Mayer and Wirth (2023) and Mayer and Wirth (2025).

4.2.3 Data

This study is based on ERA5 reanalysis data (Hersbach et al., 2017; Hersbach et al., 2023b) for the period 2010 to 2022. The θ' contributions are derived from global data at every second model level up to model level 50 with a horizontal resolution of 1° and a temporal resolution of 3 hours. The θ' contributions are obtained every 3 hours and then aggregated to daily means. The fields cover the entire global domain up to the tropopause; however,

this study only presents near-surface fields. For this purpose, all fields have been averaged grid-point-wise over a layer with a vertical extent of 50 hPa following the topography. Climatologies of any variables are computed by individually averaging each day of the year, followed by smoothing these day-specific temporal averages with a 31-day running average. Daily anomalies are calculated as differences from these daily climatologies.

4.2.4 Definition of warm and cold extremes

For warm (cold) extremes we chose the following simple definition. Warm (cold) extremes are defined as days that exceed (fall below) the 90th (10th) percentile of the daily mean near-surface potential temperature anomaly distribution during the warm (cold) season. The warm (cold) season is defined as the period of the year when the climatological daily mean near-surface potential temperature surpasses (is below) the 75th (25th) percentile. The identification of warm and cold extremes is performed for each grid point individually and results in 119 warm and 119 cold days per grid point.

4.3 Results

4.3.1 Decomposition in terms of full fields

We begin by presenting the results of our potential temperature anomaly decomposition in terms of full fields, both for warm and cold extremes. In this context, we compare our results with the findings of Röthlisberger and Papritz (2023a) and Röthlisberger and Papritz (2023b), whose analysis was limited to the hottest and coldest day of each year in a 42 year period. We expect overall good consistency with their results, but differences in the selection of warm and cold extremes and in the decomposition methods (see Mayer and Wirth, 2025) are likely to lead to some deviations.

To start with, Figure 4.1 shows the average near-surface potential temperature anomaly during warm extremes and its decomposition in terms of full fields. We find strong geographical variations in the contributions from the three process terms. Horizontal transport (Figure 4.1b) is positive in most of the extratropics, particularly in the storm track regions, and negative in the subtropics and mid-latitude land areas; it dominates the θ' decomposition in the mid-latitude storm tracks, Greenland, and over Antarctica (green in Figure 4.1f). Vertical transport (Figure 4.1c) is positive everywhere except in regions with pronounced orography, with the largest positive contributions along coastal areas on the western sides of continents and over subtropical oceans, where it dominates the θ' decomposition (blue in Figure 4.1f). Diabatic heating (Figure 4.1d) is positive over land, excluding ice sheets, and negative over oceans, with maxima in dry regions

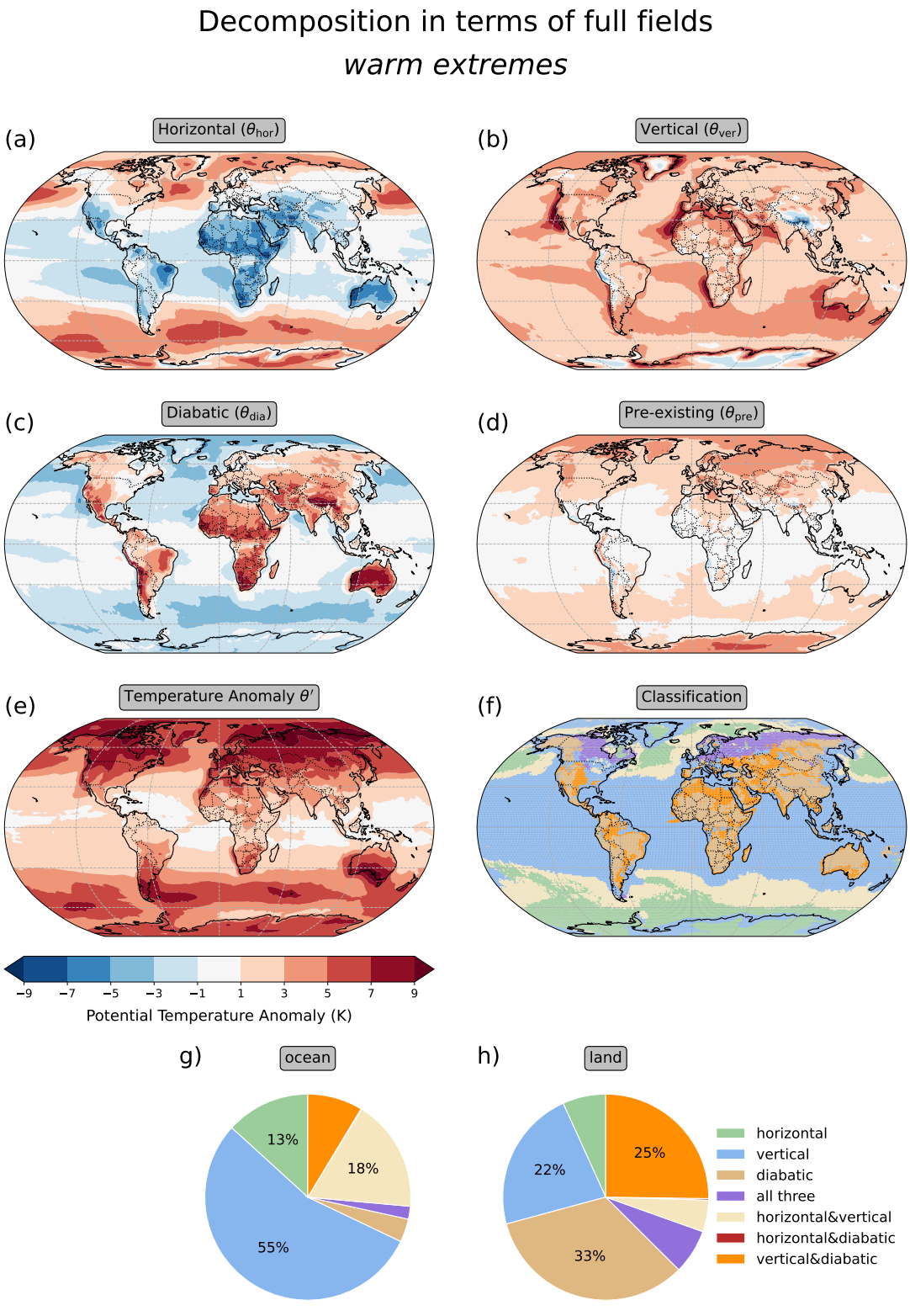

Figure 4.1 – (Caption see next page.)

Figure 4.1 – (Figure see previous page.) The average contributions from horizontal transport (a), vertical transport (b), diabatic heating (c), and pre-existing anomaly (d) to the average near-surface potential temperature anomaly (e) during warm extremes in 2010-2022 at each grid point. Contributions are given in terms of full fields. In (f), all grid points are categorised based on their θ' decomposition, following the categorisation from Röthlisberger and Papritz (2023b). The figure depicts the category that occurs most often across all hot days. Green, blue, and brown colours represent regions where either horizontal transport, vertical transport, or diabatic heating dominates, whereby a process is considered dominant if its contribution is the only positive one or if it is at least twice as large as the contribution from the second most important process. In purple regions, no single process dominates, but all three contribute positively to the anomaly. Light brown, red, and orange regions also lack a dominant process, but show positive contributions from two processes, with the remaining one being negative. The pie charts depict the occurrence frequency for each category across all hot days over land (g) and ocean (h) grid points, with a cosine-based area weighting applied to compensate for the meridian convergence towards high latitudes.

like western Australia and western Africa. In many tropical and subtropical land regions, diabatic heating dominates the θ' decomposition (brown in Figure 4.1f). The pre-existing potential temperature anomaly (Figure 4.1e) is overall positive and particularly large over northern Eurasia, Greenland, and Antarctica, consistent with a larger mean Lagrangian age of the potential temperature anomalies in these regions (Röthlisberger and Papritz, 2023b). Substantial positive contributions from multiple processes are evident in several areas, such as northern Eurasia and eastern Canada, where all three processes contribute similarly (purple in Figure 4.1f). Overall, vertical transport is the dominant process over the ocean (Figure 4.1g), whereas diabatic heating prevails over land (Figure 4.1h).

Next, Figure 4.2 shows the average near-surface potential temperature anomaly during cold extremes and its decomposition in terms of full fields. Horizontal transport (Figure 4.2b) is negative across most areas, and notably large negative contributions—sometimes even exceeding the magnitude of the final anomaly—are found in the storm track regions. Here, horizontal transport is often the only negative contributor and its strong contributions are partially offset by the other terms (see also Röthlisberger and Papritz, 2023a). Vertical transport (Figure 4.2c) mostly contributes positively, except in elevated regions, with maxima over the oceans. Diabatic heating (Figure 4.2d) is negative over the mid-to-high latitude Northern Hemisphere continents, the ice sheets, and parts of the tropical oceans, with the largest negative contributions in Siberia and Antarctica. In contrast, diabatic heating is positive over the extratropical oceans, with particularly large values in the storm track regions. The contribution from the pre-existing potential temperature anomaly (Figure 4.2e) is generally negative, but relatively small compared to the other terms. Globally, horizontal transport dominates the θ' decomposition, both over

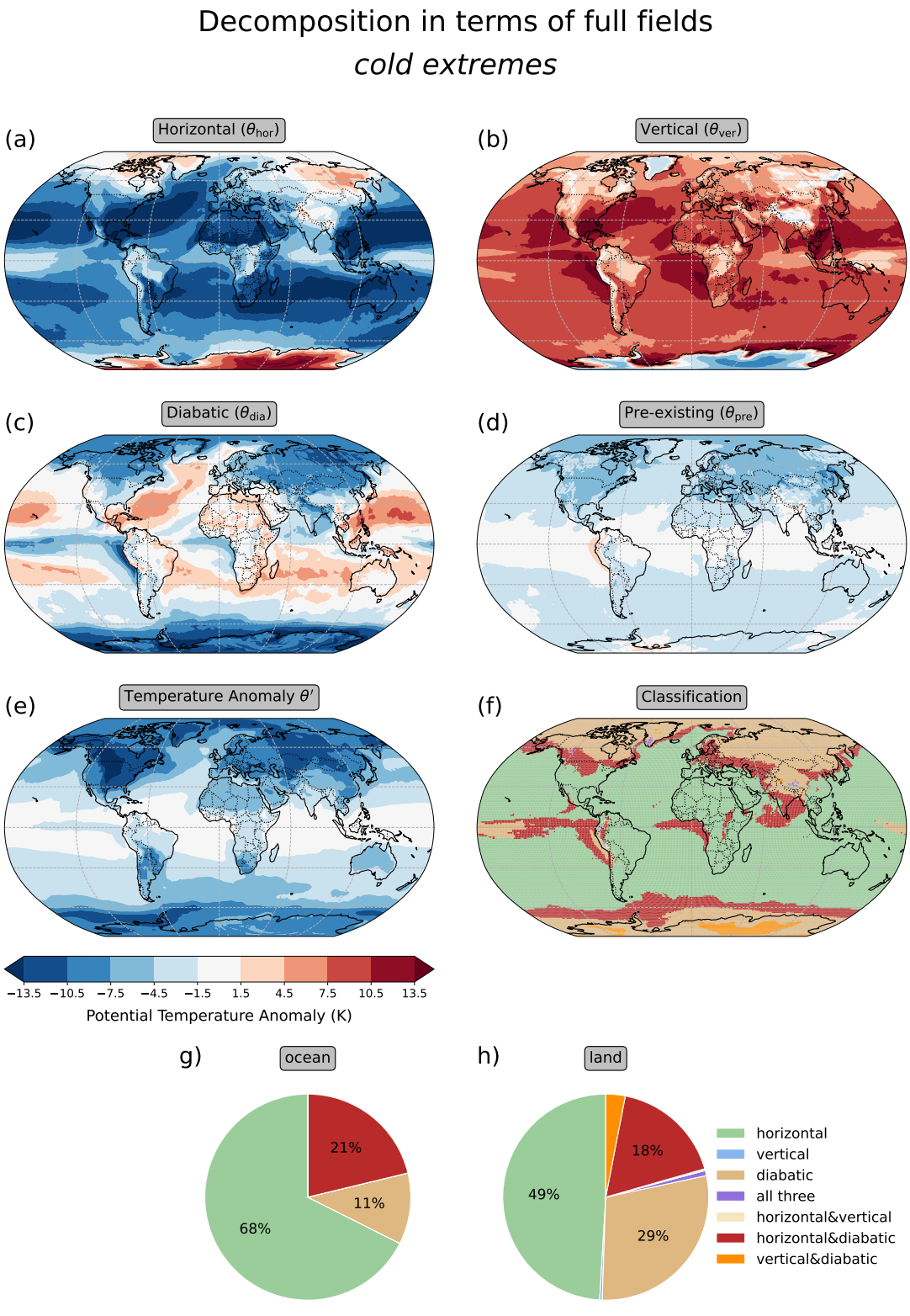

Figure 4.2 – Same as Fig. 4.1, except for cold extremes.

the ocean and over the land (Figure 4.2g,h). In summary, we find a gradual transition from cold extremes mostly driven by diabatic heating in the climatologically coldest regions (brown in Figure 4.2f) to cold extremes dominated by horizontal transport (green in Figure 4.2f) in climatologically warmer regions.

Overall, the findings for both warm and cold extremes are in good agreement with the results from Röthlisberger and Papritz (2023a) and Röthlisberger and Papritz (2023b) (also see Figure S4.1 and Figure S4.2), with only minor differences being apparent. These differences appear mostly in areas with pronounced orography, likely due to the challenge of accurately computing the temperature gradients in these regions (Röthlisberger and Papritz, 2023b). Additional differences occur in regions where the pre-existing term dominates, suggesting a link to the longer timescale over which the anomalies form in these regions (Röthlisberger and Papritz, 2023b). However, the overall good agreement with Röthlisberger and Papritz (2023a) and Röthlisberger and Papritz (2023b) suggests that the process terms in our potential temperature anomaly decomposition do capture the key processes of anomaly formation similarly to theirs, despite some differences in the decomposition approaches, and in particular, our additional pre-existing anomaly term.

4.3.2 Decomposition in terms of anomaly fields

Now we turn to the decomposition in terms of anomaly fields and analyse to what extent this decomposition differs from the decomposition in terms of full fields. This analysis is motivated by the fact that many characteristics of the process terms described earlier are largely inherent to the climatological behaviour (see Figures S4.3 and S4.4) and, as such, may not be useful in "explaining" an *anomalous* behaviour (temperature). For instance, it was diagnosed that diabatic heating during warm extremes is substantially positive over large parts of the continents and, thus, contributes substantially to warm extremes there. However, this diabatic heating is not unique to warm extremes, but also applies to the warm season as a whole (see Figure SS4.3c). Consequently, a decomposition that focuses specifically on the unusual behaviour of the process terms may provide a more effective framework for "understanding" unusual temperatures.

Figure 4.3 depicts the decomposition in terms of anomaly fields for warm extremes. Most notably, the decomposition in terms of anomaly fields differs from the one in terms of full fields in the role of horizontal transport (Figure 4.3b). While horizontal transport showed negative contributions in many parts of the Earth in the decomposition in terms of full fields, the decomposition in terms of anomaly fields reveals positive contributions almost everywhere, except in a few tropical regions. The decomposition in terms of anomaly fields accounts for the fact that horizontal cold air transport is "normal" across large areas near the Earth's surface (see Figure S4.3a) and, therefore, represents the absence or reduction

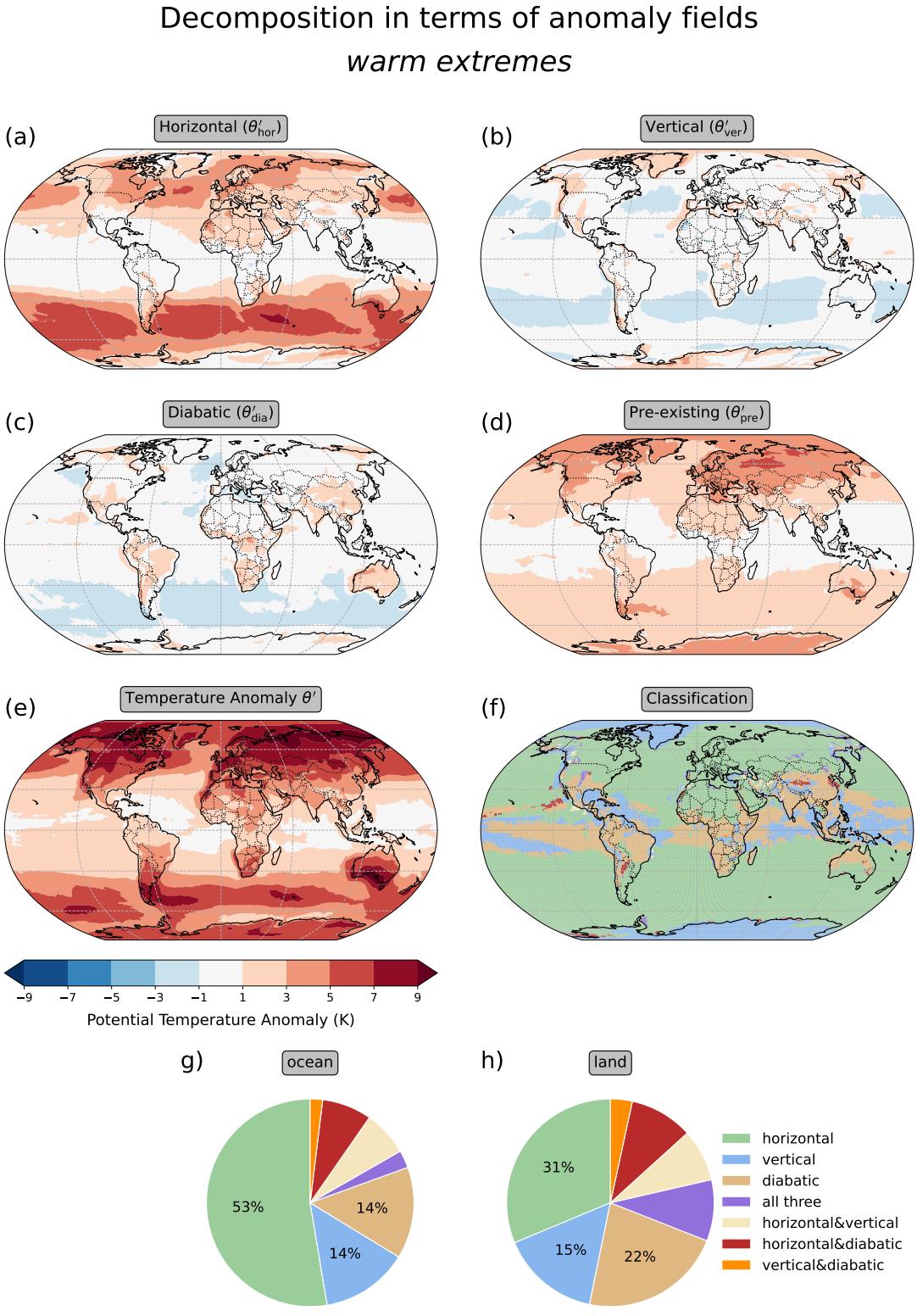

Figure 4.3 – Same as Fig. 4.1, but the contributions are now depicted in terms of anomaly fields.

of this cold air transport as a positive contribution in the decomposition. Contrary to horizontal transport, the contribution of vertical transport (Figure 4.3c) is smaller in the decomposition in terms of anomaly fields compared to the decomposition in terms of full fields, such that noticeably more areas occur where vertical transport contributes negatively. The decomposition in terms of anomaly fields takes into account that most air masses near the surface could only have arrived there through subsidence (indicated as overall positive contributions in the climatology, see Figure S4.3b), and provides a positive contribution only if the subsidence is stronger than usual. Diabatic heating (Figure 4.3d) is still mostly positive over land and negative over oceans, though its magnitude is noticeably smaller compared to the decomposition in terms of full fields.

Overall, the shift to the decomposition in terms of anomaly fields yields a new and somewhat different assessment of the dominant formation processes of warm extremes globally. Most importantly, horizontal transport controls most of the extratropics (green in Figure 4.3f) and parts of the subtropics and tropics. Moreover, the dominant role of vertical transport in the subtropical and tropical oceans is limited to lower latitudes compared to the decomposition in terms of full fields. Diabatic heating (brown in Figure 4.3f) remains the dominant process in many tropical and subtropical regions, but similar to vertical transport its dominance over land is confined to lower latitudes compared to the decomposition in terms of full fields. Instead, diabatic heating now prevails in parts of the tropical ocean. Globally, horizontal transport dominates, both over the ocean and over the land (Figure 4.3g,h).

Finally, Figure 4.4 presents the decomposition in terms of anomaly fields for cold extremes. Most importantly, the role of vertical transport (Figure 4.4c) is assessed differently compared to the decomposition in terms of full fields. That is, vertical transport now reveals substantial negative contributions, primarily over Siberia, Canada, and the northern polar regions. These occurrences of negative contributions from vertical transport are a major difference compared to the decomposition in terms of full fields, which does not allow vertical transport to contribute negatively to cold extremes in non-elevated regions. Thus, the decomposition in terms of anomaly fields opens up the possibility for vertical transport to actually contribute in an amplifying way to a cold anomaly—in distinct contrast to the decomposition in terms of full fields. In certain areas, vertical transport even dominates the formation of cold extremes (blue in Figure 4.4g). In contrast to vertical transport, the role of horizontal transport (Figure 4.4b) does not differ substantially from its role in the decomposition in terms of full fields. As before, its contribution is negative in most regions across the globe. Overall, the magnitude is smaller compared to the decomposition in terms of full fields; however, horizontal transport still constitutes the major formation process for cold extremes globally (Figure 4.4g,h). Interestingly, with the shift to the decomposition in terms of anomaly fields, diabatic cooling (Figure 4.4d) loses

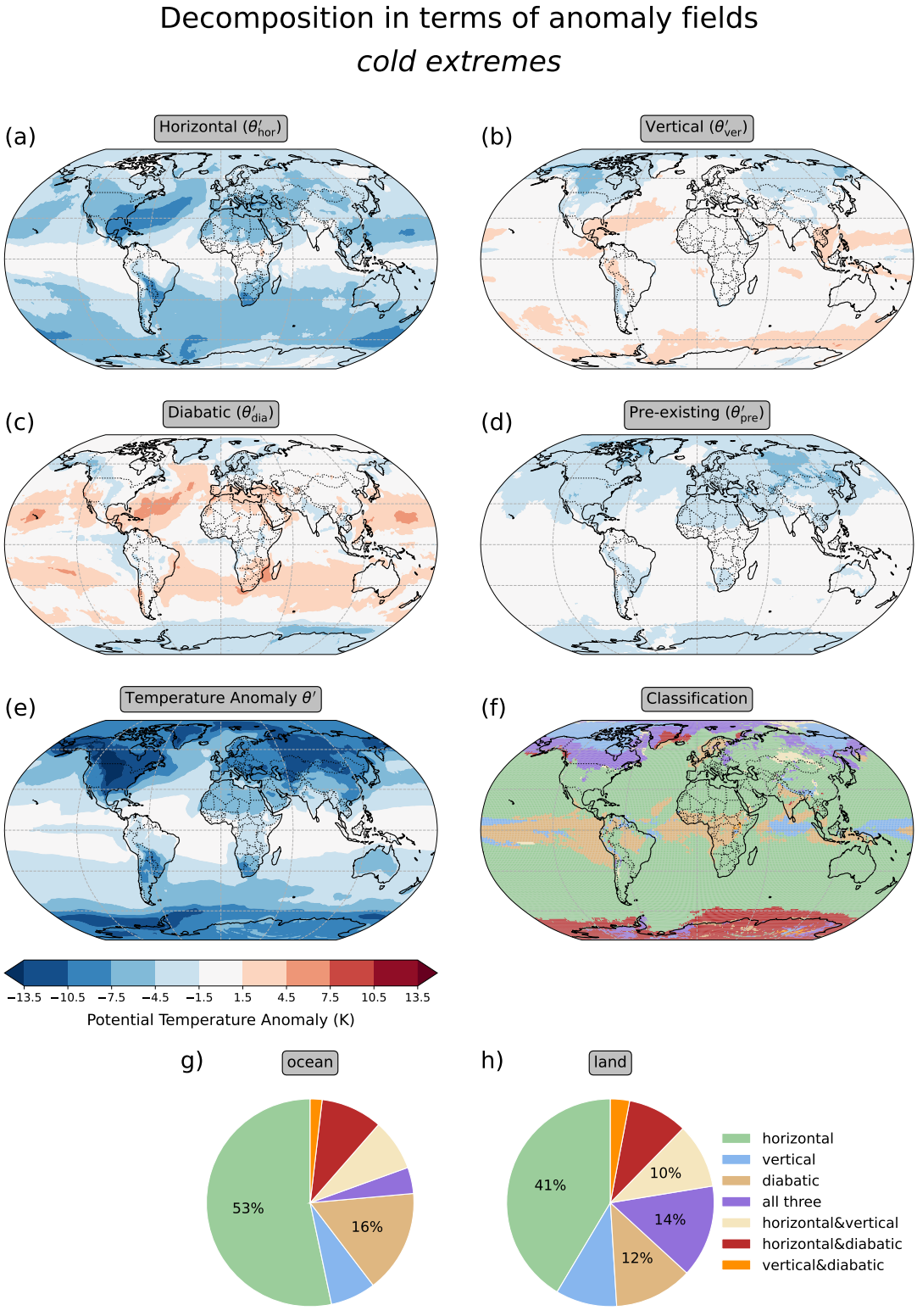

Figure 4.4 – Same as Fig. 4.2, but the contributions are now depicted in terms of anomaly fields.

its role as key formation process for cold extremes in the coldest regions, where substantial diabatic cooling is typical during the cold season (see Figure S4.4c). In contrast, diabatic cooling becomes the leading process for cold extremes in parts of the tropics (brown in Figure 4.4f).

4.4 Discussion and conclusions

This paper presents a new global quantification of the roles of horizontal transport, vertical transport, and diabatic heating for the formation of near-surface warm and cold temperature extremes based on a new Lagrangian temperature anomaly decomposition. As a first step—and to connect with existing literature—we applied a decomposition based on the absolute contributions of the respective processes, which yielded results largely similar to Röthlisberger and Papritz (2023a) and Röthlisberger and Papritz (2023b) for both warm and cold extremes. The similarity of these results not only confirms our approach but also reinforces the findings of Röthlisberger and Papritz (2023a) and Röthlisberger and Papritz (2023b), establishing them on a broader statistical basis. This quantification assigns distinctly different roles to the various processes in the formation of warm and cold extremes. In particular, on a global scale, horizontal transport is attributed an important role only in the formation of cold extremes, but not in the formation of warm extremes.

However, we then showed that the relative importance of the three processes is assessed substantially differently on a global scale when a new quantification based on anomaly fields of the respective terms is applied. The new quantification was motivated by the finding that many aspects of the processes' contributions are associated with the atmosphere's climatological behaviour and, as such, may offer limited value in understanding anomalous temperatures. In the new quantification, horizontal transport emerges as a key contributor not only to cold extremes, but also to warm extremes across large parts of the globe. This finding thus extends the findings of Mayer and Wirth (2025) beyond the two specific regions they studied. In general, the quantification in terms of anomaly fields emphasises the dominance of horizontal transport in the generation of temperature extremes and deemphasises the role of diabatic heating.

Our new quantification extends the quantification by Röthlisberger and Papritz (2023a) and Röthlisberger and Papritz (2023b) by interpreting the contributions from the respective processes with respect to their climatological behaviour—a behaviour that yields contributions substantially different from zero. More precisely, the new quantification systematically describes the highly anomalous temperatures during hot and cold extremes in terms of anomalies in the underlying process terms. In doing so, it addresses the arguably truly interesting question of what exactly is anomalous in situations where temperatures

are highly anomalous—a question we believe the quantification in terms of absolute fields narrowly misses.

Despite some limitations in our method, such as the presence of a pre-existing anomaly which leaves room for some unexplained anomaly and uncertainty in our results, we believe this study represents an important step forward in advancing our understanding of the formation of temperature extremes. For the first time on a global scale, the study makes a clear attempt to quantify, from a Lagrangian perspective, the unusual behaviour during temperature extremes through capturing the unusual behaviour of the process terms—arguably a crucial, if not the most crucial, element in understanding the formation of temperature extremes.

Open Research Section The code to reproduce the data analysis and all figures of this article is available at https://doi.org/10.5281/zenodo.15853875 (Mayer, 2025a). The data is available at https://doi.org/10.5281/zenodo.15827328 (Mayer, 2025b) and the tracer advection code used to create the data is available at https://doi.org/10.5281/zenodo.14773247 (Mayer, 2025d). All results are based on the ERA5 reanalysis (Hersbach et al., 2017; Hersbach et al., 2023b) from the European Centre for Medium-Range Weather Forecasts (ECMWF) provided by the Copernicus Climate Change Service (C3S). The results contain modified Copernicus Climate Change Service information 2024. Neither the European Commission nor the ECMWF is responsible for any use that may be made of the Copernicus information or data it contains.

Acknowledgements We thank the Copernicus Climate Change Service for granting free access to the ERA5 data. Additionally, the author is grateful to Volkmar Wirth for fruitful discussions on the topic of this paper.

4.5 Supporting information

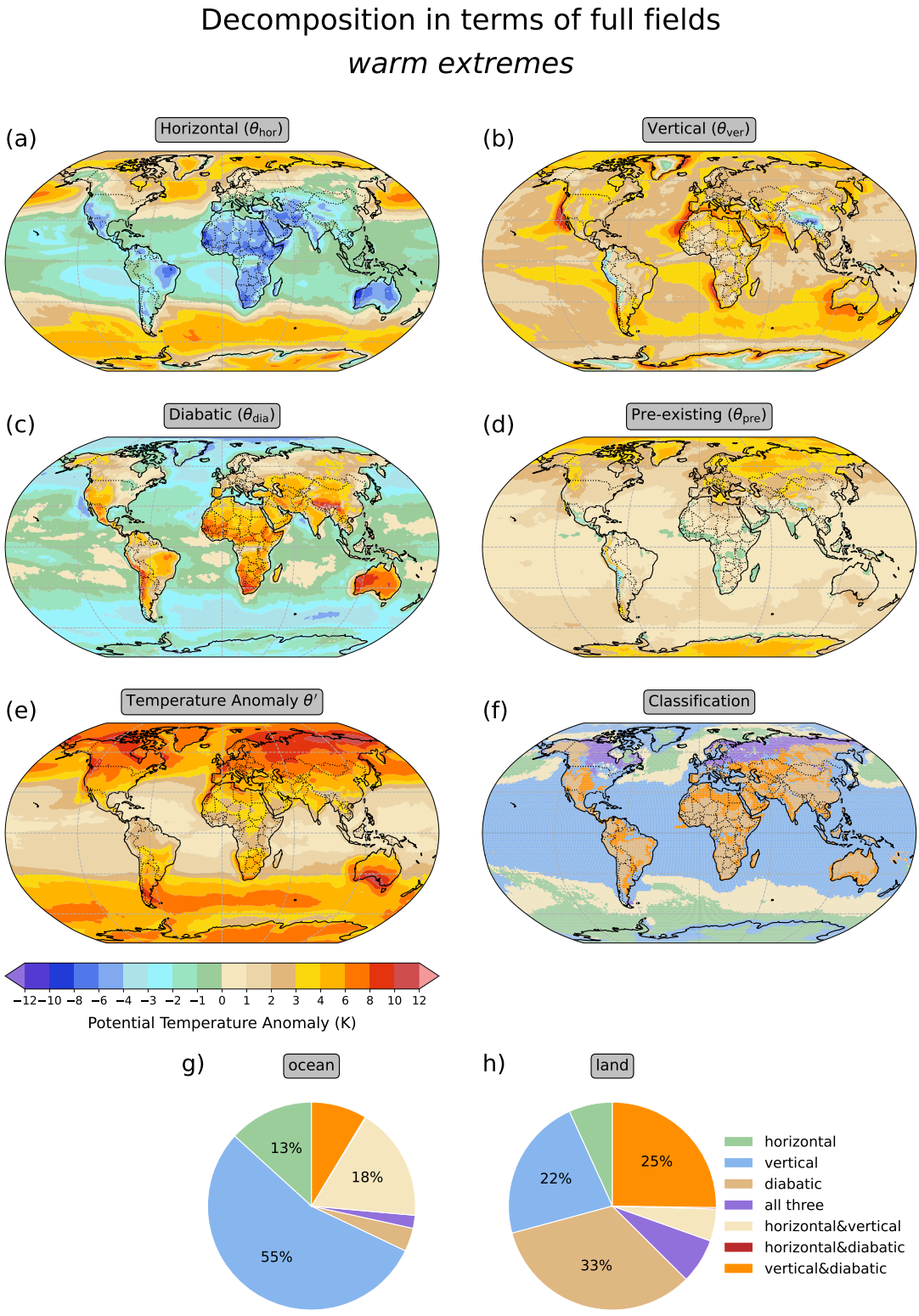

Figure S4.1 – Same as Figure 4.1, but using the same colour scheme as Röthlisberger and Papritz (2023b) for (a–e).

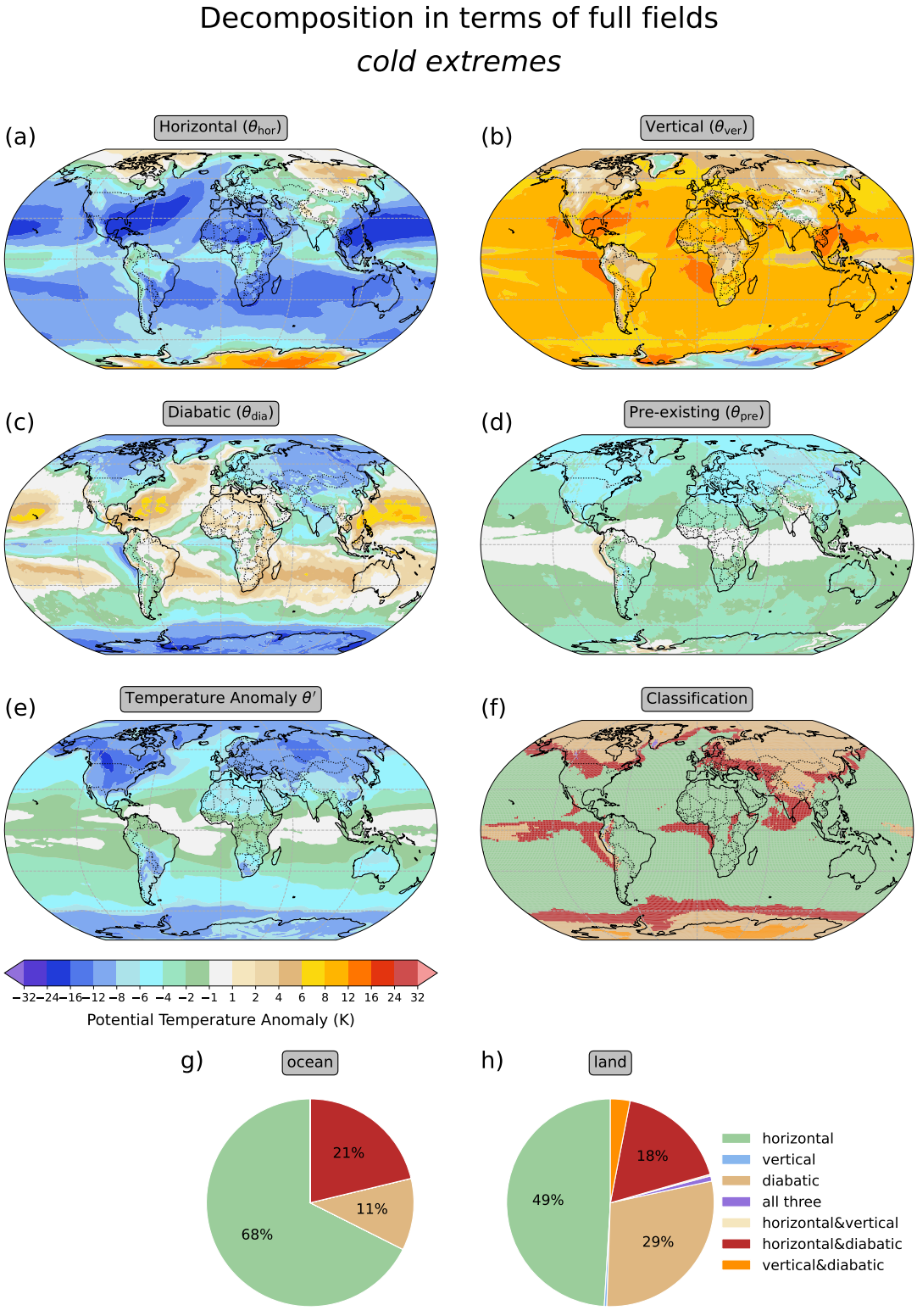

Figure S4.2 – Same as Figure 4.2, but using the same colour scheme as Röthlisberger and Papritz (2023a) for (a–e).

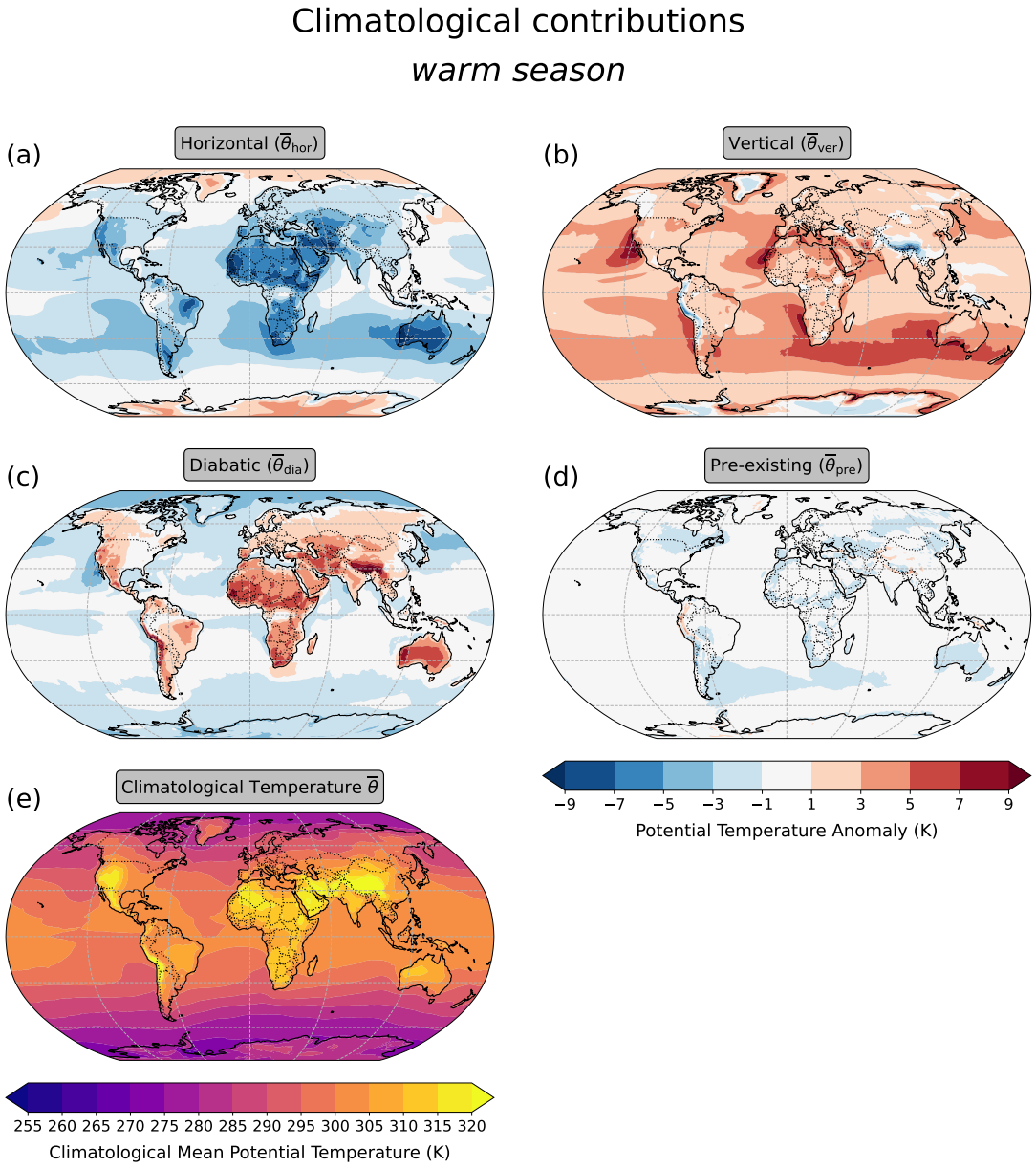

Figure S4.3 – Climatological contributions from horizontal transport (a), vertical transport (b), diabatic heating (c) and the pre-existing anomaly (d) temporally averaged at each grid point over the respective warm season. (e) depicts the climatological mean near-surface potential temperature averaged over the warm season.

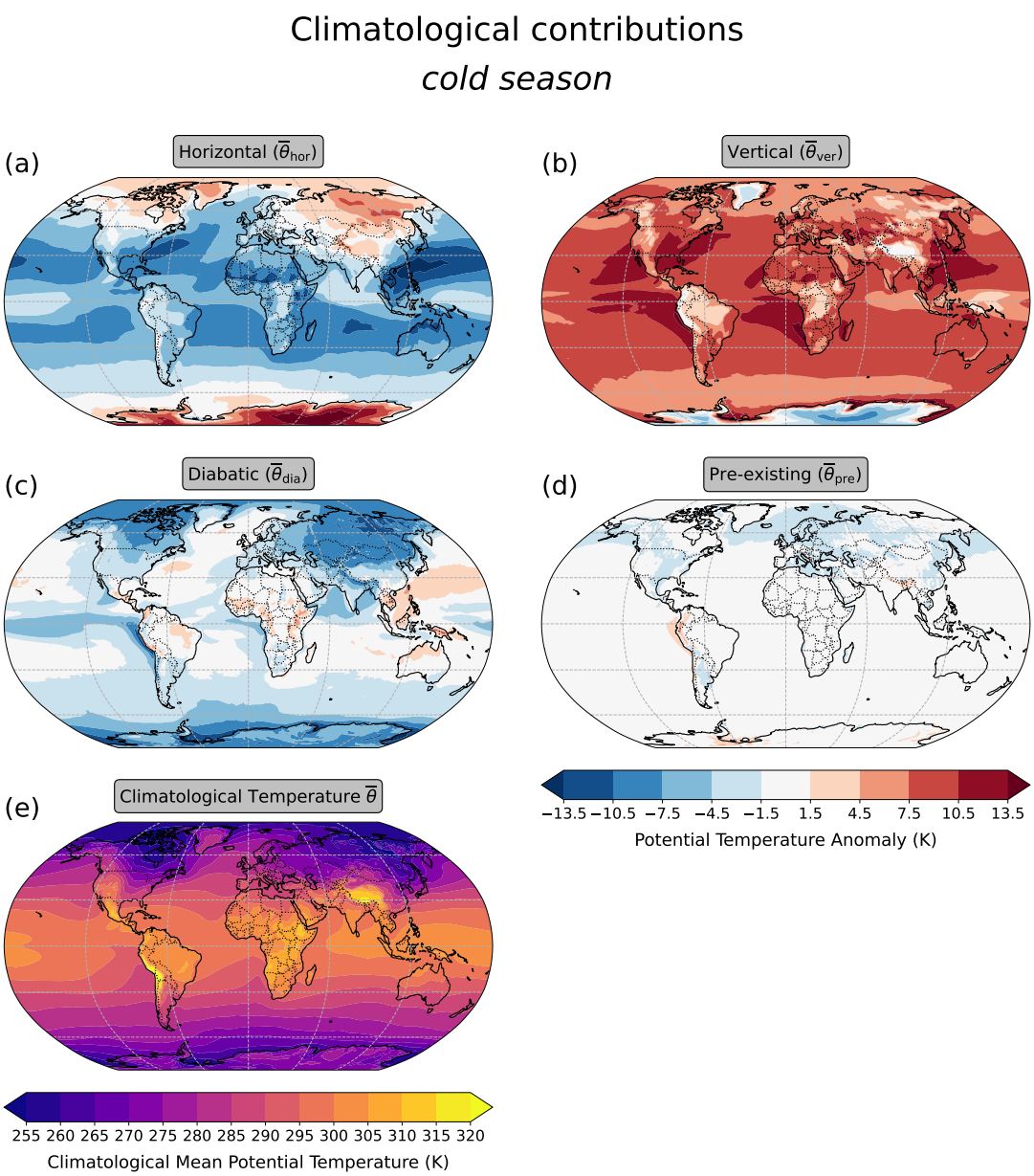

Figure S4.4 – Same as Fig. S4.3, but for the cold season.

Chapter 5

5 Summary and Conclusions

One of the still widely debated questions in the field of heat extremes research is the distinct roles and relative importance of the different processes that contribute to their formation. A framework that has proven particularly valuable in advancing our process-based understanding of heat extremes is the Lagrangian one, in which air masses are followed over time and their thermodynamical history is traced. Many studies have employed this framework to quantify, for example, the degree of diabatic heating or adiabatic warming that air masses associated with heat extremes have undergone in their recent past (e.g. Quinting and Reeder, 2017; Zschenderlein et al., 2019; Hochman et al., 2021). However, so far, hardly any of these Lagrangian studies have evaluated the degree to which the contribution from these processes differ from what air masses typically experience. In other words, almost none of these studies have systematically described the anomalous behaviour during heat extremes in terms of anomalies in the contributions from the underlying processes. At this point, this thesis makes a step forward: For the first time within the Lagrangian framework, all the discussed processes—horizontal advection, subsidence, and diabatic heating—are systematically quantified while accounting for their climatological characteristics, enabling a clearer understanding of the unusual behaviour during heat extremes by capturing the unusual contributions from the processes.

To achieve this goal, we developed a new method for extracting Lagrangian information about the atmospheric flow. The method is based on the advection of passive tracer fields in combination with a relaxation term. At its core, the method links physically meaningful parcel-based information with the grid-point-based framework that is convenient for data analysis, combining the strengths of both the Lagrangian and Eulerian approaches. Most importantly, the method is tailored to gaining Lagrangian information directly in a format well-suited for compiling climatologies.

In the thesis, we applied the method to reanalysis data from the past decade, which prompted a re-evaluation of the relevance of the discussed processes of heat extreme formation. More precisely, the new method provided us with the means to assess the relative importance of the discussed processes not only in terms of their absolute contributions, as done before by, e.g., Röthlisberger and Papritz (2023b) and Hotz et al. (2024), but, for the first time, also in relation to their climatological contributions. The schematic in Figure 5.1 illustrates the key findings from this assessment. When viewed in terms of

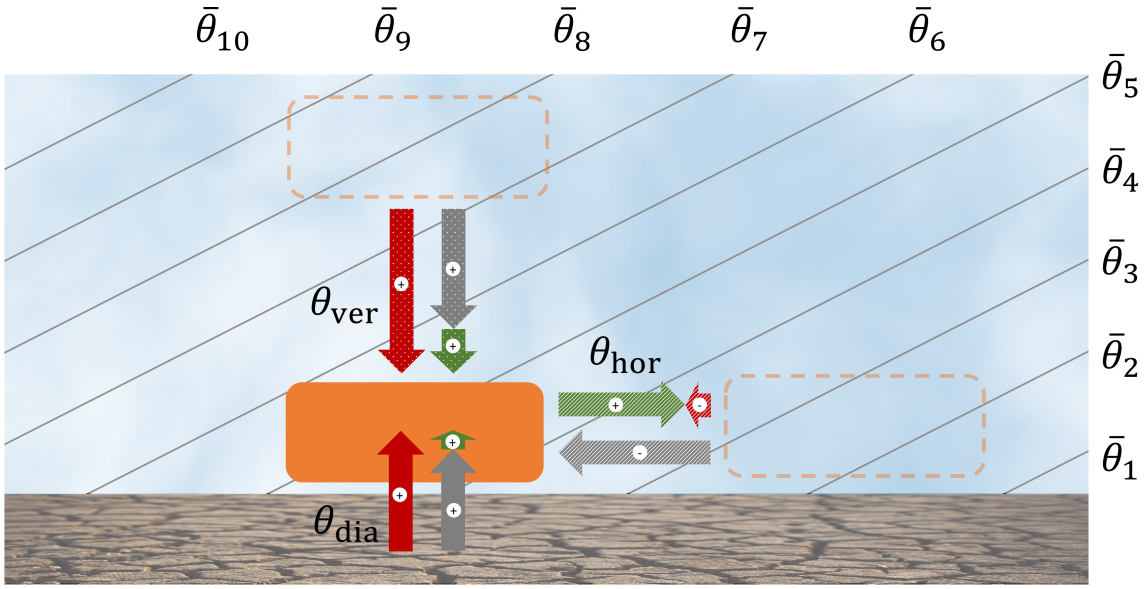

Figure 5.1 – Schematic illustrating the relative importance of horizontal advection (θ_{hor}; striped arrows), subsidence (θ_{ver}; dotted arrows), and diabatic heating (θ_{dia}; solid arrows) to a typical heat extreme (visualised by the orange box) in the extratropics. Red arrows depict the contributions in terms of absolute fields, grey arrows depict the climatological contributions, and green arrows depict the differences, i.e. the contributions in terms of anomaly fields. The length of the arrows indicates the typical magnitude of the contributions, with plus and minus signs denoting their typical sign. The typical magnitudes were calculated as the near-surface averages over all warm extremes in the midlatitudes over land. Note that for horizontal advection the signs between the contributions in terms of absolute and anomaly fields differ. Black contours illustrate climatological mean isentropes with $\overline{\theta}_1 < ... < \overline{\theta}_{10}$. The contribution from the pre-existing term, i.e. from prior temperature anomalies near the air mass origins, is not shown.

absolute values, subsidence ($\sim +2.6$ K; dotted red arrow) and diabatic heating ($\sim +1.9$ K; solid red arrow) typically contribute more than horizontal advection (~ -0.4 K; striped red arrow) to heat extremes in the midlatitudes. We demonstrated this finding through two region studies and a global statistical analysis, which corroborated the results of Hotz et al. (2024) and Röthlisberger and Papritz (2023b). However, taking into account that near-surface air masses typically experience strong positive contributions from subsidence ($\sim +1.9$ K; dotted grey arrow) and diabatic heating ($\sim +1.6$ K; solid grey arrow), along with a notable negative contribution from horizontal advection (~ -2.4 K; striped grey arrow), considerably changes the ranking of these processes in terms of their relative importance. When evaluated relative to their climatological contributions, horizontal advection ($\sim +2.0$ K; striped green arrow) actually contributes more than twice as much as subsidence ($\sim +0.7$ K; dotted green arrow) and diabatic heating ($\sim +0.3$ K; solid green arrow). We argue that the latter assessment provides a more meaningful interpretation,

as it addresses the interesting question of what exactly is different in situations where temperatures are highly different from climatology—a question we believe the quantification in terms of absolute contributions narrowly misses. In essence, our analysis suggests that it is not a slightly enhanced subsidence nor an unusually strong diabatic heating, but rather the absence or a reduction of cold-air advection that typically constitutes the most substantial contribution to heat extremes in the extratropics. Thus, we consider horizontal advection to be, on average, the most important process.

At this point, we would like to emphasise that, although our study highlights the importance of horizontal advection, our results are not fundamentally in conflict with those of Bieli et al. (2015) and Zschenderlein et al. (2019), which consider horizontal advection to play only a minor role. Over Europe, we found little to no contribution from horizontal advection in terms of absolute fields, which is consistent with their findings that the origin of air masses during heatwaves is typically located near the affected region. Both studies concluded that heatwaves are unlikely to be associated with warm southerly advection—a view we share. However, both studies went further concluding that "the geographic origin—and therefore the original temperature—is of minor importance" and that "rather more important are the pathway and the processes, that is, vertical motion and diabatic heating, along the trajectories" (Zschenderlein et al., 2019; a similar statement was made in Bieli et al., 2015). It is on this point that we disagree. We argue that the geographic origin does matter, in the sense that air masses involved in heat extremes tend to exhibit substantially warmer initial temperatures than usual. We showed that this temperature difference typically exceeds that resulting from increased subsidence or diabatic heating, and therefore conclude that horizontal advection is the decisive factor. This finding is corroborated by Schielicke and Pfahl (2022), the only other study we are aware of that compares heatwave air masses with a Lagrangian climatology. They found substantial differences in potential temperature a few days prior to the initialisation of the trajectories, which they primarily attributed to differences in horizontal origin; especially over the British Isles, where no differences in subsidence were found.

Through our anomaly-based approach, we have introduced a new quantitative method that has not previously existed in the Lagrangian framework for studying heat extremes. We feel that this approach is highly valuable, as it is grounded in the most physically meaningful Lagrangian framework while providing an intuitive way to assess the Lagrangian information in a suitable context—namely, in relation to what can be expected from climatology; a standard practice in the Eulerian framework. Unlike traditional approaches, which quantify contributions without reference to climatological behaviour, the anomaly-based approach gets to the heart of what we think truly matters—namely, identifying what is anomalous in situations where temperatures are highly anomalous. As a result, we are convinced that the new approach provides a better and more relevant quantification

of the relative importance of the underlying processes in the formation of heat extremes than has been achieved in previous studies (e.g. Röthlisberger and Papritz, 2023b).

However, despite its considerable value, the new approach also has its limitations. One of these limitations stems from the fact that the three processes in question are, to some extent, mutually dependent. For example, diabatic heating may only become particularly pronounced when cold air advection amplifies the temperature contrast between the land and the atmosphere. Thus, the contribution from diabatic heating is limited, to some extent, by the strength of both horizontal advection and subsidence. Similarly, the contributions from horizontal advection and subsidence partially limit each other. In regions with strong near-surface temperature gradients and weaker upper-level gradients, like coastal areas, the respective contributions may depend on where the air parcels sink—whether over the ocean or only after reaching land—either attributing more contribution to horizontal advection or subsidence; despite identical horizontal and vertical displacements. Such interdependencies make it virtually impossible to establish clear causal relationships, thereby constraining our Lagrangian analysis—as well as that of many others—to diagnostic rather than causal interpretations. However, diagnosis is the essential first step to understanding, and for this reason, we consider our work important.

6 Chapter 6
Outlook

Building on the diagnostic insights obtained in this study, an important next step could be to examine whether climate models accurately capture the underlying processes of heat extreme formation. To enhance confidence in climate model simulations—which project heat extremes to become more frequent and intense as global warming progresses—and to identify possible shortcomings of these models, Lagrangian studies like the one presented in this thesis applied to climate model simulations could serve to assess these models in greater depth. In this context, we see great potential in our tracer method, which could be easily implemented as an online tool in climate models, allowing the models to provide Lagrangian information simply in the form of a few additional output variables. By retrieving the required Lagrangian information through forward time integration, our method can operate as an online tool, eliminating the need to store data temporarily for offline calculation of the Lagrangian information using a separate tool. In this context, the tracer approach offers a significant advantage over trajectory models, which require data to be stored at sufficiently high spatial and temporal resolution for subsequent offline analysis. Since such high-resolution output of climate model simulations is typically not archived, Lagrangian studies based on climate model data remain extremely rare. To date, we are aware of only one study—Schielicke and Pfahl (2022)—that has computed trajectories from climate model simulations to examine heat extremes. Once it is clear that Lagrangian studies with climate models provide meaningful results, these studies could be used to answer the yet unresolved question of whether and to what extent the roles of the processes involved in heat extreme formation will change in the course of climate change. How will the contribution from horizontal advection be affected by a projected increase in the land–sea temperature contrast (e.g. IPCC, 2021)? Will subsidence become more influential as static stability increases (e.g. Schneider et al., 2010; Brogli et al., 2021)? And how might changes in the atmospheric circulation modulate these effects? Exciting questions that still await answers.

Bibliography

Añel, J., M. Fernández-González, X. Labandeira, X. López-Otero, and L. De La Torre (2017). "Impact of Cold Waves and Heat Waves on the Energy Production Sector". *Atmosphere* 8.11, p. 209. DOI: 10.3390/atmos8110209.

Aref, H. (1984). "Stirring by chaotic advection". *Journal of Fluid Mechanics* 143, pp. 1–21. DOI: 10.1017/S0022112084001233.

Barriopedro, D., R. García–Herrera, C. Ordóñez, D. G. Miralles, and S. Salcedo–Sanz (2023). "Heat waves: Physical understanding and scientific challenges". *Reviews of Geophysics* 61, e2022RG000780. DOI: 10.1029/2022RG000780.

Bieli, M., S. Pfahl, and H. Wernli (2015). "A Lagrangian investigation of hot and cold temperature extremes in Europe: Lagrangian Investigation of Hot and Cold Extremes". *Quarterly Journal of the Royal Meteorological Society* 141.686, pp. 98–108. DOI: 10.1002/qj.2339.

Birner, T. and H. Bönisch (2011). "Residual circulation trajectories and transit times into the extratropical lowermost stratosphere". *Atmospheric Chemistry and Physics* 11.2, pp. 817–827. DOI: 10.5194/acp-11-817-2011.

Black, E., M. Blackburn, G. Harrison, B. Hoskins, and J. Methven (2004). "Factors contributing to the summer 2003 European heatwave". *Weather* 59.8, pp. 217–223. DOI: 10.1256/wea.74.04.

Bönisch, H., A. Engel, J. Curtius, T. Birner, and P. Hoor (2009). "Quantifying transport into the lowermost stratosphere using simultaneous in-situ measurements of SF6 and CO2". *Atmospheric Chemistry and Physics* 9.16, pp. 5905–5919. DOI: 10.5194/acp-9-5905-2009.

Brewer, A. W. (1949). "Evidence for a world circulation provided by the measurements of helium and water vapour distribution in the stratosphere". *Quarterly Journal of the Royal Meteorological Society* 75.326, pp. 351–363. DOI: 10.1002/qj.49707532603.

Brogli, R., S. L. Sørland, N. Kröner, and C. Schär (2021). "Future summer warming pattern under climate change is affected by lapse-rate changes". *Weather and Climate Dynamics* 2.4, pp. 1093–1110. DOI: 10.5194/wcd-2-1093-2021.

Catalano, A. J., P. C. Loikith, and J. D. Neelin (2021). "Diagnosing Non-Gaussian Temperature Distribution Tails Using Back-Trajectory Analysis". *Journal of Geophysical Research: Atmospheres* 126.8. DOI: 10.1029/2020JD033726.

Chagnon, J. M., S. L. Gray, and J. Methven (2013). "Diabatic processes modifying potential vorticity in a North Atlantic cyclone: Diabatic Modification of Potential Vorticity". *Quarterly Journal of the Royal Meteorological Society* 139.674, pp. 1270–1282. DOI: 10.1002/qj.2037.

Conlon, K. C., N. B. Rajkovich, J. L. White-Newsome, L. Larsen, and M. S. O'Neill (2011). "Preventing cold-related morbidity and mortality in a changing climate". *Maturitas* 69.3, pp. 197–202. DOI: 10.1016/j.maturitas.2011.04.004.

Danielsen, E. F. (1961). "Trajectories: Isobaric, isentropic and actual". *Journal of Meteorology* 18, pp. 479–486. DOI: 10.1175/1520-0469(1961)018<0479:TIIAA>2.0.CO;2.

Davis, C. A., M. T. Stoelinga, and Y.-H. Kuo (1993). "The Integrated Effect of Condensation in Numerical Simulations of Extratropical Cyclogenesis". *Monthly Weather Review* 121, pp. 2309–2330. DOI: 10.1175/1520-0493(1993)121<2309:TIEOCI>2.0.CO;2.

Dobson, G. M. B. (1956). "Origin and distribution of the polyatomic molecules in the atmosphere". *Proceedings of the Royal Society of London. Series A. Mathematical and Physical Sciences* 236.1205, pp. 187–193. DOI: 10.1098/rspa.1956.0127.

Durran, D. R. (2010). *Numerical Methods for Fluid Dynamics*. Vol. 32. Texts in Applied Mathematics. New York: Springer. DOI: 10.1007/978-1-4419-6412-0.

Eckhardt, S., A. Stohl, H. Wernli, P. James, C. Forster, and N. Spichtinger (2004). "A 15-Year Climatology of Warm Conveyor Belts". *Journal of Climate* 17.1, pp. 218–237. DOI: 10.1175/1520-0442(2004)017<0218:AYCOWC>2.0.CO;2.

ECMWF (2016). "IFS Documentation CY41R2 - Part III: Dynamics and Numerical Procedures". *IFS Documentation CY41R2*. IFS Documentation 3. ECMWF. DOI: 10.21957/83wouv80.

Edmon, H. J., B. J. Hoskins, and M. E. McIntyre (1980). "EliassenPalm cross sections for the troposphere". *Journal of the Atmospheric Sciences* 37, pp. 2600–2616. DOI: 10.1175/1520-0469(1980)037<2600:EPCSFT>2.0.CO;2.

Eichner, J. F., E. Koscielny-Bunde, A. Bunde, S. Havlin, and H. J. Schellnhuber (2003). "Power-law persistence and trends in the atmosphere: A detailed study of long temperature records". *Physical Review E* 68.4, p. 046133. DOI: 10.1103/PhysRevE.68.046133.

Fischer, E. M., S. I. Seneviratne, D. Lüthi, and C. Schär (2007). "Contribution of land-atmosphere coupling to recent European summer heat waves". *Geophysical Research Letters* 34.6, 2006GL029068. DOI: 10.1029/2006GL029068.

Fischer, H., F. G. Wienhold, P. Hoor, O. Bujok, C. Schiller, P. Siegmund, M. Ambaum, H. A. Scheeren, and J. Lelieveld (2000). "Tracer correlations in the northern high latitude lowermost stratosphere: Influence of cross-tropopause mass exchange". *Geophysical Research Letters* 27.1, pp. 97–100. DOI: 10.1029/1999GL010879.

Fleming, Z. L., P. S. Monks, and A. J. Manning (2012). "Review: Untangling the influence of air-mass history in interpreting observed atmospheric composition". *Atmospheric Research* 104-105, pp. 1–39. DOI: 10.1016/j.atmosres.2011.09.009.

Forzieri, G., A. Cescatti, F. B. E Silva, and L. Feyen (2017). "Increasing risk over time of weather-related hazards to the European population: a data-driven prognostic study". *The Lancet Planetary Health* 1.5, e200–e208. DOI: 10.1016/S2542-5196(17)30082-7.

García-Herrera, R., J. Díaz, R. M. Trigo, J. Luterbacher, and E. M. Fischer (2010). "A Review of the European Summer Heat Wave of 2003". *Critical Reviews in Environmental Science and Technology* 40.4, pp. 267–306. DOI: 10.1080/10643380802238137.

Garfinkel, C. I. and N. Harnik (2017). "The Non-Gaussianity and Spatial Asymmetry of Temperature Extremes Relative to the Storm Track: The Role of Horizontal Advection". *Journal of Climate* 30.2, pp. 445–464. DOI: 10.1175/JCLI-D-15-0806.1.

Garfinkel, C. I., D. Rostkier-Edelstein, E. Morin, A. Hochman, C. Schwartz, and R. Nirel (2024). "Precursors of summer heat waves in the Eastern Mediterranean". *Quarterly Journal of the Royal Meteorological Society* 150, qj.4795. DOI: 10.1002/qj.4795.

Gasparrini, A., Y. Guo, M. Hashizume, E. Lavigne, A. Zanobetti, J. Schwartz, A. Tobias, S. Tong, J. Rocklöv, B. Forsberg, M. Leone, M. De Sario, M. L. Bell, Y.-L. L. Guo, C.-f. Wu, H. Kan, S.-M. Yi, M. De Sousa Zanotti Stagliorio Coelho, P. H. N. Saldiva, Y. Honda, H. Kim, and B. Armstrong (2015). "Mortality risk attributable to high and low ambient temperature: a multicountry observational study". *The Lancet* 386.9991, pp. 369–375. DOI: 10.1016/S0140-6736(14)62114-0.

Gheusi, F. and J. Stein (2002). "Lagrangian description of airflows using Eulerian passive tracers". *Quarterly Journal of the Royal Meteorological Society* 128.579, pp. 337–360. DOI: 10.1256/00359000260498914.

Gray, S. L. (2006). "Mechanisms of midlatitude cross-tropopause transport using a potential vorticity budget approach". *Journal of Geophysical Research* 111.D17, p. D17113. DOI: 10.1029/2005JD006259.

Harpaz, T., B. Ziv, H. Saaroni, and E. Beja (2014). "Extreme summer temperatures in the East Mediterranean-dynamical analysis". *International Journal of Climatology* 34.3, pp. 849–862. DOI: 10.1002/joc.3727.

Hartig, K., E. Tziperman, and C. P. Loughner (2023). "Processes Contributing to North American Cold Air Outbreaks Based on Air Parcel Trajectory Analysis". *Journal of Climate* 36.3, pp. 931–943. DOI: 10.1175/JCLI-D-22-0204.1.

Haynes, P. (1999). "Transport, stirring and mixing in the atmosphere". *Mixing: Chaos and Turbulence*. Ed. by H. Chaté, E. Villermaux, and J.-M. Chomaz. NATO ASI Series. New York: Kluwer Academic/Plenum Publishers, pp. 229–272. DOI: 10.1007/978-1-4615-4697-9.

Haynes, P. (2005). "Transport and Mixing in the Atmosphere". *Mechanics of the 21st Century*. Ed. by Witold Gutkowski and Tomasz A. Kowalewski. Berlin/Heidelberg: Springer-Verlag, pp. 139–152. DOI: 10.1007/1-4020-3559-4_8.

Hegglin, M. I., C. D. Boone, G. L. Manney, and K. A. Walker (2009). "A global view of the extratropical tropopause transition layer from Atmospheric Chemistry Experiment Fourier Transform Spectrometer O $_3$, H $_2$ O, and CO". *Journal of Geophysical Research* 114, D00B11. DOI: 10.1029/2008JD009984.

Hersbach, H., B. Bell, P. Berrisford, G. Biavati, A. Horányi, J. Muñoz Sabater, J. Nicolas, C. Peubey, R. Radu, I. Rozum, D. Schepers, A. Simmons, C. Soci, D. Dee, and J-N. Thépaut (2023a). "ERA5 hourly data on pressure levels from 1940 to present" [Dataset]. *Copernicus Climate Change Service (C3S) Data Store (CDS)*. (last access 04/2025). DOI: 10.24381/cds.bd0915c6.

Hersbach, H., B. Bell, P. Berrisford, G. Biavati, A. Horányi, J. Muñoz Sabater, J. Nicolas, C. Peubey, R. Radu, I. Rozum, D. Schepers, A. Simmons, C. Soci, D. Dee, and J-N. Thépaut (2023b). "ERA5 hourly data on single levels from 1940 to present" [Dataset]. *Copernicus Climate Change Service (C3S) Data Store (CDS)*. (last access 11/2024). DOI: 10.24381/cds.adbb2d47.

Hersbach, H., B. Bell, P. Berrisford, S. Hirahara, A. Horányi, J. Muñoz-Sabater, J. Nicolas, C. Peubey, R. Radu, D. Schepers, A. Simmons, C. Soci, S. Abdalla, X. Abellan, G. Balsamo, P. Bechtold, G. Biavati, J. Bidlot, M. Bonavita, G. De Chiara, P. Dahlgren, D. Dee, M. Diamantakis, R. Dragani, J. Flemming, R. Forbes, M. Fuentes, A. Geer, L. Haimberger, S. Healy, R. J. Hogan, E. Hólm, M. Janisková, S. Keeley, P. Laloyaux, P. Lopez, C. Lupu, G. Radnoti, P. de Rosnay, I. Rozum, F. Vamborg, S. Villaume, and J.-N. Thépaut (2017). "Complete ERA5 from 1940: Fifth generation of ECMWF atmospheric reanalyses of the global climate" [Dataset]. *Copernicus Climate Change Service (C3S) Data Store (CDS)*. (last access 11/2024). DOI: 10.24381/cds.143582cf.

Hersbach, H., B. Bell, P. Berrisford, S. Hirahara, A. Horányi, J. Muñoz-Sabater, J. Nicolas, C. Peubey, R. Radu, D. Schepers, A. Simmons, C. Soci, S. Abdalla, X. Abellan, G. Balsamo, P. Bechtold, G. Biavati, J. Bidlot, M. Bonavita, G. De Chiara, P. Dahlgren, D. Dee, M. Diamantakis, R. Dragani, J. Flemming, R. Forbes, M. Fuentes, A. Geer, L. Haimberger, S. Healy, R. J. Hogan, E. Hólm, M. Janisková, S. Keeley, P. Laloyaux, P. Lopez, C. Lupu, G. Radnoti, P. de Rosnay, I. Rozum, F. Vamborg, S. Villaume, and J.-N. Thépaut (2020). "The ERA5 global reanalysis". *Quarterly Journal of the Royal Meteorological Society* 146.730, pp. 1999–2049. DOI: 10.1002/qj.3803.

Hochman, A., S. Scher, J. Quinting, J. G. Pinto, and G. Messori (2021). "A new view of heat wave dynamics and predictability over the eastern Mediterranean". *Earth System Dynamics* 12.1, pp. 133–149. DOI: 10.5194/esd-12-133-2021.

Hoor, P., H. Fischer, L. Lange, J. Lelieveld, and D. Brunner (2002). "Seasonal variations of a mixing layer in the lowermost stratosphere as identified by the CO-O $_3$ correlation from in situ measurements". *Journal of Geophysical Research: Atmospheres* 107.D5, ACL 1–1–ACL 1–11. DOI: 10.1029/2000JD000289.

Hoor, P., H. Wernli, M. I. Hegglin, and H. Bönisch (2010). "Transport timescales and tracer properties in the extratropical UTLS". *Atmospheric Chemistry and Physics* 10.16, pp. 7929–7944. DOI: 10.5194/acp-10-7929-2010.

Horton, R. M., J. S. Mankin, C. Lesk, E. Coffel, and C. Raymond (2016). "A Review of Recent Advances in Research on Extreme Heat Events". *Current Climate Change Reports* 2.4, pp. 242–259. DOI: 10.1007/s40641-016-0042-x.

Hotz, B., L. Papritz, and M. Röthlisberger (2024). "Understanding the vertical temperature structure of recent record-shattering heatwaves". *Weather and Climate Dynamics* 5.1, pp. 323–343. DOI: 10.5194/wcd-5-323-2024.

IPCC (2021). "Climate Change 2021: The Physical Science Basis. Contribution of Working Group I to the Sixth Assessment Report of the Intergovernmental Panel on Climate Change". Ed. by V. Masson-Delmotte, P. Zhai, A. Pirani, S. L. Connors, C. Péan, S. Berger, N. Caud, Y. Chen, L. Goldfarb, M. I. Gomis, M. Huang, K. Leitzell, E. Lonnoy, J. B. R. Matthews, T. K. Maycock, T. Waterfield, O. Yelekçi, R. Yu, and B. Zhou. Cambridge, UK and New York, NY, USA: Cambridge University Press. DOI: 10.1017/9781009157896.

Iwasaki, T. (1989). "A Diagnostic Formulation for Wave-Mean Flow Interactions and Lagrangian-Mean Circulation with a Hybrid Vertical Coordinate of Pressure and Isentropes". *Journal of the Meteorological Society of Japan. Ser. II* 67.2, pp. 293–312. DOI: 10.2151/jmsj1965.67.2_293.

James, P. (2003). "A 15-year climatology of stratosphere-troposphere exchange with a Lagrangian particle dispersion model: 1. Methodology and validation". *Journal of Geophysical Research* 108.D12, p. 8519. DOI: 10.1029/2002JD002637.

Juckes, M. (2001). "A generalization of the transformed Eulerian-mean meridional circulation". *Quarterly Journal of the Royal Meteorological Society* 127.571, pp. 147–160. DOI: 10.1002/qj.49712757109.

Knippertz, P. and H. Wernli (2010). "A Lagrangian Climatology of Tropical Moisture Exports to the Northern Hemispheric Extratropics". *Journal of Climate* 23.4, pp. 987–1003. DOI: 10.1175/2009JCLI3333.1.

Koscielny-Bunde, E., A. Bunde, S. Havlin, H. E. Roman, Y. Goldreich, and H. Schellnhuber (1998). "Indication of a Universal Persistence Law Governing Atmospheric Variability". *Physical Review Letters* 81.3, pp. 729–732. DOI: 10.1103/PhysRevLett.81.729.

Kremer, T., E. Schömer, C. Euler, and M. Riemer (2020). "Cluster Analysis Tailored to Structure Change of Tropical Cyclones Using a Very Large Number of Trajectories". *Monthly Weather Review* 148, pp. 4209–4229. DOI: 10.1175/MWR-D-19-0408.1.

Lesk, C., P. Rowhani, and N. Ramankutty (2016). "Influence of extreme weather disasters on global crop production". *Nature* 529.7584, pp. 84–87. DOI: 10.1038/nature16467.

Li, X., M. E. Mann, M. F. Wehner, S. Rahmstorf, S. Petri, S. Christiansen, and J. Carrillo (2024). "Role of atmospheric resonance and land–atmosphere feedbacks as a precursor to the June 2021 Pacific Northwest Heat Dome event". *Proceedings of the National Academy of Sciences* 121.4, e2315330121. DOI: 10.1073/pnas.2315330121.

Madonna, E., H. Wernli, H. Joos, and O. Martius (2014). "Warm Conveyor Belts in the ERA-Interim Dataset (1979–2010). Part I: Climatology and Potential Vorticity Evolution". *Journal of Climate* 27.1, pp. 3–26. DOI: 10.1175/JCLI-D-12-00720.1.

Mayer, A. (2025a). "A new global Lagrangian analysis of near-surface temperature extremes: Code for figures (v1.1)" [Software]. *Zenodo*. DOI: 10.5281/zenodo.15853875.

Mayer, A. (2025b). "A new global Lagrangian analysis of near-surface temperature extremes: Dataset (v1.1)" [Dataset]. *Zenodo*. DOI: 10.5281/zenodo.15827328.

Mayer, A. (2025c). "The Tracer Method by Mayer and Wirth (v2.1)" [Software]. *Zenodo*. DOI: 10.5281/zenodo.14697529.

Mayer, A. (2025d). "The Tracer Method by Mayer and Wirth (v2.3)" [Software]. *Zenodo*. DOI: 10.5281/zenodo.14773247.

Mayer, A. (2025e). "Two different perspectives on heatwaves within the Lagrangian framework: Code for figures (v2.1)" [Software]. *Zenodo*. DOI: 10.5281/zenodo.14717758.

Mayer, A. (2025f). "Two different perspectives on heatwaves within the Lagrangian framework: Dataset (v1.0)" [Dataset]. *Zenodo*. DOI: 10.5281/zenodo.14679142.

Mayer, A. (2025g). "A new global Lagrangian analysis of near-surface temperature extremes". *Geophysical Research Letters* 52, e2025GL116696. DOI: 10.1029/2025GL116696.

Mayer, A. and V. Wirth (2023). "Lagrangian description of the atmospheric flow from Eulerian tracer advection with relaxation". *Quarterly Journal of the Royal Meteorological Society* 149.753, pp. 1271–1292. DOI: 10.1002/qj.4453.

Mayer, A. and V. Wirth (2025). "Two different perspectives on heatwaves within the Lagrangian framework". *Weather and Climate Dynamics* 6.1, pp. 131–150. DOI: 10.5194/wcd-6-131-2025.

Miltenberger, A. K., S. Pfahl, and H. Wernli (2013). "An online trajectory module (version 1.0) for the nonhydrostatic numerical weather prediction model COSMO". *Geoscientific Model Development* 6.6, pp. 1989–2004. DOI: 10.5194/gmd-6-1989-2013.

Miralles, D. G., P. Gentine, S. I. Seneviratne, and A. J. Teuling (2019). "Land-atmospheric feedbacks during droughts and heatwaves: state of the science and current challenges:

Land feedbacks during droughts and heatwaves". *Annals of the New York Academy of Sciences* 1436.1, pp. 19–35. DOI: 10.1111/nyas.13912.

Miralles, D. G., A. J. Teuling, C. C. van Heerwaarden, and J. Vilà-Guerau de Arellano (2014). "Mega-heatwave temperatures due to combined soil desiccation and atmospheric heat accumulation". *Nature Geoscience* 7.5, pp. 345–349. DOI: 10.1038/ngeo2141.

Neal, E., C. S. Y. Huang, and N. Nakamura (2022). "The 2021 Pacific Northwest Heat Wave and Associated Blocking: Meteorology and the Role of an Upstream Cyclone as a Diabatic Source of Wave Activity". *Geophysical Research Letters* 49.8, e2021GL097699. DOI: 10.1029/2021GL097699.

Oertel, A., M. Boettcher, H. Joos, M. Sprenger, H. Konow, M. Hagen, and H. Wernli (2019). "Convective activity in an extratropical cyclone and its warm conveyor belt – a case-study combining observations and a convection-permitting model simulation". *Quarterly Journal of the Royal Meteorological Society* 145.721, pp. 1406–1426. DOI: 10.1002/qj.3500.

Oertel, A., M. Pickl, J. F. Quinting, S. Hauser, J. Wandel, L. Magnusson, M. Balmaseda, F. Vitart, and C. M. Grams (2023). "Everything Hits at Once: How Remote Rainfall Matters for the Prediction of the 2021 North American Heat Wave". *Geophysical Research Letters* 50.3, e2022GL100958. DOI: 10.1029/2022GL100958.

Orszag, S. A. (1972). "Comparison of Pseudospectral and Spectral Approximation". *Studies in Applied Mathematics* 51.3, pp. 3077–3093. DOI: 10.1002/sapm1972513253.

Papritz, L. (2020). "Arctic Lower-Tropospheric Warm and Cold Extremes: Horizontal and Vertical Transport, Diabatic Processes, and Linkage to Synoptic Circulation Features". *Journal of Climate* 33.3, pp. 993–1016. DOI: 10.1175/JCLI-D-19-0638.1.

Papritz, L. and M. Röthlisberger (2023). "A Novel Temperature Anomaly Source Diagnostic: Method and Application to the 2021 Heatwave in the Pacific Northwest". *Geophysical Research Letters* 50.23, e2023GL105641. DOI: 10.1029/2023GL105641.

Pauluis, O., A. Czaja, and R. Korty (2010). "The Global Atmospheric Circulation in Moist Isentropic Coordinates". *Journal of Climate* 23.11, pp. 3077–3093. DOI: 10.1175/2009JCLI2789.1.

Pelletier, J. D. (1997). "Analysis and Modeling of the Natural Variability of Climate". *Journal of Climate* 10.6, pp. 1331–1342. DOI: 10.1175/1520-0442(1997)010<1331:AAMOTN>2.0.CO;2.

Pelletier, J. D. and D. L. Turcotte (1997). "Long-range persistence in climatological and hydrological time series: analysis, modeling and application to drought hazard assessment". *Journal of Hydrology* 203.1-4, pp. 198–208. DOI: 10.1016/S0022-1694(97)00102-9.

Perkins, S. E. (2015). "A review on the scientific understanding of heatwaves—Their measurement, driving mechanisms, and changes at the global scale". *Atmospheric Research* 164-165, pp. 242–267. DOI: 10.1016/j.atmosres.2015.05.014.

Pfahl, S. and H. Wernli (2012). "Quantifying the relevance of atmospheric blocking for co-located temperature extremes in the Northern Hemisphere on (sub-)daily time scales". *Geophysical Research Letters* 39.12, p. L12807. DOI: 10.1029/2012GL052261.

Philip, S. Y., S. F. Kew, G. J. Van Oldenborgh, F. S. Anslow, S. I. Seneviratne, R. Vautard, D. Coumou, K. L. Ebi, J. Arrighi, R. Singh, M. Van Aalst, C. Pereira Marghidan, M. Wehner, W. Yang, S.n Li, D. L. Schumacher, M. Hauser, R. Bonnet, L. N. Luu, F. Lehner, N. Gillett, J. S. Tradowsky, G. A. Vecchi, C. Rodell, R. B. Stull, R. Howard, and F. E. L. Otto (2022). "Rapid attribution analysis of the extraordinary heat wave on the Pacific coast of the US and Canada in June 2021". *Earth System Dynamics* 13.4, pp. 1689–1713. DOI: 10.5194/esd-13-1689-2022.

Pierrehumbert, R. T. and H. Yang (1992). "Global Chaotic Mixing on Isentropic Surfaces". *Journal of the Atmospheric Sciences* 50.15, pp. 2462–2480. DOI: 10.1175/1520-0469(1993)050<2462:GCMOIS>2.0.CO;2.

Ploeger, F. and T. Birner (2016). "Seasonal and inter-annual variability of lower stratospheric age of air spectra". *Atmospheric Chemistry and Physics* 16.15, pp. 10195–10213. DOI: 10.5194/acp-16-10195-2016.

Ploeger, F., P. Konopka, K. Walker, and M. Riese (2017). "Quantifying pollution transport from the Asian monsoon anticyclone into the lower stratosphere". *Atmospheric Chemistry and Physics* 17.11, pp. 7055–7066. DOI: 10.5194/acp-17-7055-2017.

Quinting, J. F. and M. J. Reeder (2017). "Southeastern Australian Heat Waves from a Trajectory Viewpoint". *Monthly Weather Review* 145.10, pp. 4109–4125. DOI: 10.1175/MWR-D-17-0165.1.

Reed, R. J. (1955). "A study of a characteristic type of upper-level frontogenesis". *Journal of Meteorology* 12, pp. 226–237. DOI: 10.1175/1520-0469(1955)012<0226:ASOACT>2.0.CO;2.

Röthlisberger, M. and L. Papritz (2023a). "A Global Quantification of the Physical Processes Leading to Near-Surface Cold Extremes". *Geophysical Research Letters* 50.5, e2022GL101670. DOI: 10.1029/2022GL101670.

Röthlisberger, M. and L. Papritz (2023b). "Quantifying the physical processes leading to atmospheric hot extremes at a global scale". *Nature Geoscience* 16, pp. 210–216. DOI: 10.1038/s41561-023-01126-1.

Ryoo, J.-M., D. E. Waliser, D. W. Waugh, S. Wong, E. J. Fetzer, and I. Fung (2015). "Classification of atmospheric river events on the U.S. West Coast using a trajectory model: Classification of ARs in the western US". *Journal of Geophysical Research: Atmospheres* 120.8, pp. 3007–3028. DOI: 10.1002/2014JD022023.

Schäfler, A., G. Craig, H. Wernli, P. Arbogast, J. D. Doyle, R. McTaggart-Cowan, J. Methven, G. Rivière, F. Ament, M. Boettcher, M. Bramberger, Q. Cazenave, R. Cotton, S. Crewell, J. Delanoë, A. Dörnbrack, A. Ehrlich, F. Ewald, A.s Fix, C. M. Grams, S. L. Gray, H. Grob, S. Groß, M. Hagen, B. Harvey, L. Hirsch, M. Jacob, T. Kölling, H. Konow, C. Lemmerz, O. Lux, L. Magnusson, B. Mayer, M. Mech, R. Moore, J. Pelon, J. Quinting, S. Rahm, M. Rapp, M. Rautenhaus, O. Reitebuch, C. A. Reynolds, H. Sodemann, T. Spengler, G. Vaughan, M. Wendisch, M. Wirth, B. Witschas, K. Wolf, and T. Zinner (2018). "The North Atlantic Waveguide and Downstream Impact Experiment". *Bulletin of the American Meteorological Society* 99.8, pp. 1607–1637. DOI: 10.1175/BAMS-D-17-0003.1.

Schär, C. and H. Wernli (1993). "Structure and evolution of an isolated semi-geostrophic cyclone". *Quarterly Journal of the Royal Meteorological Society* 119.509, pp. 57–90. DOI: 10.1002/qj.49711950904.

Schielicke, L. and S. Pfahl (2022). "European heatwaves in present and future climate simulations: a Lagrangian analysis". *Weather and Climate Dynamics* 3.4, pp. 1439–1459. DOI: 10.5194/wcd-3-1439-2022.

Schneider, T., T. Bischoff, and H. Płotka (2015). "Physics of Changes in Synoptic Midlatitude Temperature Variability". *Journal of Climate* 28.6, pp. 2312–2331. DOI: 10.1175/JCLI-D-14-00632.1.

Schneider, T., P. A. O'Gorman, and X. J. Levine (2010). "WATER VAPOR AND THE DYNAMICS OF CLIMATE CHANGES". *Reviews of Geophysics* 48.3. DOI: 10.1029/2009rg000302.

Schumacher, D. L., M. Hauser, and S. I. Seneviratne (2022). "Drivers and Mechanisms of the 2021 Pacific Northwest Heatwave". *Earth's Future* 10.12, e2022EF002967. DOI: 10.1029/2022EF002967.

Schumacher, D. L., J. Keune, C. C. Van Heerwaarden, J. Vilà-Guerau De Arellano, A. J. Teuling, and D. G. Miralles (2019). "Amplification of mega-heatwaves through heat torrents fuelled by upwind drought". *Nature Geoscience* 12.9, pp. 712–717. DOI: 10.1038/s41561-019-0431-6.

Screen, J. (2014). "Arctic amplification decreases temperature variance in northern mid- to high-latitudes". *Nature Climate Change* 4, pp. 577–582. DOI: 10.1038/nclimate2268.

Simmons, A. J. and D. M. Burridge (1981). "An Energy and Angular-Momentum Conserving Vertical Finite-Difference Scheme and Hybrid Vertical Coordinates". *Monthly Weather Review* 109, pp. 758–766. DOI: 10.1175/1520-0493(1981)109<0758:AEAAMC>2.0.CO;2.

Škerlak, B., M. Sprenger, and H. Wernli (2014). "A global climatology of stratosphere–troposphere exchange using the ERA-Interim data set from 1979 to 2011". *Atmospheric Chemistry and Physics* 14.2, pp. 913–937. DOI: 10.5194/acp-14-913-2014.

Sousa, P. M., D. Barriopedro, A. M. Ramos, R. García-Herrera, F. Espírito-Santo, and R. M. Trigo (2019). "Saharan air intrusions as a relevant mechanism for Iberian heatwaves: The record breaking events of August 2018 and June 2019". *Weather and Climate Extremes* 26, p. 100224. DOI: 10.1016/j.wace.2019.100224.

Sousa, P. M., R. M. Trigo, D. Barriopedro, P. M. M. Soares, and J. A. Santos (2018). "European temperature responses to blocking and ridge regional patterns". *Climate Dynamics* 50.1-2, pp. 457–477. DOI: 10.1007/s00382-017-3620-2.

Spensberger, C., E. Madonna, M. Boettcher, C. M. Grams, L. Papritz, J. F. Quinting, M. Röthlisberger, M. Sprenger, and P. Zschenderlein (2020). "Dynamics of concurrent and sequential Central European and Scandinavian heatwaves". *Quarterly Journal of the Royal Meteorological Society* 146.732, pp. 2998–3013. DOI: 10.1002/qj.3822.

Sprenger, M. and H. Wernli (2015). "The LAGRANTO Lagrangian analysis tool – version 2.0". *Geoscientific Model Development* 8.8, pp. 2569–2586. DOI: 10.5194/gmd-8-2569-2015.

Stefanon, M., F. D'Andrea, and P. Drobinski (2012). "Heatwave classification over Europe and the Mediterranean region". *Environmental Research Letters* 7.1, p. 014023. DOI: 10.1088/1748-9326/7/1/014023.

Stein, A. F., R. R. Draxler, G. D. Rolph, B. J. B. Stunder, M. D. Cohen, and F. Ngan (2015). "NOAA's HYSPLIT Atmospheric Transport and Dispersion Modeling System". *Bulletin of the American Meteorological Society* 96.12, pp. 2059–2077.

Stoelinga, M. T. (1996). "A Potential Vorticity-Based Study of the Role of Diabatic Heating and Friction in a Numerically Simulated Baroclinic Cyclone.pdf". *Monthly Weather Review* 124.5, pp. 849–874. DOI: 10.1175/1520-0493(1996)124<0849:APVBSO>2.0.CO;2.

Stohl, A. (1998). "Computation, accuracy and applications of trajectories—A review and bibliography". *Atmospheric Environment* 32.6, pp. 947–966. DOI: 10.1016/S1352-2310(97)00457-3.

Stohl, A., S. Eckhardt, C. Forster, P. James, N. Spichtinger, and P. Seibert (2002). "A replacement for simple back trajectory calculations in the interpretation of atmospheric trace substance measurements". *Atmospheric Environment* 36.29, pp. 4635–4648. DOI: 10.1016/S1352-2310(02)00416-8.

Stohl, A., C. Forster, and H. Sodemann (2008). "Remote sources of water vapor forming precipitation on the Norwegian west coast at 60°N-a tale of hurricanes and an atmospheric river". *Journal of Geophysical Research: Atmospheres* 113.D5, p. D05102. DOI: 10.1029/2007JD009006.

Stohl, A., L. Haimberger, M. P. Scheele, and H. Wernli (2001). "An intercomparison of results from three trajectory models". *Meteorological Applications* 8.2, pp. 127–135. DOI: 10.1017/S1350482701002018.

Talkner, P. and R. O. Weber (2000). "Power spectrum and detrended fluctuation analysis: Application to daily temperatures". *Physical Review E* 62.1, pp. 150–160. DOI: 10.1103/PhysRevE.62.150.

Tamarin-Brodsky, T., K. Hodges, B. J. Hoskins, and T. G. Shepherd (2019). "A Dynamical Perspective on Atmospheric Temperature Variability and Its Response to Climate Change". *Journal of Climate* 32.6, pp. 1707–1724. DOI: 10.1175/JCLI-D-18-0462.1.

Thornton, H. E., B. J. Hoskins, and A. A. Scaife (2016). "The role of temperature in the variability and extremes of electricity and gas demand in Great Britain". *Environmental Research Letters* 11.11, p. 114015. DOI: 10.1088/1748-9326/11/11/114015.

Townsend, R. D. and D. R. Johnson (1985). "A diagnostic study of the isentropic zonally averaged mass circulation during the first GARP global experiment". *Journal of the Atmospheric Sciences* 42.15, pp. 1565–1579. DOI: 10.1175/1520-0469(1985)042<1565:ADSOTI>2.0.CO;2.

Tuel, A. and O. Martius (2024). "Persistent warm and cold spells in the Northern Hemisphere extratropics: regionalisation, synoptic-scale dynamics and temperature budget". *Weather and Climate Dynamics* 5.1, pp. 263–292. DOI: 10.5194/wcd-5-263-2024.

Turner, J. K., J. Gyakum, and S. M. Milrad (2013). "A Thermodynamic Analysis of an Intense North American Arctic Air Mass". *Monthly Weather Review* 141.1, pp. 166–181. DOI: 10.1175/MWR-D-12-00176.1.

Villiers, M. P. (2020). "Europe extreme heat 22–26 July 2019: was it caused by subsidence or advection?" *Weather* 75.8, pp. 228–235. DOI: 10.1002/wea.3717.

Welander, P. (1955). "Studies on the General Development of Motion in a Two-Dimensional, Ideal Fluid". *Tellus* 7.2, pp. 141–156. DOI: 10.3402/tellusa.v7i2.8797.

Wernli, H. (1997). "A Lagrangian-based analysis of extratropical cyclones. II: A detailed case-study". *Quarterly Journal of the Royal Meteorological Society* 123.542, pp. 1677–1706. DOI: 10.1002/qj.49712354211.

Wernli, H. and M. Bourqui (2002). "A Lagrangian "1-year climatology" of (deep) cross-tropopause exchange in the extratropical Northern Hemisphere". *Journal of Geophysical Research* 107.D2, p. 4021. DOI: 10.1029/2001JD000812.

Wernli, H. and H. C. Davies (1997). "A Lagrangian-based analysis of extratropical cyclones. I: The method and some applications". *Quarterly Journal of the Royal Meteorological Society* 123.538, pp. 467–489. DOI: 10.1002/qj.49712353811.

White, R. H., S. Anderson, J. F. Booth, G. Braich, C.a Draeger, C. Fei, C. D. G. Harley, S. B. Henderson, M. Jakob, C.-A. Lau, L. Mareshet Admasu, V. Narinesingh, C. Rodell, E. Roocroft, K. R. Weinberger, and G. West (2023). "The unprecedented Pacific Northwest heatwave of June 2021". *Nature Communications* 14.1, p. 727. DOI: 10.1038/s41467-023-36289-3.

Williamson, J. H (1980). "Low-storage Runge-Kutta schemes". *Journal of Computational Physics* 35.1, pp. 48–56. DOI: 10.1016/0021-9991(80)90033-9.

Zschenderlein, P., A. H. Fink, S. Pfahl, and H. Wernli (2019). "Processes determining heat waves across different European climates". *Quarterly Journal of the Royal Meteorological Society* 145.724, pp. 2973–2989. DOI: 10.1002/qj.3599.

Zschenderlein, P., G. Fragkoulidis, A. H. Fink, and V. Wirth (2018). "Large-scale Rossby wave and synoptic-scale dynamic analyses of the unusually late 2016 heatwave over Europe: Large-scale Rossby wave and synoptic-scale dynamic analyses of the unusually late 2016 heatwave over Europe". *Weather* 73.9, pp. 275–283. DOI: 10.1002/wea.3278.

Zschenderlein, P., S. Pfahl, H. Wernli, and A. H. Fink (2020). "A Lagrangian analysis of upper-tropospheric anticyclones associated with heat waves in Europe". *Weather and Climate Dynamics* 1.1, pp. 191–206. DOI: 10.5194/wcd-1-191-2020.